Self-sensing Graphene Nanoelectromechanical Systems

Thesis by

Madhav Kumar

In partial fulfilment of the requirement for the degree of

Doctor of Philosophy in Materials

DEPARTMENT OF MATERIALS

UNIVERSITY OF OXFORD

2015

To my

Parents

ABSTRACT

Self-sensing Graphene Nanoelectromechanical Systems

Madhav Kumar

Nanoelectromechanical systems (NEMS) can measure very small forces and mass as has been showcased in the last decade by the demonstration of measurements ranging from single spin detection and mass spectroscopy to the read-out of the quantum ground state of a mesoscopic resonator. Mass spectroscopy with NEMS is particularly appealing because the vibrational frequency of NEMS is a sensitive function of its total mass; thus minute changes in mass due to added or removed adsorbate will change the resonance frequency of a nanomechanical resonator. Indeed, single molecule detection has recently been demonstrated using NEMS as a sensitive mass detector. To maximize mass as well as force sensitivity, resonators with low mass and high quality factors are required. Extreme stiffness, low mass, a high Young's modulus and good conductivity makes one atom-thick graphene a most suitable candidate for NEMS. However, achieving quality factors higher than 10^3 at room temperature has been a bottleneck for graphene NEMS. Extensive studies have been carried out on graphene NEMS by employing both optical, and electrostatic transduction techniques. Optical transduction requires large and complicated experimental setups. This restricts the use of this technique to low temperatures and high magnetic fields. Electrostatic sensing, another commonly used technique requires more complex circuitry and can damp the motion due to electrostatic force. In this thesis the use of

piezoresistive transduction to transduce motion of graphene resonator is explored. Major advantages of piezoresistive sensing over other sensing methods are its fairly linear response, robustness, simple measuring circuitry and implementation. It has been demonstrated in the present work that piezoresistive sensing is not only a simple but also an extremely effective electrical readout method for graphene based nanoelectromechanical systems.

The first part of the thesis starts with an introduction to Nanoelectromechanical systems (NEMS), explaining how it originates from simple electromechanical systems and then later evolved from Microelectromechanical systems (MEMS). Finite element method (FEM) analysis confirms that the stresses are concentrated at the legs of H-shaped mechanical resonator which we have used to maximize the piezoresistive effect of graphene. Modal analysis is performed employing *Comsol Multiphysics* to carry out the simulations in order to predetermine the frequency range, which is as the same order of the experimentally measured resonance frequencies of the devices. Thermoelastic damping (TED) simulations are carried out to show comparison between different structures of the resonators. Detailed fabrication processes using standard e-beam lithography to fabricate fully suspended H shape graphene resonator have been developed. Graphene resonators are electronically characterized using piezoresistive sensing. Detailed measurements such as piezomechanical and thermomechanical, frequency and time domain measurements are carried out. One order higher Q-factors (10^3) than the previous reported values for double side clamped beams in ambient temperatures has been

measured. The minimum detectable mass and force resolution of such resonators are estimated using the experimental results to be an astounding 0.95 – 1.54 zeptograms (10^{-21} g) and 11.7 – 21.6 aN/$Hz^{1/2}$ at *room temperature* respectively. Various nonlinearities in graphene resonators such as nonlinearity in spring constant as well as higher order nonlinear damping are carefully considered. Simulations as well as experimental results showing various nonlinear effects such as saddle node bifurcation, super-harmonics, Pol-Duffing and unstable states are discussed. In the last part of the thesis, some additional data of the higher order resonance modes with symmetric and asymmetric shape of the devices have been demonstrated. Interesting behaviors such as peak splitting, resonance and anti-resonance peak, have been experimentally observed. This is further confirmed with the experimental results from the commercial cantilever using AFM.

Table of Contents

List of Figures

List of Tables

List of Symbols used

NH_4F: Ammonium Fluoride

ω: Angular frequency

AFM: Atomic Force Microscopy

aN: Atto Newton

Ar: Argon

BOE: Buffered Oxide Etchant

CO_2: Carbon Dioxide

CVD: Chemical Vapour Deposition

Cr: Chromium

CAD: Computer Aided Design

Cu: Copper

CPD: Critical Point Drying

A: Cross sectional area

V_{Inp}: DC bias to the resonator

DI: Deionised

V_{Ext}: Drive amplitude

DR: Dynamic Range

R: Electrical resistance

ρ: Electrical resistivity

FFT: Fast Fourier Transform

FEM: Finite Element Method

f: Frequency

GF: Gauge Factor

Au: Gold

g: Gram

GO: Graphene Oxide

Hz: Hertz

HOPG: Highly Oriented Pyrolytic Graphite

HF: Hydrogen Fluoride

IPA: Isopropyl Alcohol

L: Length

ρ: Mass density

MIBK: Methyl Iso Butyl Ketone

MEMS: Micro Electro Mechanical Systems

mm: Micrometer

NEMS: Nano Electro Mechanical Systems

NG: Nano Graphene

nm: Nanometer

Ω: Ohm

π: Piezoresistive coefficient

v: Poisson's ratio

PDMS: Poly Di Methyl Siloxane

PMMA: Poly Methyl Metha Acrylate

Q: Quality factor

RIE: Reactive Ion Etching

f_0: Resonance frequency

SEM: Scanning Electron Microscope

Si: Silicon

SiO_2: Silicon Dioxide

SiN: Silicon Nitride

Sccm: Standard Cubic Centimeters per Minute

S: Strain

τ: Stress

TED: Thermo Elastic Damping

W: Watt

E: Young's modulus

*All other symbols are explained appropriately in the thesis wherever it appears.

Acknowledgements

First of all, I would like to thank my advisor Professor Harish Bhaskaran from the bottom of my heart for his guidance, encouragement, and understanding all through; not only for scientific and technical matters, but also for any matter unrelated to the lab, Prof. Bhaskaran has been a patient and helpful guide. In spite of his busy schedule, when I need him, he has always been there for help. When I observed the sign of graphene mechanical resonance for the first time, I was very excited and emailed Harish at midnight. He emailed me back within ten minutes and showed up in the lab next day in the morning to provide appreciation and motivation. As a graduate student I have learnt a lot from him and this PhD could have never been possible without his encouragement after each and every failure and appreciation after every tiny success in research. I admire his sharp instincts of research and punctuality, and endeavor to follow and uphold these standards in my career. He has inspired me to pursue research further as a carrier after my PhD. Apart from a great role model in research, Harish also inspires me as a great human being. One of my greatest motivations has always been to match the high standards you have set for your graduate students. Three years from now when I look back, if my research work is able to meet your expectations, I will call it a success.

I was lucky to get help from a lot of people during my DPhil research. I have immensely benefitted from discussions with Professor Bhaskar Choubey. He has always explained complex physics, mathematical equations and electronics in a layman's way

which I can understand. Being one of the very first DPhil student of the lab, it was quite a unique experience for me in helping set-up the lab from the ground up. I would especially thank Benjamin Porter for showing me the true potential of Finite element analysis. Your sincerity and punctuality has inspired me a lot. I would like to thank Gerardo Rodriguez-Hernandez for his elaborate explanations and solutions to all the problems I had in understanding complex electronic circuitry. I look up to your patience and hard work. Ben and Gerardo have been a great support for me from the very first day of my DPhil. I would like to thank Dr. Peiman Hosseini for his very valuable insights and guidance during the work. As a senior researcher he has always extended his helping hand in all possible ways and his perseverance and intelligence has inspired me a lot. With his great sense of humour, he has always maintained an enjoyable and fun environment in the lab. He has shown that cutting edge research can be truly enjoyable as well. I would also want to thank Dr. Merce Paciois Pujado for her help over the years. It feels very good to have a senior researcher like you in the group. Apart from your hard work in research your fitness, especially cycling always inspires me. I would like to thank Carlos Rios, the new member of our group, (sorry even after one and half year, I consider you as a new member!). Your deep understanding of resonators has helped me a lot. I always admire your confidence and intelligence. It was a great experience working with visiting students Dominique, Freddie, Jasmine, and Alex.

I gratefully acknowledge funding support for my research by the Department of Materials, University of Oxford, EPSRC, and the John Fell Fund. I appreciate the timely help

of the entire staff of the Department of Materials, University of Oxford. I would like to thank Chris Downs, Tom Bointon, and David Anderson from the University of Exeter for their help with my research.

Life at Oxford is filled with formal dinners, pub crawls, punting and loads of social and academic events. It is an amazing experience living in Oxford and I thoroughly enjoyed my student life. I was very lucky to have really good friends to make my stay in Oxford quite enjoyable especially Aayush, Anjul, Ashish, Avani, Karabi, Kokil, Manisha, Meenakshi, Nishant, Pranoy, Prateek, Rakesh, Sanskriti, Shifali, Sounak and many more. I would like to thank all the people who have made these last three years a memorable experience.

And finally and most importantly I would like to thank my family for always taking care of me, loving me, supporting me throughout my life, irrespective of the situation, advising me whenever I needed it. Dad, your energy and love for life is an inspiration for me. You are not only my superhero but, my *guru* as well. From teaching me my first alphabet to Newton's first law of motion, from explaining condensed matter physics to Verses of *Srimad Bhagavad Gita,* you have been my teacher, *guru,* advisor, mentor and everything. You are the most knowledgeable, yet diverse and open-minded person I have ever come across. Probably that's the reason you are my best friend as well. I would like to thank Mom, for your unconditional and pure love and care for me. I love your spontaneity and respect all the sacrifices you have made for us. I cherish my brother for his unwavering faith in me. I have never worried about my life because I know you will be always there for me, irrespective of the situation. I thank my sister-in-law for being an amazing friend. I feel

lucky to have amazing cousins providing me a vital support system all through. I am very thankful to Prof. S. Biswas for inspiring me to peruse a carrier in research. I am grateful to my friends Swaraj, Pradeep and Alex who are always there for me whenever I need them. Last but not the least, I am grateful to my sweetheart *Swasti,* my sweetest little niece, for making me relive my childhood and bring a smile on my face whenever I see you.

Chapter 1

Introduction to Graphene Nanoelectromechanical systems

1.1 Introduction to electromechanical systems

As its literal meaning would suggest, an electromechanical system [1] consists of electrical and mechanical parts coupled to each other. In 1785, the first electromechanical system was demonstrated by Charles-Augustin de Coulomb who measured electric charges and formulated the very famous Coulomb's law in electrostatics using the Coulomb's torsion balance [2]. Figure 1. 1 shows the experimental setup of the Coulomb's torsion balance of 1785 [2]. Coulomb's torsion balance is an ideal example of electromechanical system which has both electrical and mechanical parts coupled to each other with a transducer. As we change the electrical charge on the metallic sphere the deflection in the moving mechanical part i.e., the torsional fiber also changes. The read out is the visual observation of the scale on the cylindrical glass case. The torsional angle of the fiber thread is measured with the amount of charge introduced on the metallic sphere. Figure 1.2a shows the schematic representation of a multilevel electromechanical system [3]. For a resonant device, the electrical input signal is applied to input transducers which convert the electrical energy into mechanical stimuli, which is applied to a mechanical system such as a resonator. For example in a piezo-shaker as we apply an AC signal, the piezo vibrates mech-

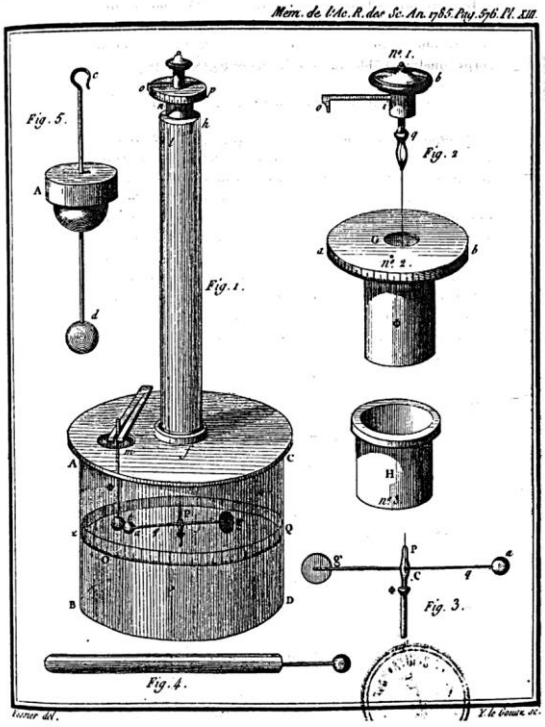

Figure 1. 1 Experimental setup of Coulomb's torsion balance of 1785. (Image reproduced from Ref. [2])

anically at the applied frequency and so do the structure (resonator) coupled to the piezo. The response (vibration) from the mechanical system is transduced back into an electrical output signal using an output transducer. Control systems perturb the mechanical response such as modifying the vibrational frequency and quality factor of the vibrating system. Figure 1.2b shows the schematic representation of a self-sensing electromechanical system [4] driven externally using an input transducer, the one used in the present work. Unlike the conventional electromechanical systems here we do not required any extra output transducer to convert the mechanical defection to electrical signal. The intrinsic property

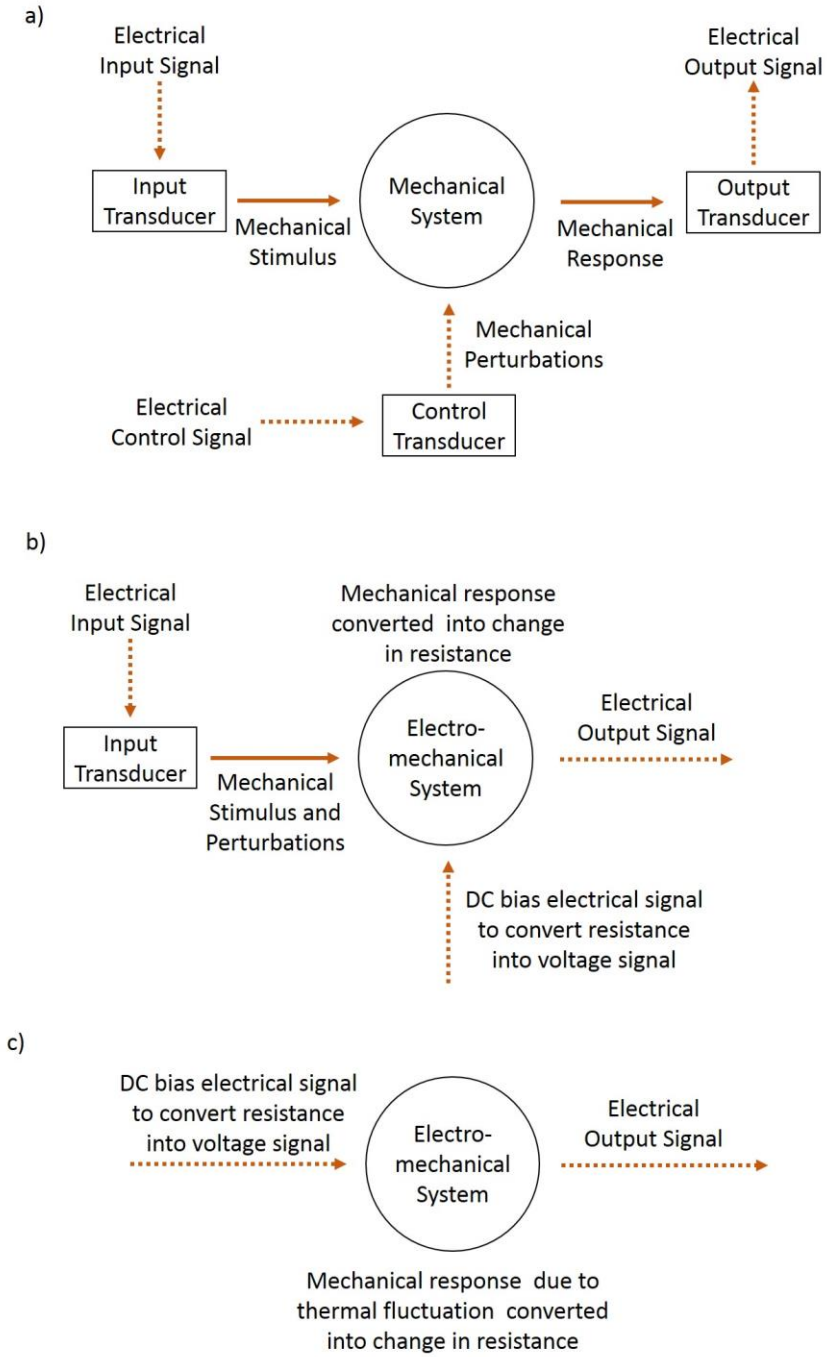

Figure 1.2 a) Schematic representation of a multilevel electromechanical systems. b) Schematic representation of a piezoresistive sensing driven externally and c) thermo-mechanically driven by Brownian motion (used in the present work)

of the system such as piezoresistivity is used as a self-sensing component to transduce mechanical energy into electrical energy. As the system vibrate resistance of the mechanical system changes. A DC bias voltage is applied to the electromechanical system which converts the change in resistance into an output voltage signal. Also the input transducer can be used to perturb the system and accordingly the resonance frequency and the quality factor can be changed. Figure 1.2c shows schematic representation of a self-sensing electromechanical system driven thermally [4] by the surrounding temperature. Here we do not require any input transducer (external driving force) but the thermal vibration due to the surrounding temperature is sufficient to vibrate the system.

1.2 Introduction to Microelectromechanical systems

Microelectromechanical or MEMS are electromechanical systems which have all the components with dimensions in the micron scale, often called as microsystems or micro-machines. MEMS are example of miniaturization of electromechanical devices from macroscopic to microscopic dimensions. A paradigm shift in manufacturing, sensing and application has been brought about by MEMS. For example, highly priced macroscopic piezoelectric accelerometers have been replaced by inexpensive minuscule silicon accelerometers. Apart from being smaller in size, the main advantage of MEMS is that batch fabrication is utilized in the manufacturing process. Unlike traditional manufacturing where devices are manufactured one at a time, using batch fabrication processes [5], thousands of identical devices can be processed simultaneously on a single wafer. MEMS based

devices such as inkjet print heads, micro mirrors, pressure sensors, accelerometer gyroscopes etc. are less expensive and superior to previous technologies.

The first few commercially successful MEMS devices were pressure sensors and accelerometers which were fabricated in the 1970s. Further, development of MEMS and integrated circuit (IC) technology go hand-in-hand. IC fabrication technologies such as lithography, etching and thin film deposition (or growth) were first used to fabricate MEMS in 1980s. In 1980s and 1990s significant research and development took place in the field of new fabrication technologies, different devices and markets for MEMS. Today MEMS based products have a huge impact on our society. Although the future of MEMS is quite bright, in order to accelerate the development, new manufacturing processes and applications will have to be continuously invented. Emerging applications based on MEMS that have a huge potential to grow in the future are resonators, switches, drug delivery systems, optical switches and micro-spectrometers.

The resonant transducer is one of the most common micro-electromechanical devices. Strain induced is converted into resonant frequency change of the device by the resonant transducer. Different detection techniques such as electrostatic, optical, piezoelectrical, and piezoresistive are used to detect the resonant frequency. Measurement of pressure, acceleration, vibration and so on has been done using these resonant transducers.

1.3 Introduction to Nanoelectromechanical systems (NEMS) [3]

On 29th December 1959, Richard Phillips Feynman [6] who received his Nobel Prize in Physics in 1965 gave his much quoted talk at the annual meeting of the American Physical Society, which is now often quoted as the "There's Plenty of Room at the Bottom" [1,7,8] . Long before the word *nano* came into the picture, his question to the scientific world *''Why cannot we write the entire 24 volumes of the Encyclopaedia Britannica on the head of a pin?''* during his talk was a defining moment in the field of nano science and technology. It became the road map for present and future nanotechnology. He looked into the future and predicted how technology could create structures that would be as small as the size of an atom. At the end of his talk he offered a prize of $1,000 to the first person who can take the information on the page of a book and put it on an area 1/25,000 smaller in linear scale in such a manner that it can be read by an electron microscope. He also offered another prize of $1,000 to someone who can make an operating electric motor which can be controlled from the outside and is only 1/64 inch cube in size.

Few months later the challenge offered by Feynman to stimulate the development of micro miniaturization was completed successfully by William McLellan [9] a mechanical engineer and alumnus of the California Institute of Technology. Out of several McLellan's motors one of the motor is still displayed in the corridor of the Caltech physics department. McLellan made a micro motor which was about the size of a pencil dot on a paper, even smaller than what Feynman specified. It weighed around 250 micro gram and required a power of 1 milliwatt to operate. McLellan used tweezers, a fine paintbrush and a toothpick

as tools to make his device. He used intelligent machining tricks such as drilling holes in his minuscule components by using watchmakers' tools etc. to scale down the components. The other prize was claimed in 1985, by Tom Newman, a Stanford graduate student by writing the first paragraph of '*A Tale of Two Cities*' in an area 1/25,000 times smaller [10].

In nanoelectromechanical systems [3] or NEMS the dimensions of the components of the systems are in deep sub-micron scale. It can be considered to be a further miniaturisation of MEMS. NEMS represents devices integrating electrical and mechanical components on the nanoscale, such as resonators. Flexural and torsional vibrations are the two mechanical motions mostly detected in these resonators. In case of flexural resonators, the moving mechanical part is either a cantilever (a mechanical beam clamped at one end), or a doubly clamped beam. An example of torsional oscillator would be a paddle. In this thesis I focus only on a special geometry of the doubly clamped beam.

The low mass and high quality factors that nanomechanical resonators exhibit leads to exceptional sensitivity in the frequency domain. [3-4, 11-34] Suspended CNT-based resonators [22] have shown operating frequency as high as 1.3 GHz which can go up to 10 GHz and even in terahertz range by scaling down the resonators. Researchers have measured room temperature quality factors (Q) as high as 4×10^5 [23] for silicon nitride nanomechanical resonators and up to 5×10^6 [24] at low temperatures for carbon nanotube resonators. The ultra-high quality factors and resonance frequencies make NEMS an ideal candidate for sensing applications such as a mass [14-18] and force [12, 13] sensors.

The sensitivity of a nanomechanical mass and force sensor depends on its mass and quality factor; a low mass and high quality factor reduces both the minimum resolvable force [12, 13] and mass [14]. The minimum detectable mass is given by:

$$\delta m = 2M_{eff}\left(\frac{\Delta f}{Q\omega_o}\right)^{1/2} 10^{-DR/20} \quad (1.1)$$

Where M_{eff} is the resonator mass, Q the quality factor and ω_o the resonance frequency, Δf the measurable bandwidth and DR the dynamic range [25, 26]. Hence a low mass resonator with high Q would be ideal for mass sensor. The minimum detectable force (F_{min}) of a nanomechanical resonator is given by the force spectral density (S_{th}^{F}):

$$F_{min} = \sqrt{S_{th}^{F}} = \sqrt{\frac{4kTk_b}{\omega_0 Q}} \quad (1.2)$$

Where k is the spring constant (which increases with increasing mass, as $k = M_{eff}\,\omega^2$), T the temperature and k_b is the Boltzmann constant. Thus, to maximize force sensitivity, resonators with low mass, low resonance frequency, and high quality factors are required.

Nanoelectromechanical systems (NEMS) can measure very small forces [12, 13] and masses [15, 16] as has been showcased in the last decade. NEMS has been used to demonstrate measurements ranging from detection of single spin [11], to displacement [27-33]. Mass spectroscopy [17, 18] with NEMS is particularly appealing because the vibrational frequency of NEMS is a sensitive function of its total mass; thus minute changes in mass due to added or removed adsorbate will change the resonance frequency of a nanomechanical resonator. Indeed, single molecule detection has recently been demonstrated using NEMS as a sensitive mass detector [17, 18].

1.4 Introduction to Graphene: The miracle material of 21st Century

Graphene [35] a single atom thick sheet of carbon atom arranged in the honeycomb lattice has fascinated the researchers and industry from every field of science and technology. Research in the field of graphene is truly one of the largest and most rapidly growing fields in material science and technology.

Theoretically graphene had been first studied by *P.R Wallace* in 1947 [36] when he calculated the band structure of graphene. This was the starting point of understanding the electronic properties of graphene. In 1962 *Von H. P. Boehm* [37] synthesised graphene successfully for the first time by reducing a graphite oxide monolayer. He managed to measure the thickness of a graphene layer using electron microscopy and X-ray scattering characterization tools. He named it ''*graphene*'' in 1986 [38] as a molecule by combining ''*graph*'' from the word graphite and the suffix ''*ene*'' considering it as a hydrocarbon. Thanks to researchers *Andre Geim* and Konstantin *Novolselov* at University of Manchester for their ''*Friday evening experiment*''. In 2004 they managed to successfully isolate the first free standing two dimensional material, single layer graphene, after years of attempts to isolate a single layer of graphite. For their simple but ground breaking research on graphene they both won the 2010 Nobel Prize in Physics.

Quasi two dimensional graphene is the building block for all other carbon allotropes. As shown in Figure 1.3 it can be wrapped into zero dimension bucky balls, rolled into one dimensional nanotube, or stacked into three dimensional graphite. Unlike in diamond where carbon atoms are covalently bonded by sp^3 hybridization, in graphene, carbon atoms

are covalently bonded by sp^2 hybridization. This results in high in-plane Young's modulus (1 terapascal (TPa)), 2-D elastic stiffness of 340 Newton/meter (Nm^{-1}) and breaking strength of 42 Nm^{-1} [39]. This makes graphene the strongest material on planet, even 200 times stronger than steel but still being one atom thick it is the thinnest material on the planet.

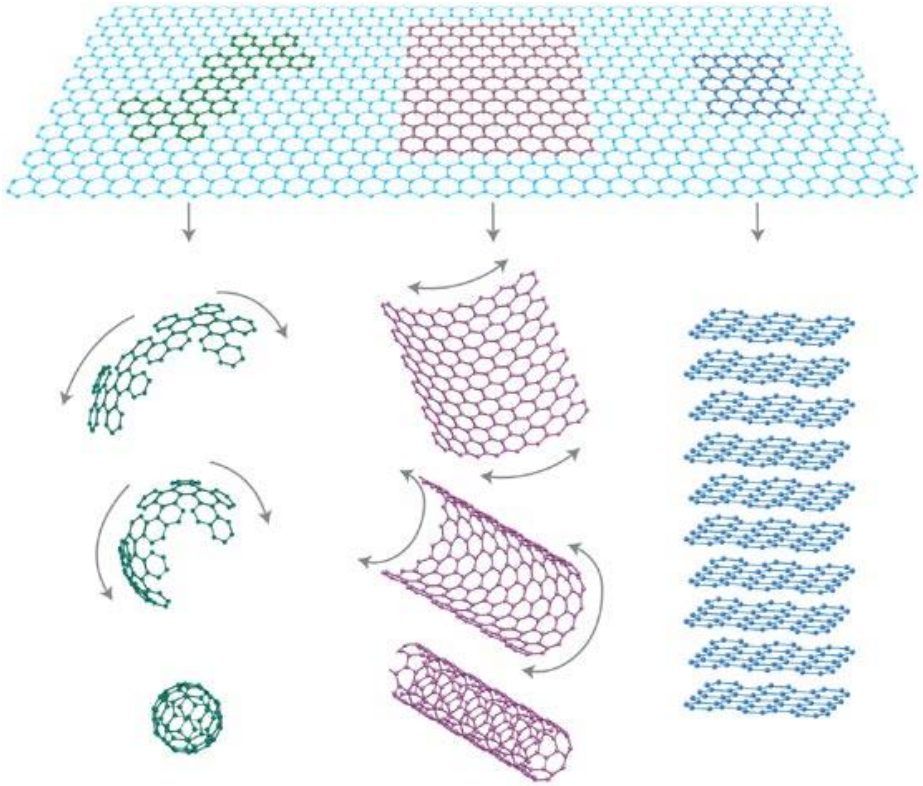

Figure 1.3 Quasi 2D material graphene as the source of all allotropes of carbon such as 0D bucky balls, 1D nanotubes or 3D graphite. (Image reproduced from Ref. [35])

On top of this graphene is very flexible. From nanoindentation experiments of freely suspended graphene it has been shown that it can withstand more than 20% strain applied to it before it undergoes permanent deformation [39]. In addition being thin and flexible

makes graphene a unique material among all other thin films and nanostructures. It has been estimated that the weight of an elephant would be necessary to break a sheet of graphene with the thickness of kitchen wrap [40]. Suspended graphene has been shown to acquire of charge carrier mobility up to 40, 000 cm^2/VS [41] at room temperature and 200, 000 cm^2/VS at low temperature [42, 43]. With such a high charge carrier mobility, graphene is not only the best conductor of electricity but heat as well. It is almost completely impermeable. With mass density of 7.4 x 10^{-19} Kg/μm^2, it is the lightest continuous thin film. Its potential is practically limitless from using it in condoms to cancer therapy, from flexible touch screen to super-fast batteries. Researchers are working on using it for desalination. Tennis rackets made up of graphene composites are strong, flexible and are already being used by international tennis players.

1.5 Introduction to Graphene based NEMS

Extreme stiffness, low mass, high Young's modulus and good conductivity of electricity makes graphene the most suitable candidate for NEMS materials as compared to any other thin film or nanostructures. While resonators based on SiN can exceed quality factors of 10^6 [44] but its mass is not as low as that of monolayer graphene. Over the years NEMS devices have shown high sensitivity based on nanostructures such as carbon nanotubes [15, 45-50], nanowires [51, 52]. Unlike other nanostructures such as carbon nanotube, nanowire graphene is an extremely stiff and strong continuous thin film. This allows graphene manufacturing to utilize the top-down fabrication process and is also compatible with the standard micro-nano fabrication techniques. At the same time

compared with bulk micro-machined structures such as Si, graphene can be grown over a large area [55, 56] and can be patterned at the wafer scale using the standard lithography process. Hence graphene avails advantages of both top-down and bottom-up fabrication processes and has a superiority over other NEMS materials. Table 1. 1 shows the performance of graphene mechanical; resonator –a comparison (adapted and extended from Hone *et al.* 2013 [57]).

1.5.1 Review of graphene-NEMS

Bunch *et al.* in 2007 demonstrated the first graphene mechanical resonator and studied its electromechanical properties [58]. Graphene was exfoliated from Kish graphite similar to the one reported earlier [35] and stamped on pre-patterned trenches of SiO_2 (260-330 nm) with gold pads connected at one end of the trench as metal electrodes. The length of these doubly clamped graphene resonators which is attached to SiO_2 surface by weak van der Waals force ranges from 0.5 µm to 10 µm with thickness of graphene from monolayer to multilayer (~ 50nm). Both electrical and optical actuation techniques were used to mechanically drive the resonator. For electrical actuation, electrostatic techniques were used to drive the graphene resonator by applying a combination of direct-current (DC) and radio frequency (RF) voltages between the gold electrode and Si. Silicon act as the gate with SiO_2 as the dielectric. The electrostatic force between the SiO_2 substrate and the suspended graphene produces motion in the graphene sheet. For optical actuation an amplitude modulated 432 nm diode laser beam (blue laser, Figure 1. 4) was focused on the suspended graphene. It drives the beam by periodic contraction and expansion of suspended graphene

due to the modulation of temperature of the graphene sheet. Optical interferometry was used to detect the motion of the oscillating graphene. Another laser beam (red laser, Figure 1. 4) was focused on the graphene sheet. A part of this laser is reflected back while the other passes through graphene. The laser beam passed through graphene reflects back

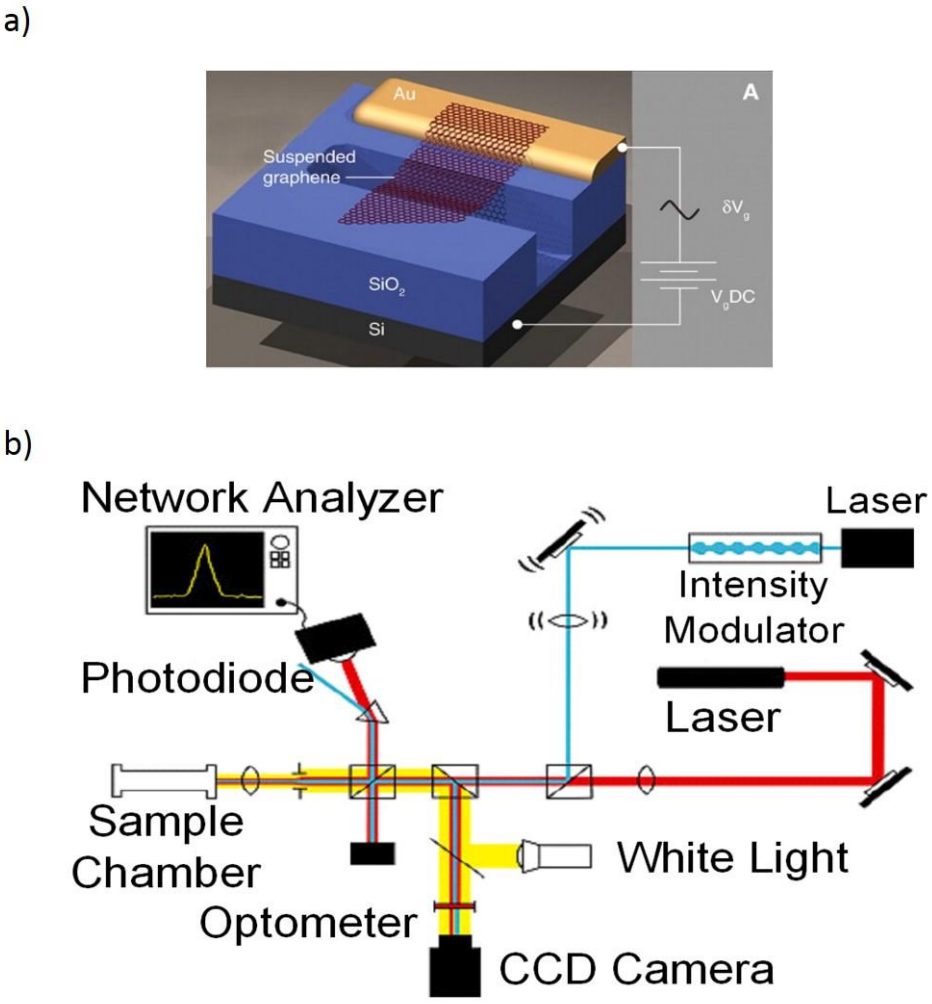

Figure 1. 4 a) Schematic of a suspended graphene resonator and electrical actuation scheme. b) Schematic of the experimental setup for optical actuation and interferometry detection technique. (Image reproduced from Ref. [58])

from the Si substrate (mirror) forming an interference pattern with the laser light reflected

from the graphene sheet. The changing position of oscillating graphene sheet changes the amplitude of intensity of the reflected signal. By monitoring the intensity modulation of the reflected signal using a photodiode and a network analyser, the motion of the graphene resonator was detected. Figure 1. 4 shows schematic of the device and the setup [58].

A year later, in 2008 D. Garcia-Sanchez *et al.* [59] used an AFM tip to not only measure the resonance frequency and deflection of graphene resonator but also image the spatial shape of the Eigen modes. The quality factor for this detection scheme was quite low as this was done in atmospheric pressure. Previous graphene resonator device structure [58] was used for this indirect optical detection technique using scanning force microscopy. This is discussed more in Chapter 3.

In 2008 J. Bunch *et al.* [60] demonstrated graphene to be a complete gas impermeable membrane using a graphene based drum resonator, where graphene is fully clamped (sealed) at all its edges. Atomically thick graphene trapped air in the etched hole in between the graphene membrane and backplane SiO_2/Si substrate. When the device was put into vacuum, the atmospheric pressure due to the trapped air in the etched SiO_2 hole covered with the graphene membrane caused the graphene sheet to bulge out forming a ''balloon''. It demonstrated the strength of monolayer graphene and its strong attachment with SiO_2 which does not break due to pressure exerted by trapped air on it. However, as the graphene-SiO_2 junction doesn't have a perfect seal hence the trapped air flows out slowly after around 24 hours of pumping.

Image of graphene resonator	Year	Graphene	Resonance frequency (f_o)	Room temperature Quality factor (Q)
	2007 (58)	Mechanically Exfoliated	70 MHz	78
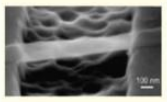	2008 (59)	Mechanically Exfoliated	18-85 MHz	64
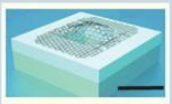	2008 (60)	Mechanically Exfoliated	66 MHz	25
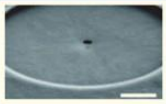	2008 (67)	Synthesised by reducing chemically graphene oxide	10-110 MHz	1,500-4,000
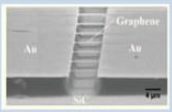	2009 (61)	Epitaxial (by SiC)	3-100 MHz	50-400
	2009 (61)	Mechanically Exfoliated	30-130 MHz	100
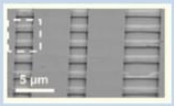	2010 (63)	Grown by CVD	5-75 MHz	250
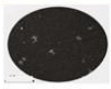	2011 (68)	Grown by CVD	4-12 MHz	2,400
	2013 (97)	Grown by CVD	52 MHz	4,015
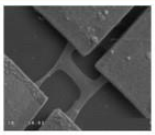	2015 **Present work [4]**	Grown by CVD	1-2 MHz	1500

Table 1. 1 Review of graphene mechanical resonators at room temperature. (Table reproduced from Ref. [57])

In 2009 C. Chen *et al.* [61] demonstrated for the first time the electrical transduction of graphene-NEMS using capacitive actuation and RF down mixing technique. This is now a widely used detection technique for graphene resonators [21, 62, 63]. Detailed discussions on this transduction technique is carried out in chapter 3. Unlike previous device fabrication processes [58-60], in this case exfoliated graphene was stamped onto a SiO_2/Si wafer instead of pre-patterned trenches and electrodes. Electrodes such as Au with adhesive layer Cr were patterned by electron beam lithography. This allows for the shaping of graphene using additional lithography processes. This is not only important and beneficial for fabricating symmetrical structures and different shapes and sizes, but also for allowing batch fabrication processes. But since for each graphene flake, designing and electrode alignment is required, this approach is quite slow. To suspend the structure, wet etching of the underling SiO_2 using hydrofluoric acid (HF) [43, 64] is carried out, which requires a special drying process known as supercritical drying. This prevents graphene from surface tension induced collapse after wet etching. Using this approach they could fabricate micron wide graphene resonators with small spacing between graphene and the gate (~100nm) and hence a high aspect ratio was achieved. However, it is difficult to fabricate fully clamped structures such as drum resonators using this process. Also because this is a top down approach, metal electrodes on top of graphene is also suspended due to uncontrolled etching underneath the SiO_2 [64].

Later in 2011 *Song et al.* [65] used another transfer technique for transferring graphene from one substrate to any other substrate using a polymer release layer instead

of using a scotch tape. This polymer transfer method has the advantage of moving individually suspended graphene flakes.

Moreover, to commercialize and allow applications of graphene-NEMS and demonstrate its potential in sensing devices such as force and mass sensors, the fabrication of graphene-NEMS should be done using scalable synthesis of graphene such as for example, graphene grown epitaxially, using graphene oxide, on transition metals using CVD process. In 2008 *Robinson et al.* [66] demonstrated fabrication of large-area mono and few layer Graphene Oxide (GO) films. Mechanical properties of these films were studied using drum resonators with quality factors as high as 4000. Later in 2009, *S. Shivaraman et al.* [67] demonstrated a method to fabricate doubly clamped free-standing graphene sheets with lengths up to 20 µm from epitaxial graphene on silicon carbide (SiC) substrate. An optical detection technique was used to actuate the graphene resonator and detect its motion. Photochemical etching of underlying SiC was used to suspend graphene after patterning electrodes and shaping graphene. In 2009 Li *et al*. [55] synthesized large scale high quality monolayer graphene on copper foils using CVD processes. A polymer support layer such as Polymethyl methacrylate (PMMA) or polydimethylsiloxane (PDMS) was deposited on the surface of the as-grown graphene on Cu. The copper was then etched away chemically. The polymer support layer/graphene was then transferred onto another substrate for device fabrication. In 2010 *Van der Zande et al.* [63] demonstrated fabrication of large arrays of doubly clamped, as well as fully clamped monolayer graphene membrane resonators using chemical vapour deposition (CVD). Doubly clamped resonators were

shaped into strips and then electrodes were patterned using standard lithography after transferring graphene onto SiO_2/Si and finally etching away underlying SiO_2 as discussed earlier. In another device fabrication process graphene on as grown Cu foil was shaped into strips and then transferred on top of predefined trenches and electrodes. Both optical and electrical detection techniques were used to detect the motion of these resonators. A year later in 2011 Barton *et al.* [68], demonstrated fabrication of a fully clamped circular mechanical drum resonators of diameters between 2-30 μm using graphene grown by chemical vapour deposition. These drum resonators showed quality factor one order higher than previously reported at room temperature. Table 1. 1 shows a comparison of the state-of-the-art of graphene mechanical resonator.

In this thesis CVD graphene has been used as for piezoresistor-NEMS device to showcase that graphene can itself act as a self-sensing layer, thus also allowing electrical sensing using the motion induced modulation of resistance (i.e. piezoresistive detection). Compared with NEMS based on other materials graphene NEMS are far more superior and display remarkable advantages [4]. By employing this piezoresistivity in a monolayer graphene resonator *to* transduce its motion in nanoelectromechanical systems (NEMS), I have achieved high quality factors, high onset of nonlinearity and thus exquisite force and mass sensitivity at room temperature. I discuss the design, finite element simulation, fabrication and characterization of the devices in Chapter 2. Piezoresistive measurements employed in this work are explained in Chapter 3 with experimental data and results. Various non-linear vibrations in the graphene NEMS have been explained with experim-

ental data and simulation results in chapter 4. Different resonance modes are discussed in Chapter 5 with modification in the frequency behaviour due asymmetry in the shape of graphene resonator. Summary and outlook of the future work is discussed in Chapter 6.

In the present work, the very first demonstration of piezoresistive sensing of graphene based nanoelectromechanical systems has been carried out. An astounding 0.95 – 1.54 zeptograms (10^{-21} g) of minimum detectable mass is estimated for such resonators at room temperature. Thermomechanical motion detection of these resonators allows us to estimate minimum force resolution which is extraordinarily low, 11.7 – 21.6 aN/Hz$^{1/2}$ also at room temperature. The basic understanding of nonlinearities in these devices and its origin have been carefully studied both experimentally as well as theoretically.

Chapter 2

Modeling, Fabrication and Characterization of devices

In this chapter I shall discuss Finite element method (FEM) modeling of devices, detail device fabrication processes and their characterization. Modal analysis is performed employing *Comsol Multiphysics* in order to predetermine the frequency range, which is of the same order of the experimentally measured resonance frequencies of the devices. Thermoelastic damping (TED) simulations are carried out to show comparisons between different designs of resonator. Fabrication processes of clamped H-shaped suspended graphene devices are explained. Standard device fabrication process as are developed with high reliability. Scanning electron microscopy was used to characterize these devices, to verify whether or not the graphene resonators are fully suspended. To check the quality of the graphene Raman spectroscopy was used, which confirms that graphene is monolayer.

2.1 Introduction to finite element method (FEM)

Finite element method (FEM), or finite element analysis (FEA) is a very effective numerical tool for solving a differential or integral equation describing different physical processes. It is used in modeling and simulation as a computational technique to obtain

approximate solutions of boundary value problems in various fields of science and technology. Solving the differential or integral equation analytically of a complex system with boundary and the initial conditions is otherwise very difficult. Hence, FEM is a very convenient and well-established technique for solving complex problems using computer coding.

2.1.1 General Procedure for Finite Element Analysis

The basic FEM procedure for computational modeling are: Modeling of the physical problem (geometry), specifying the boundary, initial and loading conditions, the finite element discretization of the geometry into small elements, and solving the resulting equations.

In general, real systems are very complex in structure and geometry. Hence it has to be reduced into a simpler and manageable geometry. For example curves and curved surfaces can be used to model curved parts of the geometry and its boundary. Also, linear elements, curve and curved surfaces are approximated using piecewise straight lines or flat surfaces. Figure 2. 1a shows H shape geometry of the resonator used in the present work.

Most real systems consist of many materials. Hence, the properties of elements need to be specified for each individual element. Different sets of material properties are required for different simulations. For example in structure mechanics applications the Young's modulus, Poisson's ratio and mass density of the material are required. Boundary,

initial and loading conditions vary from problem to problem and have to be specified as it plays a significant role in simulations.

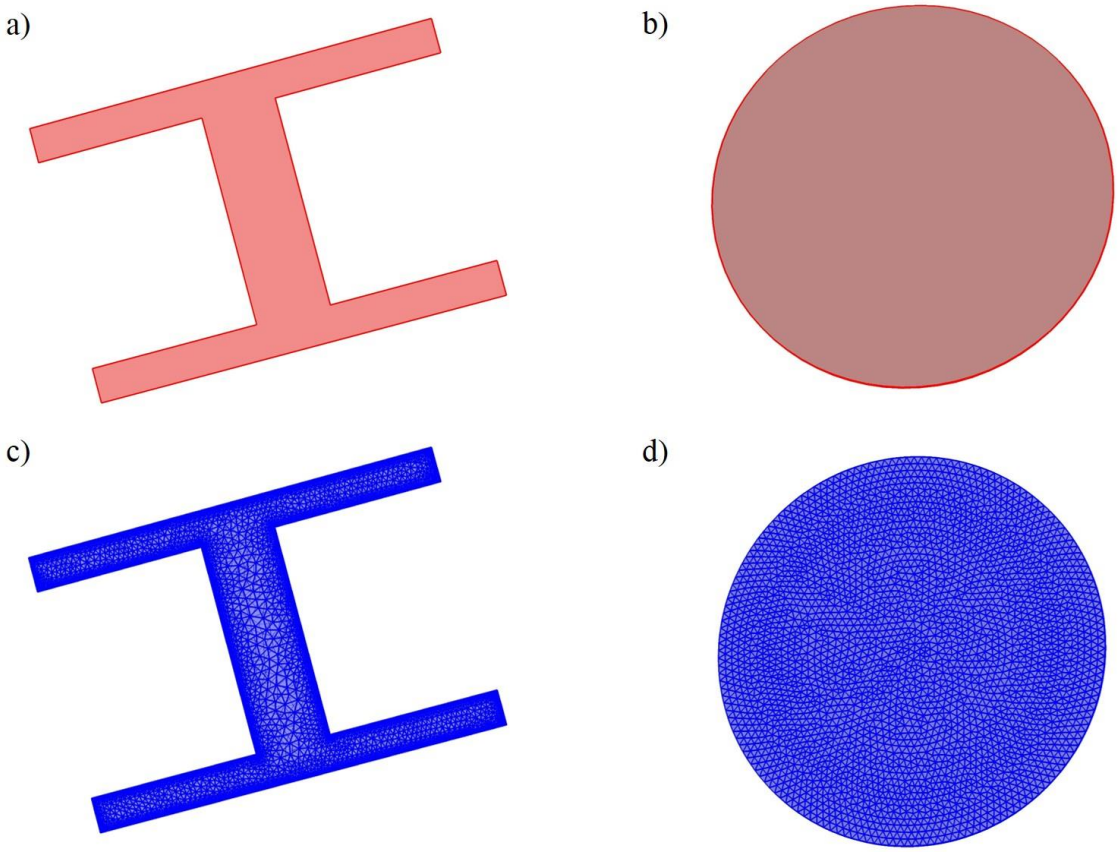

Figure 2. 1 a-b) The H shape and circular geometry of the resonator. c-d) Meshing of the above geometry using triangular element shapes

Domain discretization involves meshing to discretize the domain. The whole geometry is converted into small non-overlapping elements often called cells. Hence, domains having infinite degrees of freedom have been replaced by a system with finite degrees of freedom. A variety of element shapes such as triangular, quadrilateral etc. formed by connecting a certain number of nodes can be used for meshing the system. A

triangular element shape has been used in the present work, because of their flexibility in modeling complex geometries as shown in Figure 2. 1c-d. After creating a computational model, the discretized system is simulated.

Apart from all the advantages of FEM there are some limitations as well. The element size of the system should be always much smaller than the minimum feature size of the system. For smaller systems such as mono layer graphene where the minimum feature size (thickness) is a few angstroms, the element size should be angstrom or sub angstrom. Thus the number of elements will increase and accordingly the computational time will also increase. Hence often a massive parallel system is required for complex problem. Similarly for very large systems, the number of elements are massive and again a parallel computation is required.

2.2 Modal analysis of resonators [76]

Modal analysis using finite element methods (FEM) have been performed in order to predetermine the frequency range of the resonators. This analysis also serves to confirm that the stresses are concentrated at the legs of the H-shaped mechanical resonator. *Comsol Multiphysics* has been employed to carry out the simulations to calculate the resonance frequencies of the system.

Figure 2. 2a shows the resonance frequency of a double sided clamped rectangular beam graphene resonator, with varying length of the beam while keeping width of the

beam constant. An inverse square decrease in the resonance frequency is observed with increasing length as expected analytically. Figure 2. 2b shows resonance frequency of the beam with varying number of layers of graphene. A linear increase in resonance frequency is observed with increasing number of layers as expected analytically.

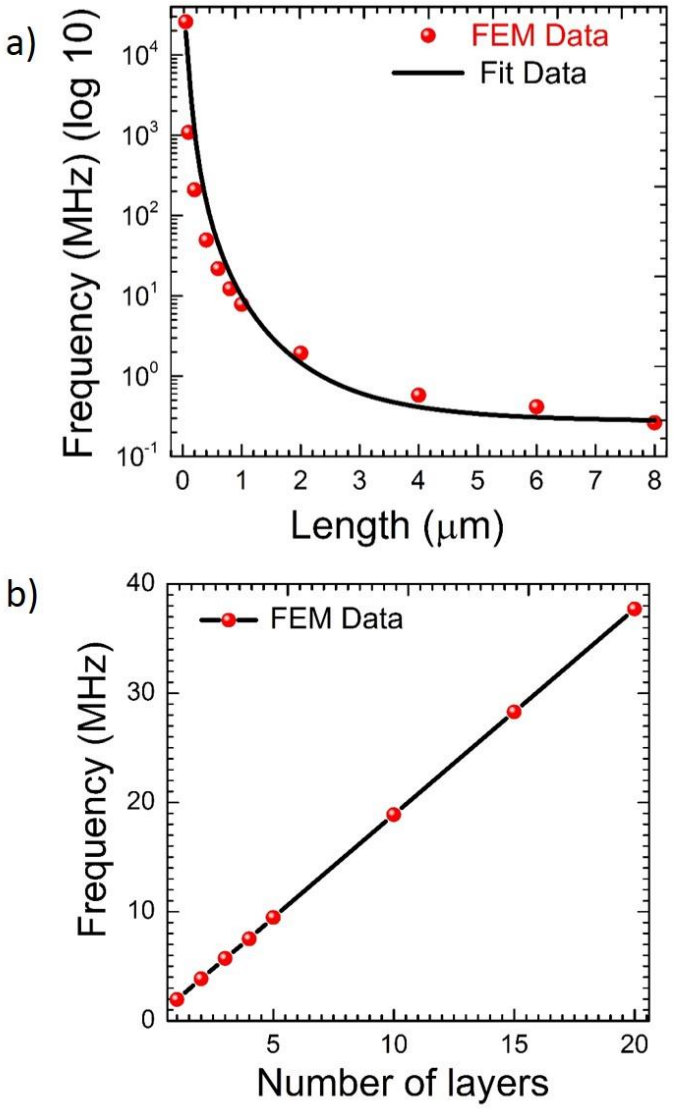

Figure 2. 2 a) The resonance frequency of a graphene resonator with varying length of the resonator at constant width. b) With varying number of layers of graphene

Figure 2. 3 a shows the deformed shape of a double sided clamped rectangular beam graphene resonator at resonance frequency. Figure 2. 3 b shows the fundamental mode shape of mechanical resonance frequency of the suspended graphene beams clamped at the four legs. Here, mass density of the beam (ρ) $= 2.5 \times \rho_{graphene}$, where $\rho_{graphene}$ = 7.4 x 10^{-16} g/μm^2 [61] has been considered. The fundamental resonance frequency (f_o) for this resonator which is approximately 1.8 μm long, 1.2 μm wide with each leg being ~ 120-150 nm wide and 0.7 μm long is calculated to be around 1 MHz using modal analysis. Resonance frequency (f_o) has been measured between 1-3 MHz for most of the resonators (devices on the same chip), this will be discussed in details in chapter 3. It has been found that these frequencies are of the same order as f_o calculated using FEM (Figure 2. 3 b) taking into account the higher mass density. Figure 2. 3 c shows the second modes (f_1) of the same device, the f_o of which is shown in Figure 2. 3 b.

Etching Silicon dioxide (SiO_2) underneath graphene using buffered oxide etchant (BOE) also etches 100-120 nm of SiO_2 underneath gold electrode pads which results in a small portion of the gold pads being suspended. The dimensions of this overhang are 100 nm thick (thickness of gold pads) and 120-150nm long. In order, to verify that observed frequency is not the vibration of these suspended gold electrodes, simulations have been carried out with this overhang. Figure 2. 3 e shows that the first mode of this gold overhang is around 1 GHz. Thus, the resonance frequency of the graphene resonator is much lower

than that of the suspended gold. Therefore, there is expected to be no contribution from the gold electrodes to the first few modes of the graphene resonator, other than to serve

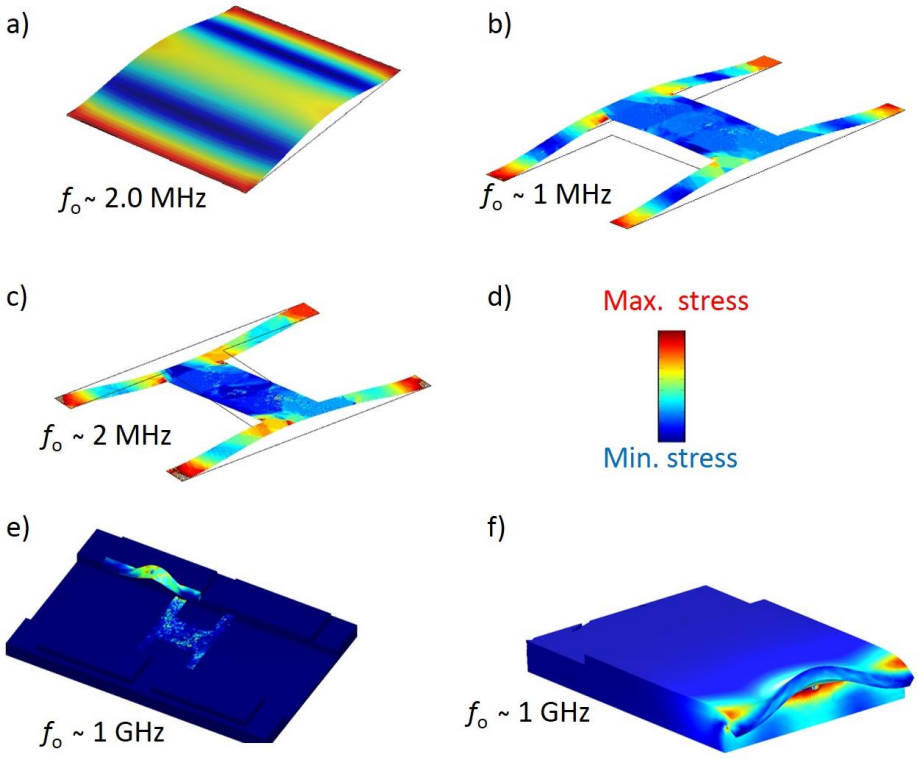

Figure 2. 3 a) The deformed shape of a double sided clamped graphene resonator at fundamental resonance frequency. b) The fundamental mode shape of one of the suspended graphene beams clamped at the four legs at mechanical resonance frequency. c) The second modes (f_1) of the same device, the f_o of which is shown in figure 2.2b. d) The colour code of amount of stress. e) The first mode of the gold overhang in the device. f) Modal analysis of the same gold over hang (modeled separately).

as a modified clamped support. This supports the contention that the resonance frequency, which has been measured at around 1-3 MHz for most of the devices is that of suspended graphene. Further simulations have been carried out of just the gold pad with the overhang as shown in Figure 2. 3 f and the result remain the same.

2.3 Modeling Thermoelastic Damping (TED)

For small mechanical systems one of the main sources of energy dissipation is the thermoelastic effect. As the resonator vibrates, stress is produced in the beam and hence, the local volume is changed which leads to a temperature gradient across the resonator. Due to the thermal gradient, heat dissipation from hotter region of the resonator to colder region takes place to bring the resonator back to the thermal equilibrium state. Hence, energy dissipation due to the heat flow causes damping of the resonator which is often called thermoelastic damping (TED) [77-81]. In 1948, Zener *et al.* first proposed this theory, which was later advanced in 2000 by Lifshitz and Roukes *et al.* for thin vibrating beams. It explains that TED is directly dependent on the temperature of the resonator at f_o.

Figure 2. 4 shows TED simulation of a double sided clamped beam (Figure 2. 4 a), and a clamped H shape beam (Figure 2. 4 b) using *COMSOL multiphysics*. It has been observed that the temperature gradient is produced across the beam. Maximum temperature gradient is from clamp to the central portion of the beam and vice-versa. Since, the area in an H shape resonator has been reduced, hence the temperature gradient in the beam is also reduced to a great extent. Furthermore, TED is comparatively smaller in the H shaped resonator than a double sided clamped resonator of the same dimension. Hence the quality factor is higher for the H shape resonators compared to the double sided clamped resonator of same size. Hence, it can be concluded that the H shape resonator has

a lower TED compared to double side clamped resonators and thus has a higher quality factor.

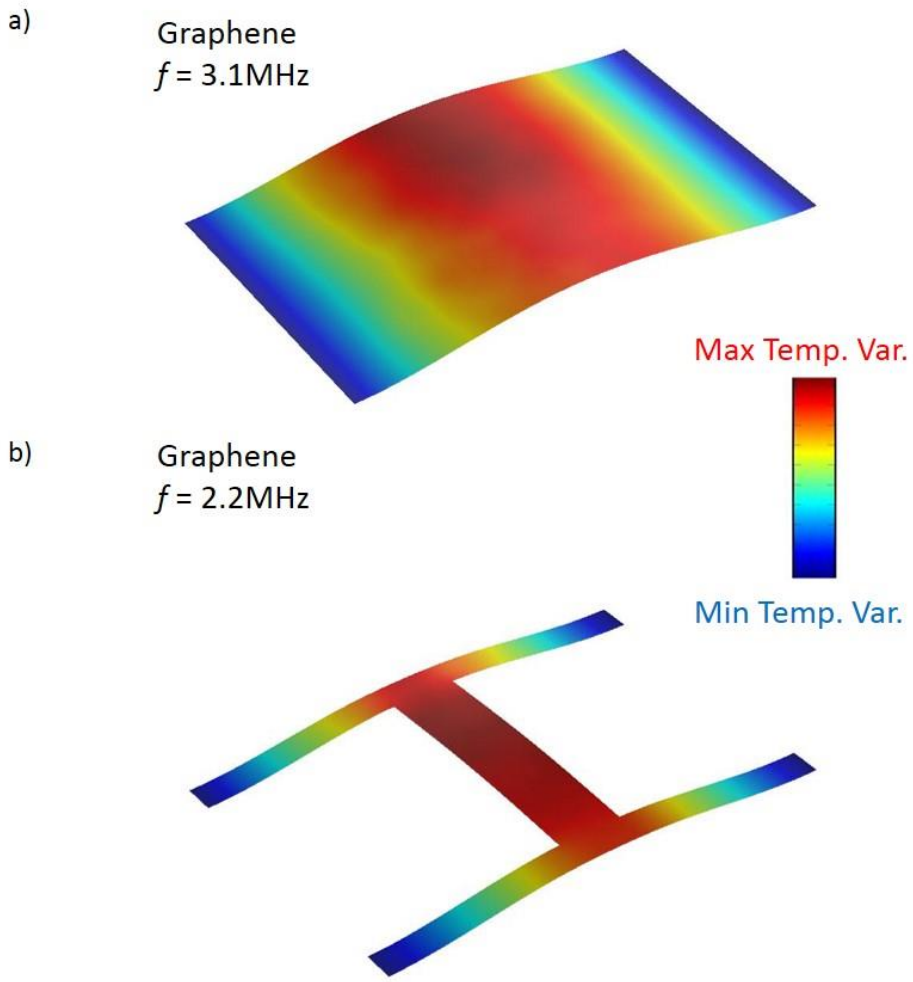

Figure 2. 4 TED simulation of resonators showing temperature of resonator at mechanical resonance frequency for a) double sided clamped and b) four sided clamped H shape graphene

2.4 Fabrication of suspended graphene

As discussed earlier, the present work focuses on studying graphene based NEMS, using a mechanical actuation technique and utilizing the intrinsic piezoresistivity of graphene as a self-sensing component. To increase the sensitivity due to the intrinsic piezoresistive effect, a four-sided clamped H shaped suspended graphene beam has been employed. Fabricating a two sided clamped beam itself is very challenging. Hence, fabricating a H shaped beam where the clamping area is less than 80% compared to two sided clamped beam was even more challenging. So, for these nanoscale devices, an environment as clean as possible for all the device fabrication process have been maintained. Hence, the entire fabrication process is performed in a Class 100-1000 clean room facility, which provides a suitable condition for micro/nano device fabrication. To achieve a resolution of around 100 nm feature size, standard e-beam lithography based device fabrication processes were used to fabricate fully suspended H shaped graphene resonators. A standard device fabrication process has been explored for this, which works reliably. Figure 2. 5 shows a schematic of different device fabrication processes for making a fully suspended H shaped graphene resonator. E-beam lithography and plasma etching is performed on CVD grown graphene on a 285nm SiO_2 substrate (bought from Graphene Supermarket) for patterning H shaped graphene. Another e-beam lithography step is performed to pattern the metal electrodes followed by a metallization process of thermally evaporating 5nm Chromium (Cr) as an adhesion layer and 90nm Gold (Au) as metal

electrodes. Finally, Graphene is suspended by under-etching SiO_2 using BOE [43, 61]. To prevent the suspended graphene membrane from collapsing during the drying process due to surface tension effects, critical point drying has been employed [43,61].

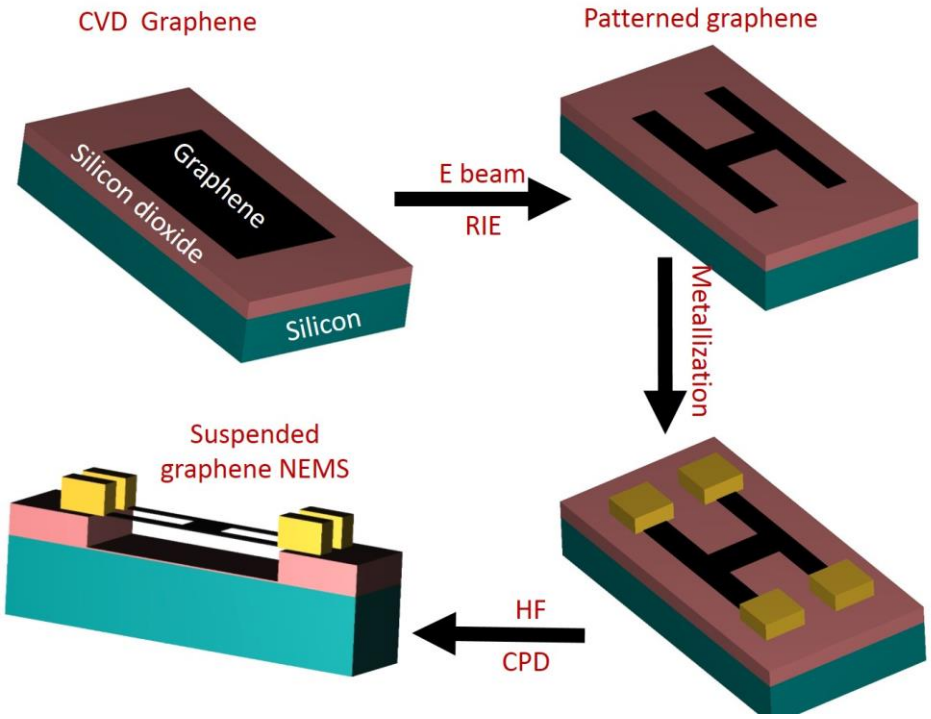

Figure 2. 5 Schematic diagram of fabrication process

2.4.1 Patterning alignment markers

A 300 nm thin film of PMMA-495 (Poly-methyl Methacrylate), an electron sensitive compatible polymer resist is deposited on CVD grown graphene on a 300nm SiO_2/Si substrate using a spin coater at 4000 rpm (revolutions per second) for 60 seconds, followed by post baking at 175˚C for 10 minutes. At a constant time, the thickness of a resist is inversely proportional to the speed of rotation. However, beyond a certain threshold speed, the thickness of the resist remains constant. Patterning of the alignment markers is done

by e-beam writing of a computer aided design (CAD) file which contain the particular alignment markers on the sample. Figure 2. 6 a shows a schematic of the pattern of these markers. E-beam resists such as PMMA are long chains of cross linked polymer. It is a positive e-beam resist, so by exposing the selected area (alignment markers) of the resist by e-beam, its solubility in a particular chemical dedicated for the resist called developer increases. Hence, by putting the sample in the developer for a certain time, the region of the resist exposed to the e-beam gets dissolved in the developer.

For my devices, the resist has been developed after e-beam exposure developer for 15 seconds and then rinsed in IPA for 60 seconds to remove any residue. The developer

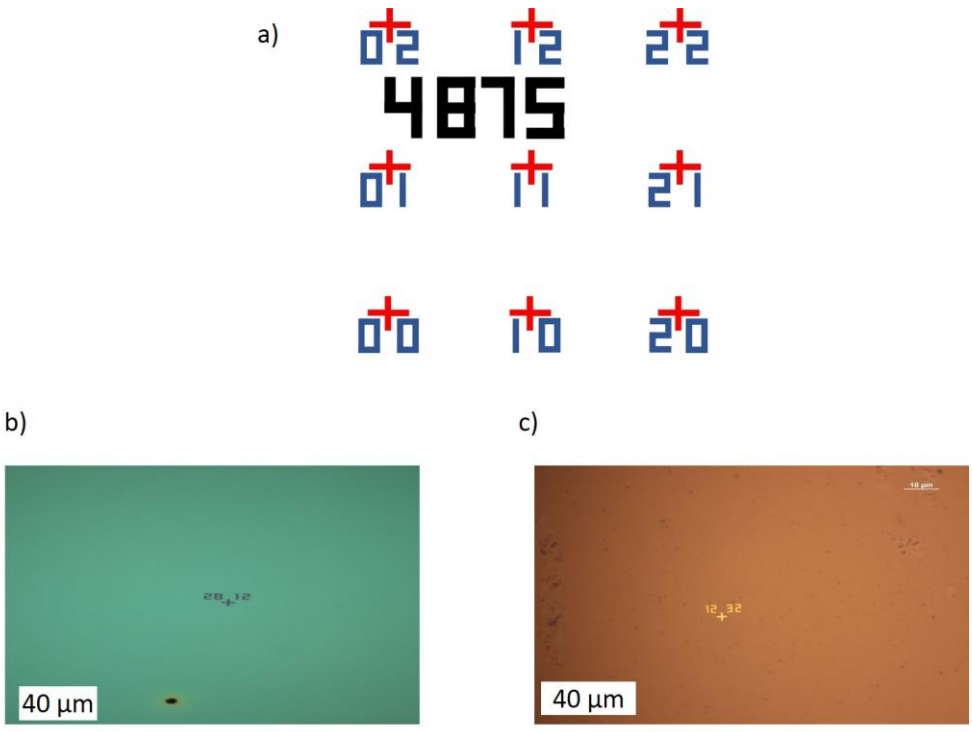

Figure 2. 6 a) Schematic of pattern of markers. b) Optical microscope image of markers, after developing resist. c) Optical microscope image of markers, after metallization and lift-off.

used in this case is a solution of 1:3 MIBK (Methyl isobutyl ketone) : IPA (Isopropyl Alcohol). The time to keep the exposed resist in the developer is very precise. It can be over or under developed if it is kept for longer or shorter period (few seconds) respectively. Figure 2. 6 b shows an optical microscope image of markers, after developing resist on a sample. Metallization of the alignment markers was done by depositing 10 nm Cr followed by 60 nm gold using a thermal evaporator without breaking the vacuum at a rate of 0.1 nm per second. Cr acts as an adhesion layer for gold to adhere better to the sample. Lift-off process was performed by keeping the sample in warm acetone (40 °C) for 2-3 hours, followed squirting it with acetone, using a pipette, until fine features of the alignment markers can be seen under an optical microscope followed by rinsing in IPA. Figure 2. 6 c shows an optical microscope image of markers, after metallization and liftoff.

2.4.2 Patterning H shape graphene

E-beam patterning of H shaped graphene is performed as explained above. Plasma etch or reactive-ion etching (RIE) is performed on the sample using 10 standard cubic centimetres per minute (sccm) Ar, for 20 seconds, at 10 Watt RF power. H shaped graphene on the device, being protected by the resist layer is not affected by the plasma. The rest of the graphene, being exposed and unprotected is etched away by plasma. Remaining resist is removed by keeping the sample in warm acetone for 10-20 min and rinsing it in IPA. Figure 2. 7 a shows an optical image of device after e-beam patterning of H shaped

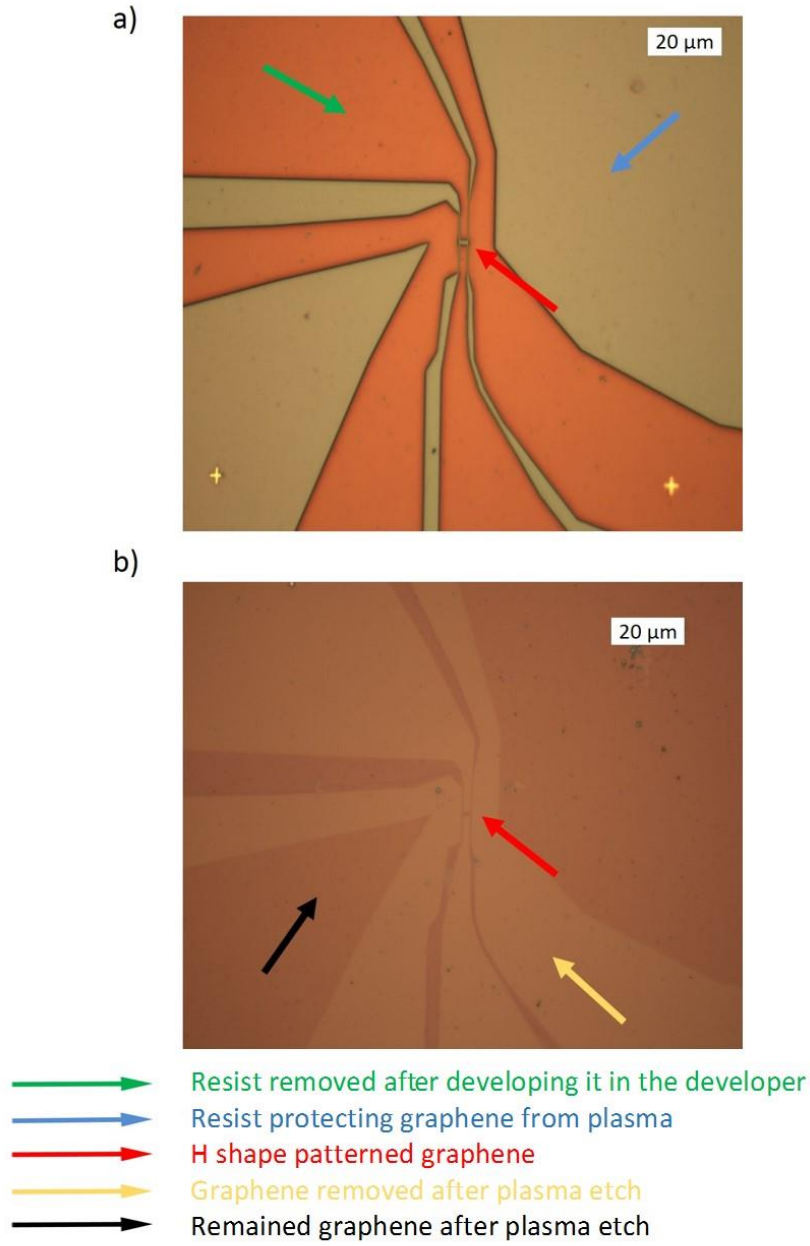

Figure 2. 7 a) An optical image of a device after e-beam writing and developing the resist for plasma etch. b) An optical image of the same device after plasma etching of unprotected graphene followed by removing PMMA.

graphene followed by developing the resist for plasma etch. Contrast between the areas of

resist removed after developing and area of resist protecting graphene can be seen quite clearly. Figure 2. 7 b shows an optical image of the device after plasma etching of graphene and removing PMMA. Contrast between H shaped patterned graphene and rest of the area where graphene is removed after plasma etch is quite visible.

2.4.3 Patterning Metal contact pads

As explained earlier, metal contact pads were patterned using another e-beam writ-

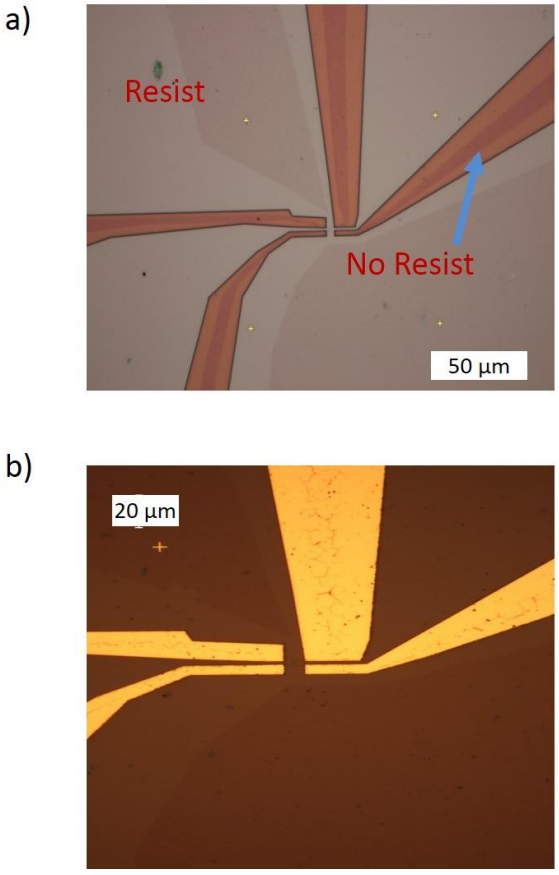

Figure 2. 8 a) An optical image of device after developing resist for metal contact. b) An optical image of device after metallization and lift off.

ing step followed by developing the resist. Metallization of the contact pads is done as explained earlier by depositing 10 nm of Cr as an adhesive layer, followed by 90 nm of gold using thermal evaporation without breaking the vacuum at a rate of 0.1 nm per second. The lift-off process of the unexposed resist and metal on top of it was performed as before. Figure 2. 8 a shows an optical image of the device after developing the resist for metal contact pads. Figure 2. 8 b shows an optical image of the device after metallisation and lift off.

2.4.4 Releasing graphene using HF etching of SiO_2 [43 61, 62]

The last step is to suspend the device. To suspend the device, selective etching the region beneath the graphene flakes (SiO_2) has been performed in such a way that the electrodes remain intact. BOE has been used, which selectively etches only the oxide layer but not the silicon (Si). BOE is a solution of 1:6 volume ratio of 49% Hydrogen Fluoride (HF) in water buffered with 40% Ammonium Fluoride (NH_4F) in water. This solution has been calibrated to etch at a rate of 1 nm/sec. The chip is placed into the solution for two and half minutes to etch away around 150 nm. Since the etching is isotropic, it etches the SiO_2 beneath the metallic contacts also. After the etching, thorough rinsing with deionised water (DI) is undertaken to remove any remains of BOE. The sample is kept in DI water for 2-3 hours to ensure there is no BOE residue. The device is never exposed to air directly since, exposing to air will result in a sudden change of surface tension force resulting in a collapse device.

2.4.5 Critical point drying of devices [43, 61, 62]

To prevent the device from collapsing due to surface tension, while drying the chip by exposing it to air, critical point drying (CPD) has been used. The critical point for any given substance is that point beyond which the true gaseous/liquid nature of the substance

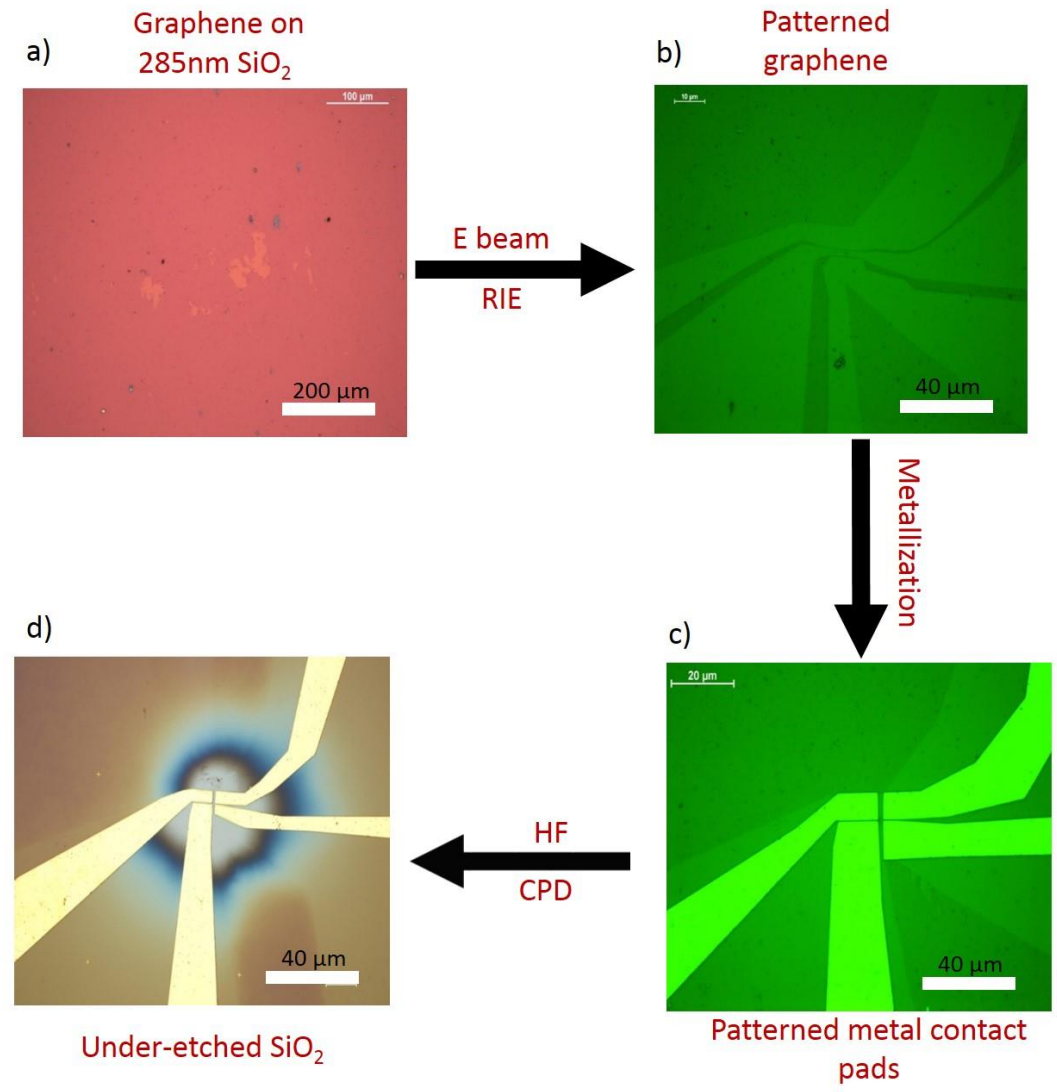

Figure 2. 9 Optical images of real fabrication processes.

vanishes. This state is called the super-fluid state. Critical point for Carbon dioxide (CO_2) is at around 31.1 °C and 73 atm. Beyond this point CO_2 exists as a super-fluid. The advantage with this region is that there are no surface effects beyond this region and the transition from a liquid to a super-fluid occurs without any surface tension. Figure 2. 9 d shows an optical image of the device after HF etching and CPD. Figure 2. 9 summarizes all fabrication process of suspended graphene discussed in section 2.4 using optical images of the processes. Starting from patterning H shape graphene, depositing metal electrodes, releasing graphene by under etching SiO_2 and finally drying the sample using CPD.

Scanning electron microscopy (SEM) has been used to characterize the devices. Figure 2. 10 shows SEM images of the graphene resonators after CPD. Figure 2. 10 a shows a SEM image of a collapsed graphene device. Figure 2. 10 b, shows an SEM image of a partially collapsed resonator. The difference in contrast between the SiO_2 substrate and suspended portion of graphene distinguish it from collapsed graphene where there is hardly any contrast between the SiO_2 substrate and graphene. Figure 2. 10 d-e shows SEM images of fully suspended H shaped graphene resonators with different dimensions. Difference in the contrast between SiO_2 substrate and graphene shows that graphene is fully suspended. Figure 2. 10 c shows SEM image of several devices on one chip. Using CVD graphene and standard lithography processes the device fabrication process can be easily up scaled. From SEM images suspended and non-suspended regions can be readily identified.

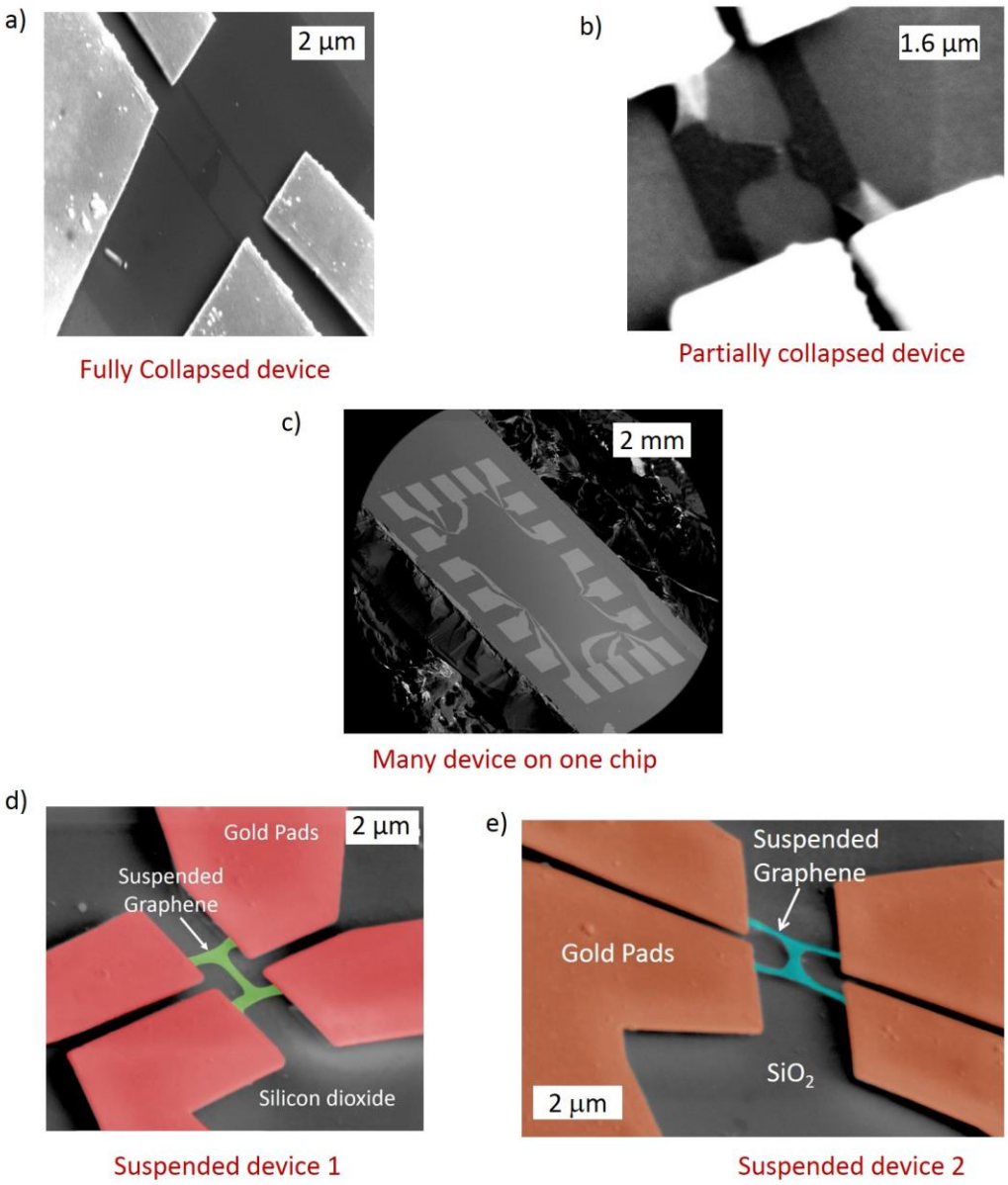

Figure 2. 10 a) SEM image of a collapsed resonator. b) SEM image of partially suspended graphene devices (tilted) after critical point drying. The difference in contrast between collapsed (central area) and suspended portion (two legs) of this resonator is clearly visible. c) Several devices on one chip. d) SEM image of a fully suspended graphene resonator. Difference in contrast between the substrate and graphene clearly shows that graphene is fully suspended. e) Another suspended graphene device with different dimensions.

2.5 Raman Spectroscopy of Graphene [82-83]

Raman spectroscopy has been historically used to characterize carbon based materials such as graphite. Apart from structural characterization, it is a very powerful tool to understand the behaviour of electrons and phonons in graphene. It is a very useful spectroscopic technique to distinguish monolayer graphene from few-layer graphene. It can also determine precisely the number of layers in few-layer graphene film. Due to the extensive study of graphene by Raman spectroscopy over the last decade, the Raman spectrum of graphene is very well understood [82-83]. Raman spectroscopy has been used in this work to characterize graphene and to confirm its monolayer nature prior to the fabrication of devices.

2.5.1 Raman Spectrum of Graphene [83]

The Raman spectrum of monolayer graphene has two most prominent features - the so called G band at around 1582 cm^{-1} and G' band appearing at 2700 cm^{-1} using a laser of 2.41 eV excitation energy. Another band, the so-called disorder-induced D-band at around 1350 cm^{-1} which is half of the frequency G' band can also be seen for a disordered sample. Hence, the D-band is also associated with the defect in the sample. Since G' is at about twice the frequency of D-band, it is also called 2D band in most of the literature. In order to avoid confusion between G', and G, the G' is addressed as the 2D band in line with most of the other authors. Figure 2. 11 shows a Raman spectrum of graphene showing the main features- the D, G and G' band with a laser excitation energy of 2.41 eV.

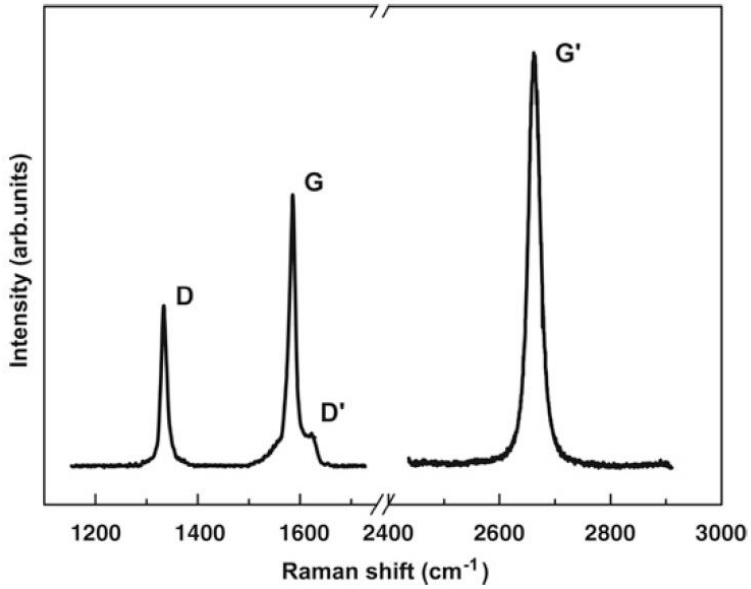

Figure 2. 11 Raman spectrum of a graphene, showing the main Raman features, the D, G and G' bands taken with a laser excitation energy of 2.41 eV. [83]

Figure 2. 12 [83] shows the line shape of the 2D band of graphene describing the evolution of the 2D band with the number of graphene layers. The 2D band of monolayer graphene is a single Lorentzian peak. As the number of layers increases, the 2D band continues to evolve with distinct bands for each number of layers up to four layers, conforming to that of many layered graphene or bulk graphite (Figure 2. 12 e). Therefore, the 2D band can be used to determine the number of layers of graphene in the film.

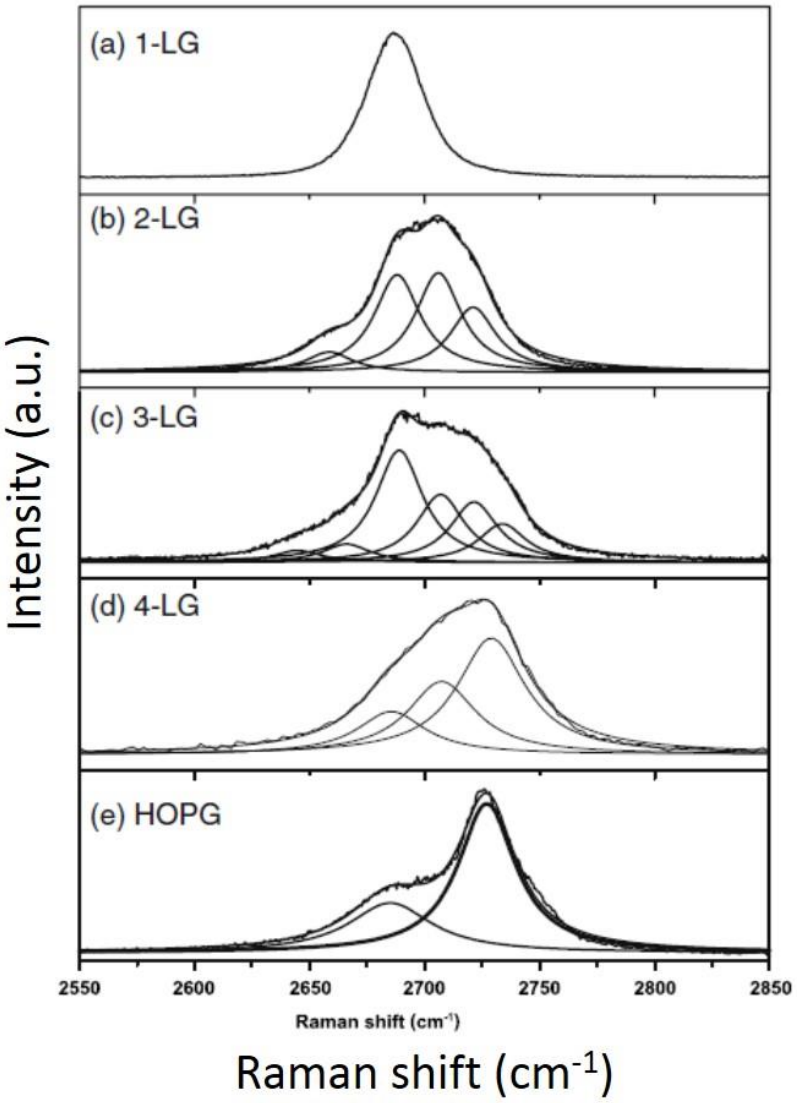

Figure 2. 12 The measured G' Raman band with 2.41 eV laser energy for (a) 1-layer graphene (LG), (b) 2-layer graphene (LG), (c) 3-layer graphene (LG), (d) 4-layer graphene (LG) and (e) Highly oriented pyrolytic graphite (HOPG). The splitting of the G' Raman band opens up in going from mono to three layer graphene and then closes up in going from 4-LG to HOPG. (Image reproduced from Ref. [83])

2.5.2 Interpretation of the Raman spectrum of graphene

One of the effective ways to distinguish monolayer graphene from few-layer graphene is by comparing the relative intensity of the 2D band to that of the G band (I_{2D}/I_G). Figure 2. 13 shows comparison of Raman spectra of graphene synthesized on Cu foil and transferred on a SiO_2/Si substrate for different number of layers of graphene [55]. With the decrease in the number of layers in the graphene film under four layers, the relative intensity of the 2D band to that of the G band (I_{2D}/I_G) increases as shown in Figure 2. 13 . With mono layer graphene I_{2D}/I_G is always more than one and for multilayer graphene or bulk graphite it is very small.

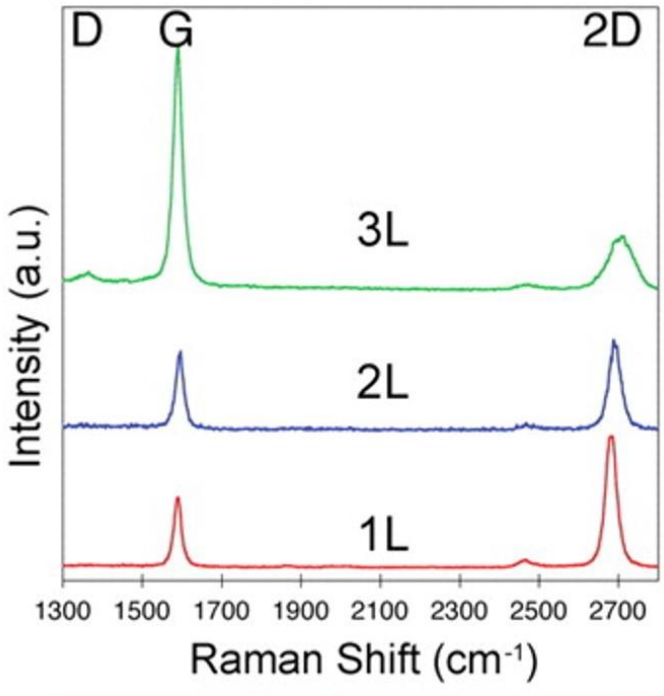

Figure 2. 13 Raman spectra of monolayer graphene (red) bilayer graphene (blue) and tri layer graphene (green) grown by CVD process and transferred to a SiO2/Si substrate using a 532 nm (2.33 eV) laser [55].

For this work a laser beam of wavelength 532 nm is used for the Raman spectroscopic measurements reported in this work. Figure 2. 14a shows the Raman spectrum of one of the graphene devices with D, G and 2D band peaks. Intensity of the 2D band peak is higher than the G band peak indicating monolayer graphene with some defects

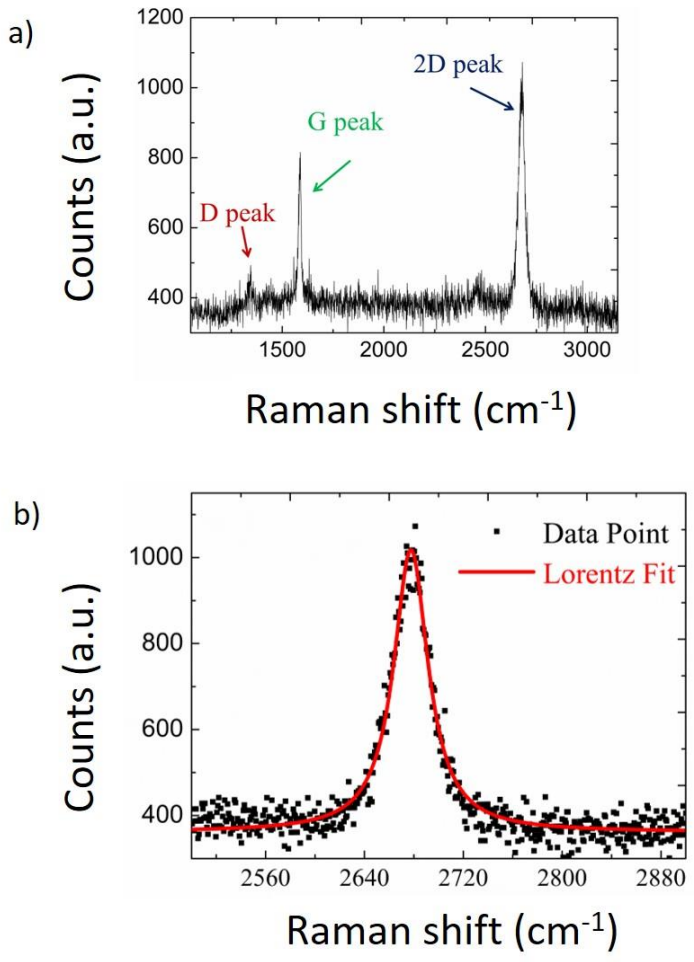

Figure 2. 14 Raman spectra of monolayer graphene. a) Raman spectrum of a graphene device showing D (red), G (green) and 2D (blue) band peaks. b) Single Lorentzian fit (red solid line) to the 2D band.

as shown in the D peak. Figure 2. 14b shows a single Lorentzian fit to the 2D band and ratio I_{2D}/I_G at around 1.8 confirming monolayer graphene.

2.6 Conclusions

To increase the sensitivity due to the instrinsic piezoresistive effect, I have made use of the higher stress concentrations near the base of a mechanical resonator, where the resistance change is most pronounced. I have thus employed a four-sided clamped H shaped graphene beam, which allows us to measure across the regions of maximum stress near the supports of the mechanical beam to maximize the piezoresistivity. Modal analysis shows that the leg area has the highest stress using finite-element-methods. Thermoelastic damping (TED) simulations show the superiority of H shape design resonator over double sided clamped beam regarding thermal damping in the resonators. I have used chemical vapour deposition grown monolayer graphene to fabricate all side clamped H-shaped suspended graphene devices, using standard device fabrication process. I verify that the devices are suspended using SEM imaging. I employ Raman spectroscopy to confirm that the graphene is monolayer prior to fabrication.

Chapter 3

Piezoresistive sensing of graphene resonator

Taking measurements of nanoelectromechanical resonators at their resonance frequencies can be challenging. This is because the signal generated from the very small mechanical motion of the device is minuscule and is buried in other parasitic or interference signals. The readout methods used should possess efficient signal transduction from the mechanical motion to the electrical signal and should also be suitable for a wide range and high frequencies (MHz) [22]. In this chapter, a piezoresistive readout method for graphene based resonators starting from externally (mechanically) driven resonators to thermally driven (no external drive) resonators are discussed. These are the first reported measurements of such a detection technique in the otherwise well studied graphene-NEMS field.

3.1 Overview of the previously used transduction techniques

There are various sensing methods for MEMS/NEMS resonators such as capacitive, optical, microwave, piezoelectric, piezoresistive etc. Similarly, there are various actuation methods such as optical, electrostatic, mechanical, using AFM tip etc. Among them, capacitive, optical detection techniques, and AFM tip (Amplitude modulation) have been used for the detection of the motion of graphene resonator.

3.1.1 Overview of the Optical detection technique [58]

The optical detection technique is based on optical interferometry. An amplitude modulated laser beam is focused on suspended graphene. The graphene is being periodically set into motion due to heat produced by the laser beam. Another laser beam is used to detect its motion. A part of this laser beam reflects back while rest passes through the suspended graphene sheet and is reflected back from the substrate (Si) which acts as a mirror, thus forming an interference pattern. This reflected laser beam is sensitive to the motion of the suspended graphene sheet. Hence, motion of the suspended graphene can be measured by detecting modulation of the intensity of the reflected laser beam using a photodiode and a network analyser. Figure 1.6 shows a schematic of the optical interferometry detection technique for measuring the motion of a graphene resonator [58]. This method was used in the very first detection of the motion of a graphene resonator by Bunch *et al.* in 2007 [58]. Later, other groups [60, 66-67] have used this technique to transduce the motion of graphene. However, this method requires a large and complicated experimental setup. This restricts the use of this technique where low temperatures and a high magnetic field is required.

3.1.2 Overview of the capacitive sensing [61]

In the capacitive detection method graphene is electrostatically actuated and the current through the periodically driven graphene resonator measures the motion of the graphene sheet. Figure 3. 1a shows a schematic of a suspended graphene resonator used

for the electrostatic detection technique. Graphene acts as a channel in the Field effect transistor device, where it is connected to the source and the drain and is suspended over the gate electrode. Graphene is actuated electrically by applying an RF signal and a DC voltage to the gate. The DC voltage applied to the gate produces static deflection in the

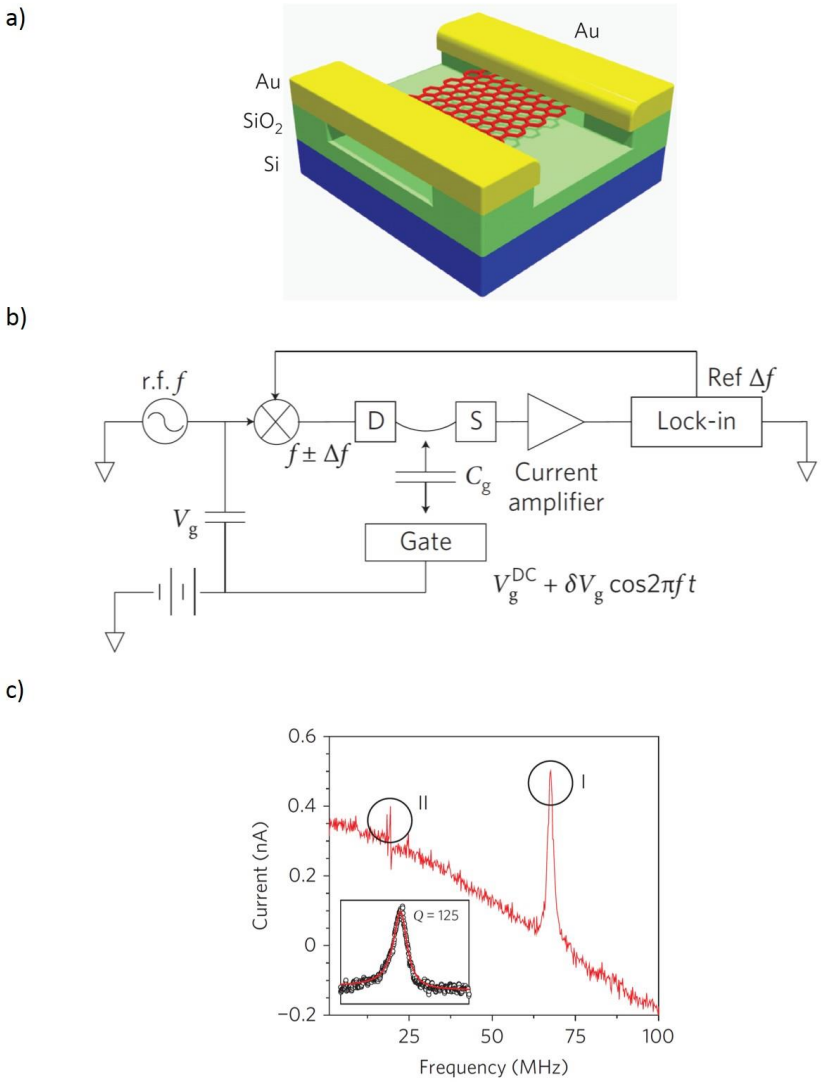

Figure 3. 1 Capacitive sensing of graphene nanoelectromechanical resonator. (Image reproduced using ref. [61]). a) Schematic of the device. b) Schematic of circuit used in capacitive sensing. c) Mechanical resonance frequency of graphene (I) and metal beam (II). Inset: the graphene resonance peak with Q = 125.

beam or away from the gate. The RF signal to the gate produces an electrostatic force due to the capacitance between the resonator and the gate which drives the beam at its resonant frequency. The motion of the beam is transduced by the current passing through the graphene sheet. In 2009 Chen *et al.* [61] showed an electrostatic detection method for sensing the motion of a graphene resonator. Figure 3. 1b [61] shows a schematic diagram of the capacitive sensing method used for the graphene resonator. One of the advantages of this technique is that because the deflection in the graphene is dependent on the applied gate voltage, the frequency of the graphene resonator can be tuned. Due to the high charge carrier mobility in graphene, the resonance frequency of a graphene resonator is highly tuneable with applied gate voltage. But electrostatic actuation generally damps the motion of graphene and thus the quality factor at room temperature goes down. One of the other disadvantages of this technique is that because a high gate voltage needs to be applied to the device to deform the beam, it causes additional tension in the beam and changes the natural resonance frequency of the resonator. This makes it very difficult to measure the natural resonance frequency. Figure 3. 1c shows frequency response of graphene resonator using capacitive sensing with quality factor of 125 [61].

Due to electrostatic actuation, additional tension in the beam is produced. It has been shown that due to electrostatic gating [61] the extra tension T_e produced in the beam is a function of the DC gate voltage (V_g). The resonance frequency of this detection technique is given by equation 3.0, where T_o is the built in tension, ρ is mass density

$$f(V_g) = \sqrt{\frac{T_0 + Te(V_g)}{\rho w}} \quad (3.0)$$

($\rho_{graphene} = 7.4 \times 10^{-19}$ gm/μm²) and $T_e \alpha V_g^{4/3}$ and hence $f \alpha V_g^{2/3}$ [61]. Hence the fundamental resonance frequency increases significantly due to the measuring technique.

3.1.3 Overview of the detection technique using AFM tip: [59]

Another detection technique used for graphene resonators is using an AFM tip to measure the motion of graphene. In this detection method graphene is generally actuated by an electrostatic method i.e., by applying an RF signal to the gate as discussed above. The motion of graphene is detected by the AFM tip. Resonance frequency of the AFM tip is used to modulate (Amplitude Modulation) the RF signal applied to the gate. Hence the AFM tip drives at the modulated frequency and measures the motion of the graphene beam due to interaction between graphene and the AFM tip. Quality factors are generally very low in this technique as this is done mostly in air. However, it can be used to image the mode at the resonance frequency which is quite difficult to do using other detection techniques. Also this is probably the most direct method of measuring graphene deflection at the resonance frequency.

3.2 Overview of piezoresistive sensing: [4, 92-93]

Lord Kelvin discovered the piezoresistive effect in 1856. When a mechanical stress is applied to any material, its electrical resistivity changes. This effect is called piezoresistivity. Many commercial devices such as pressure sensors and accelerometers utilise

piezoresistivity. In micromechanical pressure sensors, deformation of a diaphragm due to changes in pressure is transduced into electrical signals using piezoresistors. Piezoresistive sensing of micromechanical accelerometers is based on the change in resistance of a piezoresistor due to acceleration induced by stress.

Piezoresistive sensing in general uses a simpler measuring circuit as compared to the capacitive sensing which requires more complex circuitry. The other advantages of piezoresistive sensing over capacitive sensing are its fairly linear response [5], and that it is very robust and simple to implement.

3.2.1 Piezoresistive effect

Let's consider the electrical resistance of a bar:

$$R = \rho \frac{L}{A} \tag{3.1}$$

where ρ is the resistivity of the material, A is the cross sectional area, and L is the length of the bar. Unlike electrical resistance *(R),* electrical resistivity *(ρ)* is independent of the geometry of the conductor and is a property of the material itself making it a useful quantity to compare electrical properties of different materials. When the conductor is deformed, its resistance changes. The fractional change in resistance can be calculated by taking the partial differentiation of equation 3.1 as shown in equation 3.2.

$$\frac{\partial R}{R} = \frac{\partial \rho}{\rho} + \frac{\partial L}{L} - \frac{\partial A}{A} \tag{3.2}$$

The first term $\partial\rho$ is due to the change in the material's electrical resistivity, the second term dL is due to change in the length, and the last term ∂A is due to change in cross sectional area of the bar. As can be seen from equation 3.2, change in resistance is due to material and geometrical changes. Hence piezoresistive effect exists in all materials but is more effective only for materials that possess high relative change in resistivity ($\partial\rho/\rho$). Otherwise the output signal ($\partial\rho/\rho$) would be too weak to detect efficiently.

The piezoresistive coefficient π is the change in resistivity due to applied stress on the material and is expressed as the fractional change in resistivity ρ per unit stress (τ).

$$\pi = \frac{\partial\rho/\rho}{\tau} = \frac{\partial\rho/\rho}{ES} \tag{3.3}$$

$$\frac{\partial\rho}{\rho} = \pi_1\tau + \pi_2\tau^2 + \pi_3\tau^3 + \pi_4\tau^4..... \tag{3.3a}$$

Where τ is applied stress, π_i is the i[th] order piezoresistive coefficient, E is Young's modulus, and S is the strain. Second and other higher terms of the right hand side of the equation 3.3a [84] contribute to the nonlinear piezoresistivity. Similarly, the resistance-strain relationship of a piezoresistive material can be characterized by a figure of merit called gauge factor GF, defined as the fractional change in resistance divided by the applied strain (S) can be expressed as:

$$GF = \frac{\partial R/R}{S} = \frac{dR/R}{\partial L/L} \tag{3.4}$$

if ν is the Poisson's ratio of the material then using:

$$\frac{\partial A/A}{\partial L/L} = -2\nu$$

Hence (3.2) can be written as:

$$\frac{\partial R}{R} = \frac{\partial \rho}{\rho} + \frac{\partial L}{L}(1 + 2\nu) = GF\frac{\partial L}{L} \tag{3.5}$$

Hence the Gauge factor GF can be expressed in terms of ν, ρ and strain produced in the conductor due to applied stress:

$$GF = (1 + 2\nu) + \frac{\partial \rho/\rho}{\partial L/L} \tag{3.6}$$

$$GF = (1 + 2\nu) + \frac{d\rho/\rho}{S} \tag{3.6}$$

Replacing $\frac{\partial \rho/\rho}{S}$ from (3.3) into (3.6), GF can be expressed in terms of ν , ρ , E and π:

$$GF = (1 + 2\nu) + E\,\pi \tag{3.7}$$

The term $E\pi$ in equation 3.7 is due to material properties and $1 + 2\nu$ is due to geometrical changes. Equation 3.7 shows that gauge factor is a dimensionless figure-of-merit. Also GF depends only on the strain produced in the materials, as other terms ρ, E and ν are characteristics of the materials and hence remain constant. The bulk value of Poisson ratio, Gauge factor and resistivity of common metals are listed below in the Table 3. 1 from [85-86]. Poisson ratios of most of the materials ranges from 0 and 0.5, as can be seen from Table 3. 1. Hence from equation 3.7 the first term of $GF(1 + 2\,\nu)$ which is purely responsible

for geometrical changes ranges from 1 to 2. Hence all the materials which possess high GF have most of the changes in resistance due to their material ($GF \sim E\pi$) property.

Metal	Poisson's ratio (ν)	Gauge factor (γ)	Electrical resistivity (ρ) μΩ.cm
Cu	0.35	1.96	1.7
Au	0.42	3.03	2.2
Al	0.34	2.17	2.65
Pd	0.39	2.23	10
Pt	0.39	2.54	10.6
Ni	0.30	1.88	7.0

Table 3. 1 The bulk value of Poisson ratio, Gauge factor and resistivity of common metals [85-86]

3.2.2 Piezoresistivity in thin films

The Piezoresistive behaviour of metals and semiconductors [87-90] is very well known. In semiconductors, applied mechanical stress, produces deformation, which changes the band structure and charge carrier distribution in the band. Hence the mobility and the effective mass of free carriers changes, which ultimately results in the change of resistivity (piezoresistance). In semiconductors this change is affected by doping and temperature. It has also been shown that piezoresistivity of thin films (less than 10 nm) is large compared to that of the bulk [88, 91]. For example Gauge factor of bulk gold as mentioned in the above Table 3.1 is around 3 whereas for 3 nm gold thin film is reported as high as 24 to 48 [91]. This is because electrical conductance is very sensitive to induced

strain which changes the separation between particles in a thin film. Thus piezoresistivity is very effective in semiconductors and it increases greatly as thickness of thin film is decreased below 3 nm. Because graphene is a one atom thick material, it is very sensitive to strain induced in it and hence it can be an ideal candidate for very high sensitive piezoresistive sensing.

3.2.3 Piezoresistivity of Graphene [69-75]

In 2010 Lee *et al.* [69] showed how graphene based stretchable strain sensors perform, with a gauge factor of around 6.1 on a wafer scale. This opens up a new area of research which was never before explored and also shows the potential for applications in strain gauge sensors, mass sensors etc. They fabricated a graphene based strain sensor on a PDMS substrate and showed that when 1% strain was applied, the change of resistance was from 492 Ohm (Ω) to 522 kΩ, which they repeated more than a hundred times. The corresponding gauge factor is found out to be 6.1 which is far more than conventional strain gauges based on alloys. A year later Huang *et al.* [70] in 2011 measured a gauge factor of 1.9 for suspended graphene using nano-indentation experiments by introducing homogeneous tensile strain in the beam. Even under a high strain only a small change in electrical resistance was observed. In the same year Chen *et al.* [71] measured a high gauge factor of 150 for a graphene-based piezoresistive strain gauge on SiO_2. The strain gauge was fabricated using mechanically exfoliated graphene sheets on SiO_2 and patterned electrodes for electrical measurements. A year later in 2012, H. Hosseinzadegen *et al.* [72] used

graphene films as a piezoresistive element in MEMS device and reported giant piezoresistivity of 1.8 x 10^4. They measured the GF for graphene by placing it on highly strained SiN membrane and measured the change in resistance in response to an applied strain. The reason for this giant GF is that in graphene the electrons are confined to 2D [35], so even a small amount of strain can greatly modify the band structure, which causes this large change in resistance. The very same year Zhao *et al.* [73] demonstrated an ultra-sensitive strain sensor based on nanographene (NG) films deposited on a mica substrates. An approximately inverse proportional correlation between the thickness and the conductivity was found. A gauge factor (GF) over 300 for the graphene-based strain sensors was reported. A high GF is due to the very high sensitivity of conductivity of the NG films to the applied strain. A year later in 2013 Smith *et al.* [74] used a nanoelectromechanical membrane structure to demonstrate the piezoresistive effect in graphene which can readout pressure due to applied strain on the membrane. They showcased that ultra-thin graphene based pressure sensors have orders of magnitude higher sensitivity per unit area compared with the conventional pressure sensors based on silicon and Carbon nanotubes (CNTs). An average value of gauge factor for the suspended graphene was estimated using a finite element simulations to be 2.92 which is higher than previously reported values [70]. Recently Zhao *et al.* [75] have shown that a graphene based strain sensor on a flexible substrate has a very high Gauge factor of 600 with a long life time of more than 10, 000 cycles. Hence piezoresistance of graphene can be measured successfully. This could

provide a new transduction. mechanism for graphene resonators in the frequency domain, making piezoresistive transduction more attractive and superior over other transduction methods used earlier such as optical and electrostatic transduction.

3.3 Piezoresistive measurements

In the piezoresistive transduction scheme, the strain-dependent resistance produced in the piezoresistive material due to the applied stress is measured. However, there is no way to measure the change in resistance directly. So I converted the change in resistance into an electrical signal by applying a known current through the piezoresistor and measured the voltage drop across it. One of the main advantages of piezoresistive sensing is the ease of measuring dc resistance.

3.3.1 Piezoresistive transduction using external actuation

Figure 3.2 shows a schematic of the electrical circuit diagram for the piezoresistive sensing of a graphene resonator (piezomechanically actuated). The electrical readout

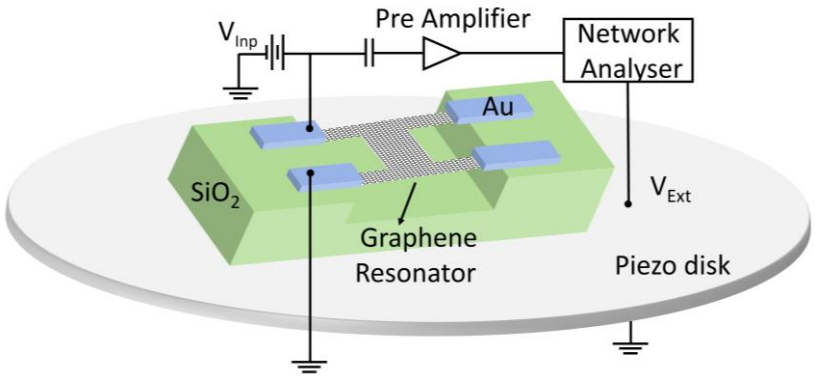

Figure 3. 2 Schematic of the circuit used for externally driven piezoresistive transduction.

method utilizes the piezoresistivity of graphene as a self-sensing component for NEMS. A DC bias (V_{Inp}) is applied to two adjacent legs of the resonator to convert the resistance variation to a voltage signal, which is amplified with a preamplifier (MITEQ AU1442), and the frequency response of the beam is measured with a Lock-in amplifier (Zurich Instruments HF2 with UHS option). All measurements are carried out at high vacuum (> 10^{-6} T) to increase quality factor.

Figure 3. 3 shows broadening of the resonance peaks and a slight deviation towards the lower frequency with increasing drive amplitude (V_{Ext}). It indicates decrease in the spring constant (capacitive softening) [26, 62, 65, 94-95] and quality factor. There are differences between devices, for example, device 1 (Figure 3. 3a) is more non-linear when compared to device 2. In device 1 at V_{Ext} = 2V, resonance peak depart from Lorentzian shape as shown in Figure 3. 3a, whereas in device 2 there is less change in f_0 with V_{Ext} (Figure 3. 3 b). Hence device 2 operates fairly in the linear regime compared with device 1. Non-linearity in NEMS and its onset is of concern particularly for mass sensing, where the dynamic Range of a device sets the minimum resolvable mass, and I discuss this in later section 3.6.1. Decrease in the resonance frequency with V_{Ext} indicate that the devices may have some slack [96] probably due to use of CVD graphene. Depending on the amount of slack in each device, the effect may not discernible.

Graphene displays a negative coefficient of thermal expansion [61-62]. Essentially, this would entail that as V_{Inp} is increased, more power is dropped across the graphene

resonator, which would heat the resonator; hence, the resonance frequency would be expected to go up for a resonator under tensile stress. As shown in **Error! Reference source not found.** I indeed observe this behavior in both device 1 and 2 where a slight increase in resonance frequency is observed as I increase the input DC bias (V_{Inp}) to the device.

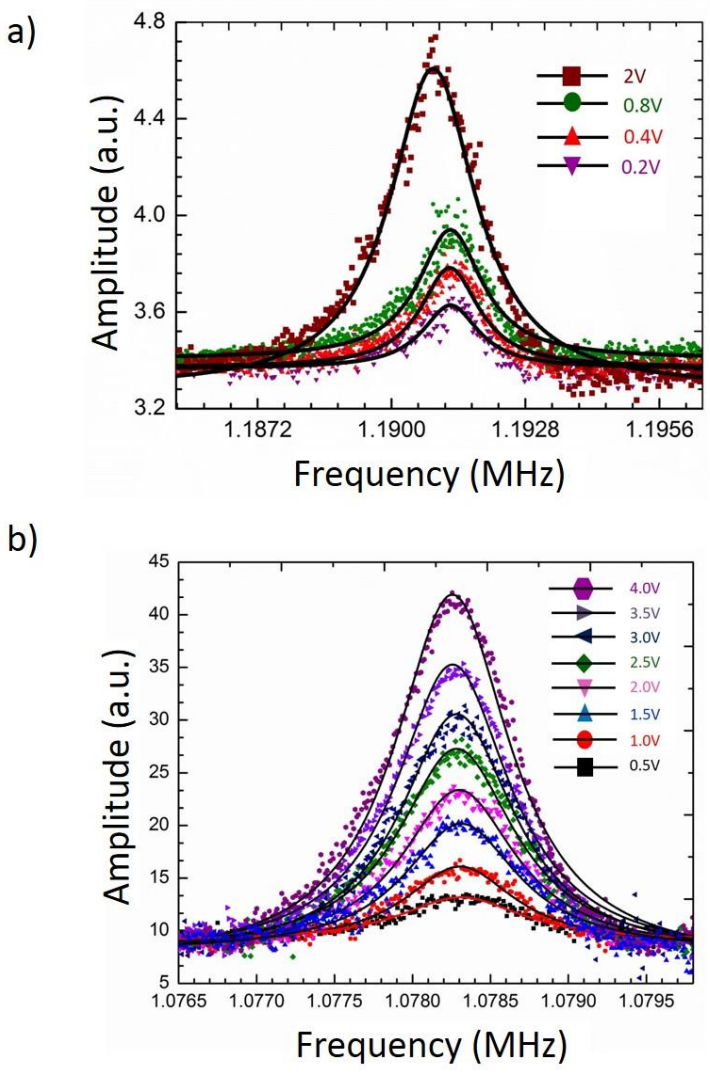

Figure 3. 3 a) The resonance frequency response of device 1 with different V_{Ext} and constant V_{Inp} = 75mV. b) The resonance frequency response of device 2 with different V_{Ext} and constant V_{Inp} =

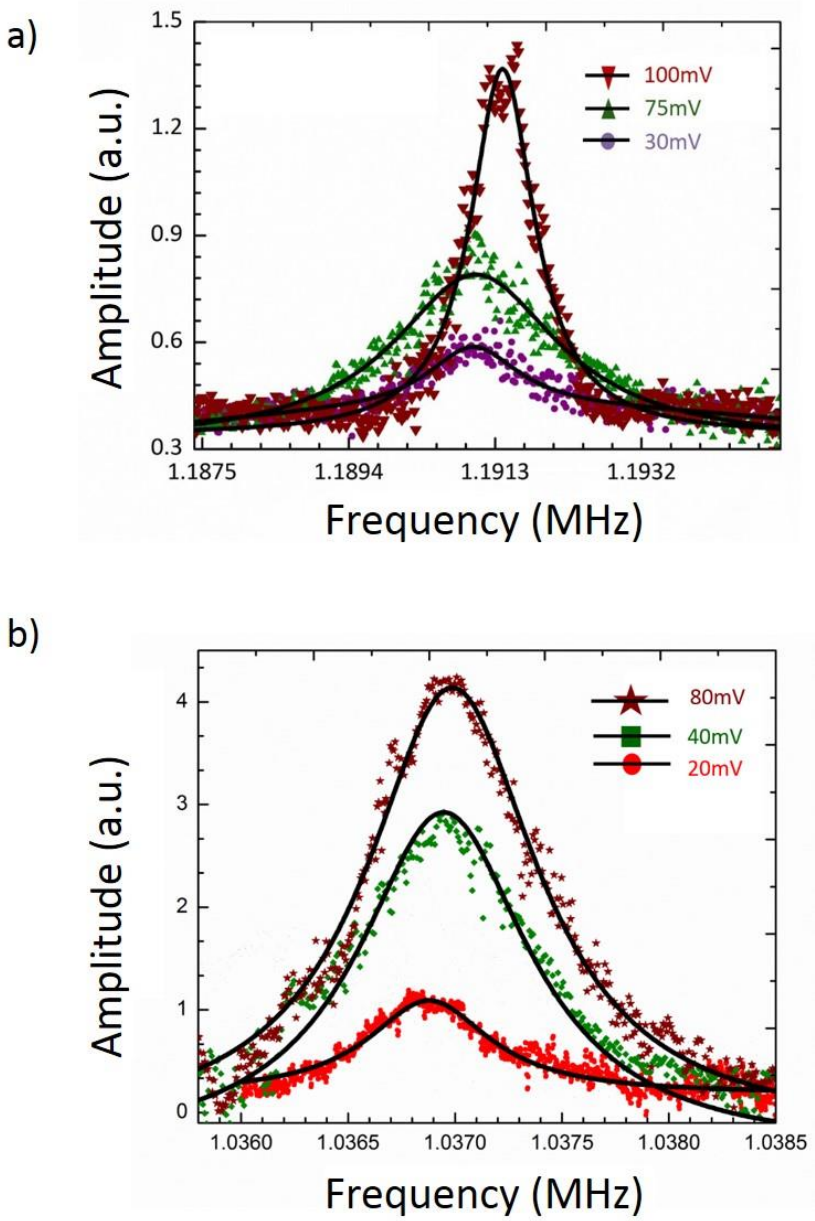

Figure 3.3 a) Variation of amplitude at f_o at different V_{Inp} and constant V_{Ext} = 2V (Device 1). At V_{Ext} = 2V, for V_{Inp}= 100mV Device 1 shows quality factor of the order of 10^3. b) Variation of amplitude at f_o at different V_{Inp} and constant V_{Ext} = 6V (Device 2). Device 2 also shows quality factor of the order of 10^3.

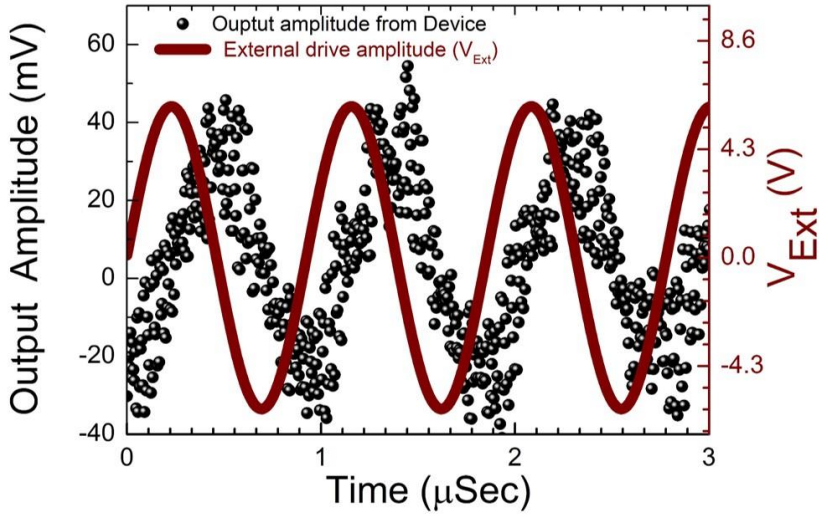

Figure 3. 5 Time domain output signal (black data points) for device 1 at $V_{Ext}(f_o)$ = 6V, and V_{Inp} = 20 mV with respect to the input to the piezomechanical drive (red solid line).

I have also measured the time domain signal of the resonator when being driven at the resonance frequency. It is studied, not only to highlight the exceptional sensitivity of this measurement scheme at room temperature, but also because such signals can have applications, for example as self-sustaining mechanical oscillators [97]. Figure 3. 5 shows the time-domain output signal (black data points) of the device 2 for $V_{Ext}(f_o)$ = 6V, and V_{Inp} = 120mV (whose resonance is shown in Figure 3. 3b) with respect to the input to the piezo-mechanical drive (red solid line). Figure 3. 6 shows the schematic of the electrical circuit diagram for the time domain signal from device. I drive the device piezo-mechanically at f_o using a signal generator and measure the time domain signal from the device using an oscilloscope. Figure 3. 7a shows the variation of amplitude of the signal (sinusoidal fit) with time for different $V_{Ext}(f_o)$, at V_{Inp} = 20mV. It is seen that the amplitude of the signal

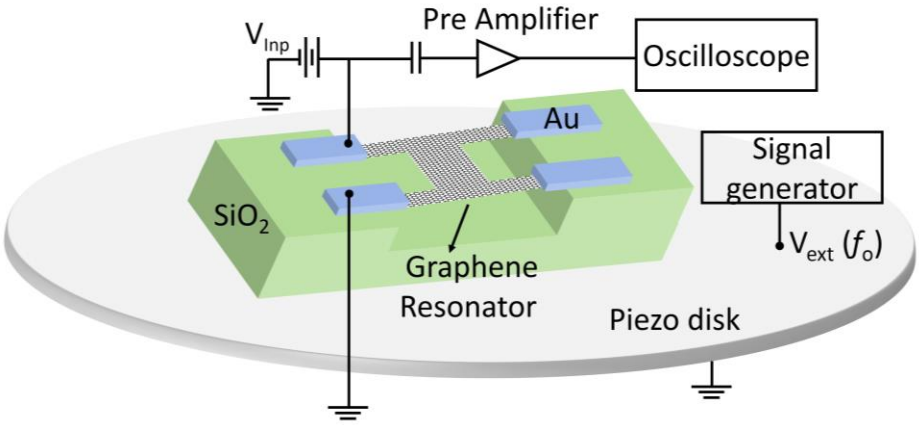

Figure 3. 6 Schematic of the circuit used for time domain signal measurements.

increases, with slight increase in phase as I increase $V_{Ext}(f_o)$. Figure 3. 7b shows the fast Fourier transform (FFT) of this signal, indicating that the first amplitude coefficient is at the frequency of the mechanical resonance as expected and shown in Figure 3. 3a. Increasing $V_{Ext}(f_o)$ at constant V_{Inp} results in a corresponding increase in the amplitude of the coefficient as expected.

My measurement, unlike capacitively detected graphene resonators [24-26], employs piezoresistivity, which would contribute to a unique condition for monolayer resonators; the schematic in Figure 3. 8a-c illustrates this condition. My resonators are expected to always be under tension when perturbed from their equilibrium position as shown Figure 3. 8b, which is in contrast to conventional piezoresistive sensors, where a thin piezoresistive layer on a mechanical beam as shown in Figure 3. 8a, is the transducing element. Thus, unlike conventional piezoresistive sensors, my measurement does not result in the graphene changing from a tensile to compressive stress when perturbed as shown in

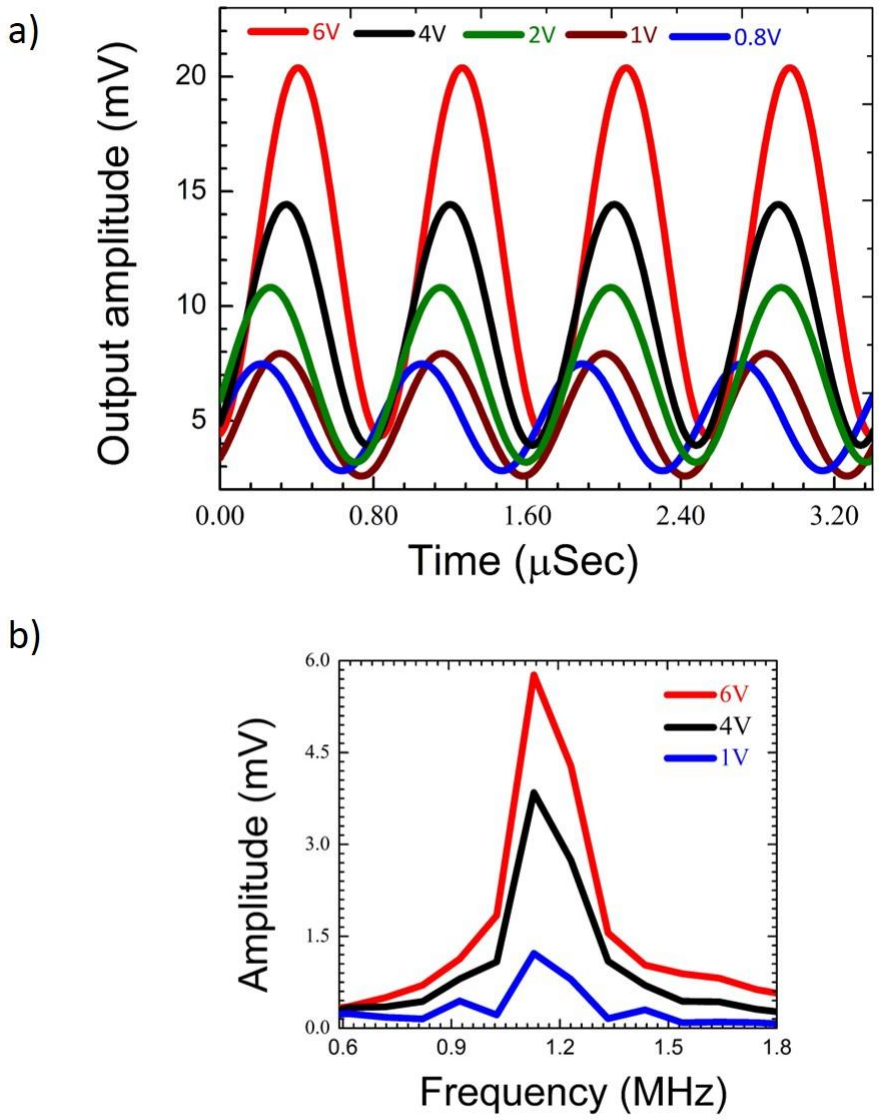

Figure 3. 7 a) Sinusoidal fit of the time domain output signal of device 1 with different $V_{Ext}(f_o)$ and constant V_{Inp} = 20mV, showing change in phase (non-linearity) and increase in amplitude as I increase V_{Ext}. b) First FFT coefficients of the time domain output signal of device 1 with different $V_{Ext}(f_o)$ and constant V_{Inp} = 20mV.

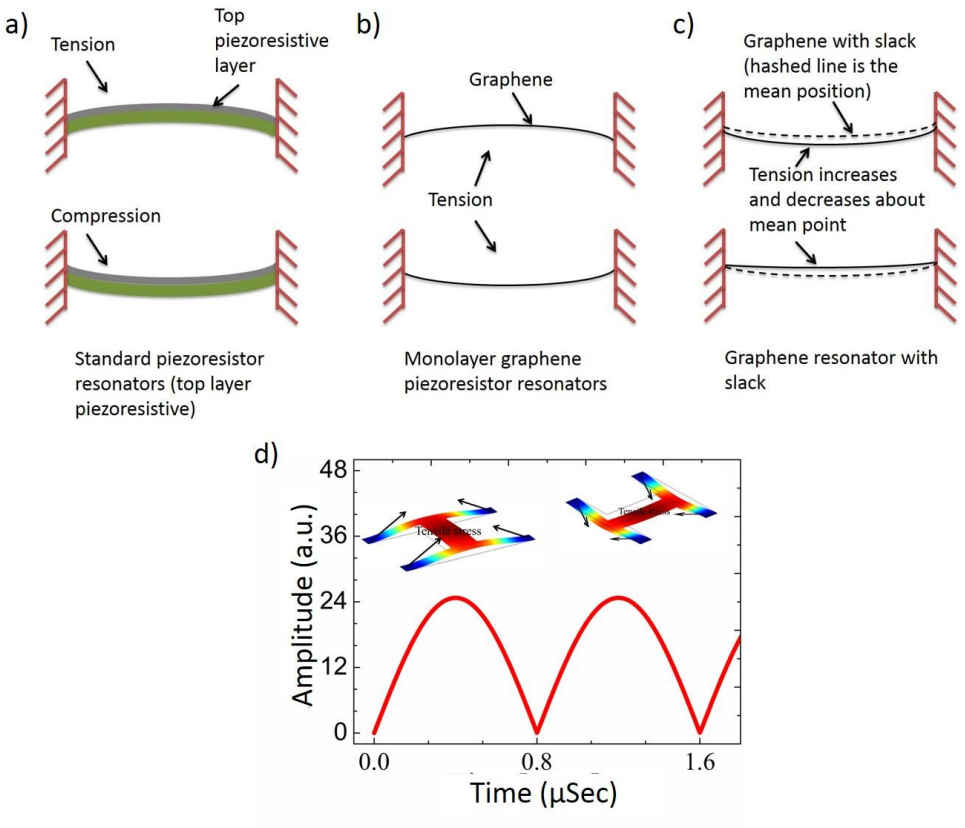

Figure 3. 8a) Schematic of conventional piezoresistive sensors, with a thin piezoresistive layer on a mechanical beam. b) Schematic showing that the graphene resonator is always under tension when perturbed from its equilibrium position. c) Schematic showing a graphene resonator with slack; thus graphene does not change from tensile stress to compressive stress when it bends. d) Graph showing a typical rectified response with inset showing that the graphene always remain under tensile stress in both the cycles.

Figure 3. 8b. Therefore, I expected a rectified output at the amplifier as a consequence of my measurement technique employing intrinsic piezoresistivity; conventional graphene NEMS measurement techniques that use a capacitively gated measurement will not be expected to display rectification. However, I did not see any evidence of the signal being rectified. Essentially, rectification would result in a doubling of the crests (or troughs) of the

output signal, which is not observed as shown in Figure 3. 9. Figure 3. 9 shows the comparison of the time domain output signal from the device (V_{Ext} = 6V, and V_{Inp} = 20mV) at the mechanical resonance frequency (f_o) and the generated signal from a function generator. The function generator signal does not mimic the expected output at the device resonance frequency. The primary reason for this is the expected slack [96] in the resonator as also indicated by the softening non-linearity shown in Figure 3. 3a and b. Such a slack would ensure that the stress resonator varies between a higher tensile points to a lower tensile point without going through a zero-stress level (schematic in Figure 3. 8c). Hence, the lack of expected rectification further evidences the potential slack in the resonator.

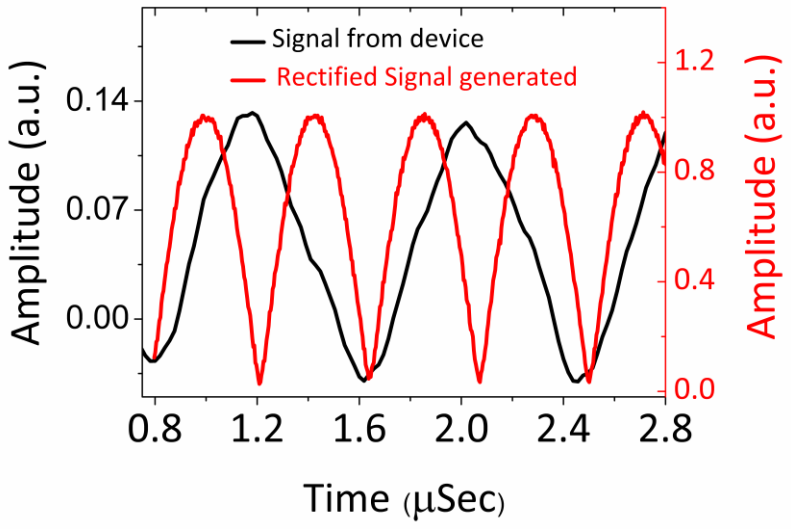

Figure 3. 9 Time domain output signal from device 1 (black curve) at $V_{Ext.}$ (f_o) = 6V, and V_{Inp} 20m. Generated rectified signal using an arbitrary function generator showing doubling of frequency (red curve), confirming that there is no rectification

3.3.2 Piezoresistive transduction of thermomechanical motion

I then proceeded to resolve the thermomechanical motion [58, 93] of the resonator. Thermomechanical noise of a mechanical resonator is present at all temperatures above 0 K. I measured the thermomechanical noise spectrum by averaging the spectrum 32-64 times to obtain high-resolution data. Figure 3. 10 shows schematic of electrical circuit diagram for the thermally driven resonator, where I simply do not drive the piezomechanical disc. Figure 3. 11a shows the amplitude due to thermomechanical motion at V_{Inp} = 120 mV (the red solid line in the figure is the Lorentzian fit to the data). As external drive amplitude (V_{Ext}) is applied and further increased, the resonator can be driven, similar to that seen in the other devices, confirming that this is indeed a highly sensitive transduction method capable of sensing the Brownian motion of the resonator. Figure 3. 11b shows amplitude variation of f_o at constant V_{Inp} with different V_{Ext} including the thermomechanical

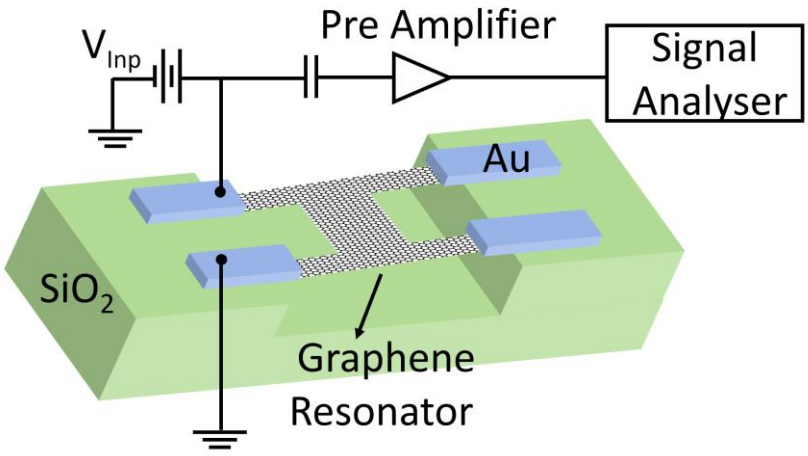

Figure 3. 10 Schematic of the circuit used for sensing the thermomechanical motion of the resonator.

noise data (V_{Ext} = 0V, black data points). A decrease in f_o (softening non-linearity) can be seen as the external drive amplitude is increased. It is worth noting that I observe this softening effect in all my devices.

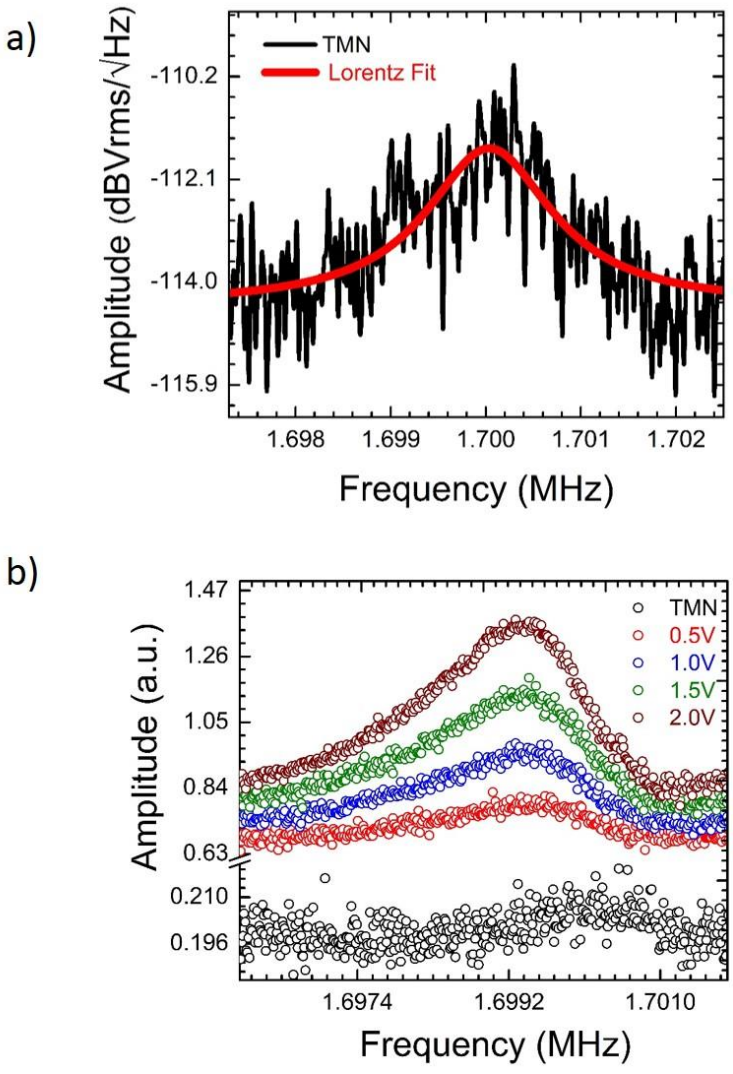

Figure 3. 11 a) Amplitude of thermomechanical motion of device 3 at the resonance frequency (1.7MHz) at V_{Inp} = 120mV; Quality factor (Q) = 1043. b) The resonance frequency response of device 3 with different V_{Ext} and constant V_{Inp} = 120mV.

3.4 Tuning of resonance frequency: Capacitive softening

For piezoresistive detection to induce motion of the resonator, the whole chip containing the resonator is placed on a vibrating piezo disc. High voltage (V_{Ext}) applied to drive the piezo, produces to a small capacitive leakage current which may affect the detection signal. Figure 3. 3a shows variation of amplitude at f_o with different external drive amplitudes (V_{Ext}) at constant bias voltage (V_{Inp}) to the device (Device 1). A decrease in resonance frequency can be observed as V_{Ext} is increased. This is due to capacitive softening of the spring constant which has been observed previously [26, 62, 65, 94-96]. Basically electrostatic interaction softens the intrinsic spring constant K_i. Hence this voltage-induced effective spring [62] constant is given by:

$$K_{eff} = K_i - \frac{1}{2}\left(V_g^{DC}\right)^2 \frac{d^2 C_g}{dZ^2} \tag{3.8}$$

Since in the present device scheme there is no local gate for the resonator, hence due to high parasitic capacitance of the device mechanical resonance frequency (f_o) of the resonator can not be resolved capacitively [98]. Thus in the present work, motion of the resonator is measured due to mechanical actuation only but not due to capacitive coupling (electrostatic actuation). Since there is no impedance matching, as a result capacitive coupling is not perfect and not enough to drive the resonator. But the drive voltage (V_{Ext}) applied to the piezo-mechanical disk effects the K_{eff} of the device as shown in equation 3.8 and the background signal. Graphene is known for frequency tuning with capacitive

charging, generally done through gate voltage. Hence in the present detection technique as V_{Ext} increases, capacitive charging also increases, although this is very small compared to the gate voltage applied to the device. This results in the change (decrease) in the resonance frequency as shown in Figure 3. 3 a. Capacitive softening could be due to slack in the beam (CVD graphene) as this softening has been explained due to slack in the beam earlier [96]. This is not unexpected – the graphene I used was grown using CVD and transferred to a silicon dioxide substrate in liquid, which would significantly change intrinsic

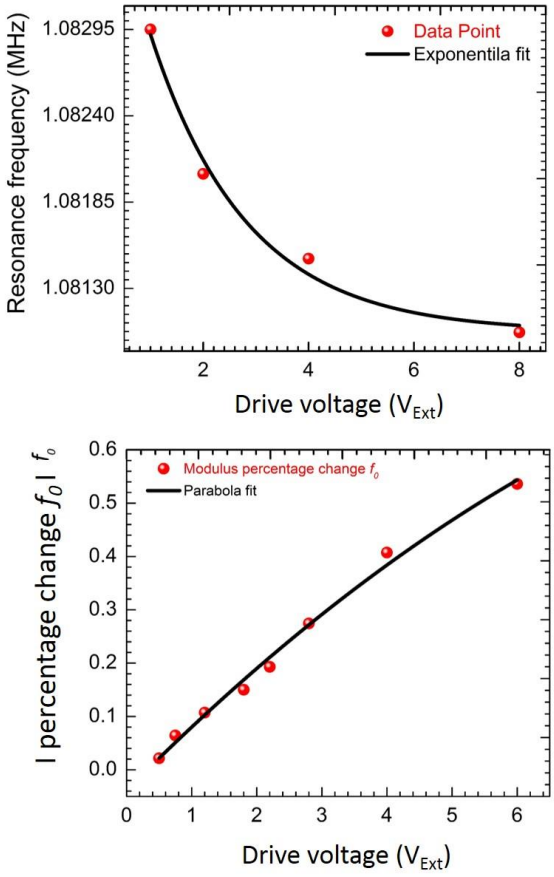

Figure 3. 12 a) Change in resonance frequency of device 2 with V_{Ext} (red data point). Black curve fits the data point showing exponential decrease in the f_0. b) Tuning of f_0 up to 0.6% with V_{Ext}.

stress effects as compared to mechanically exfoliated graphene. For one of the devices frequency tuning of f_o with V_{Ext} is shown in Figure 3. 12. Figure 3. 12a shows parabolic negative tuning of f_o with V_{Ext} as shown in previous literature [62, 65, 95]. Figure 3. 12b shows approximately -0.6% tuning of f_o with V_{Ext}. Tuning of f_o with V_{Ext} confirms that what I measured is resonance frequency of graphene, because V_{Ext} would not alter the f_o of the gold (Au) electrodes.

3.5 Current annealing of devices

Resist residues are mostly left over on the surface of graphene due to the fabrication process which is unavoidable and very difficult to remove completely [99]. I performed Joule heating [43, 61-62,100] prior to electrical measurements to remove impurities and other adsorbents on the device from the fabrication process. Due to removal of residual impurities from surface of graphene, resistance and mass of the graphene reduces and become closer to the single layer of graphene. Doping concentration can also decrease due to removal of impurities. Hence overall the electronic and mechanical properties of graphene improve. In this process I heated graphene locally by passing a large current density through the device. Due to Joule heating the local temperature of graphene increases enormously which results in evaporating residual impurities such as water molecules, N_2, resist-based impurities and other inert and non-reactive impurities which cling to surface of graphene. I performed current annealing in vacuum so that there shouldn't be any reactions from other molecules which will affect graphene. This was done

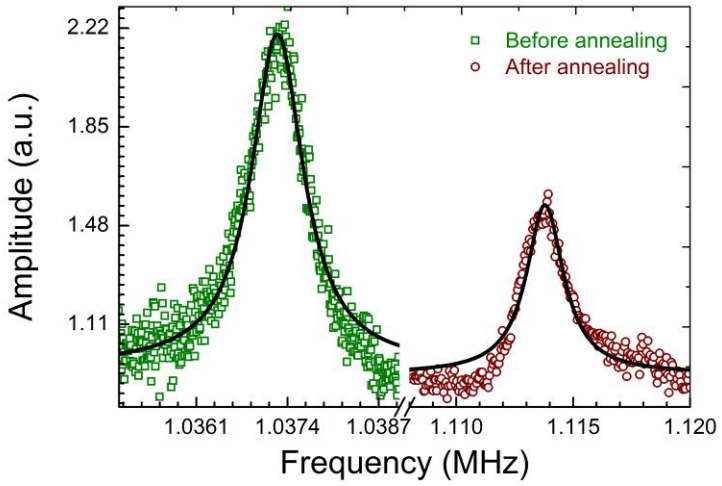

Figure 3. 13 Change in f_o of a device 2 during initial (green data points) and final (red data points) current annealing measurements. The black lines are Lorentzian fits to the data.

simply by slowly increasing V_{Inp} in steps of 10-20 mV and observing the resistance of the device for few minutes. If there was no considerable change in device resistance I increased V_{Inp} further to the next step. In case I observed any change in device resistance I wait for a few minutes until it stabilizes. I repeated the same process by changing the polarity of electrode. Thus I tried to get rid of as much contamination as possible. Extra care was taken so that the device was annealed without damage. As V_{Inp} was slowly increased in steps of 10-20mV thus the process was in control such that annealing is done without burning off the graphene layer. If V_{Inp} is increased at a faster rate then there is a risk of burning off the graphene layer before or during the point when the contaminants were driven off the membrane. Apart from change in the device resistance I also observed a shift in position of the resonance frequency due to change in mass of the graphene as I decreased the impurity level of graphene during current annealing. Generally I observed an increase in resonance

frequency as I performed current annealing as shown in Figure 3. 13. Resistance of the device was observed to decrease from 6 kΩ to 0.8 kΩ during current annealing. Figure 3. 13 shows an increase of 7.4 % in f_o as the resistance of the device decreases during measurement (after initial current annealing).

3.6 Calculations

3.6.1 Calculation of Dynamic range [25-26]

The linear dynamic range (DR) of nanomechanical resonators is the largest signal to noise ratio. It is measured from the thermomechanical noise to the onset of nonlinearity.

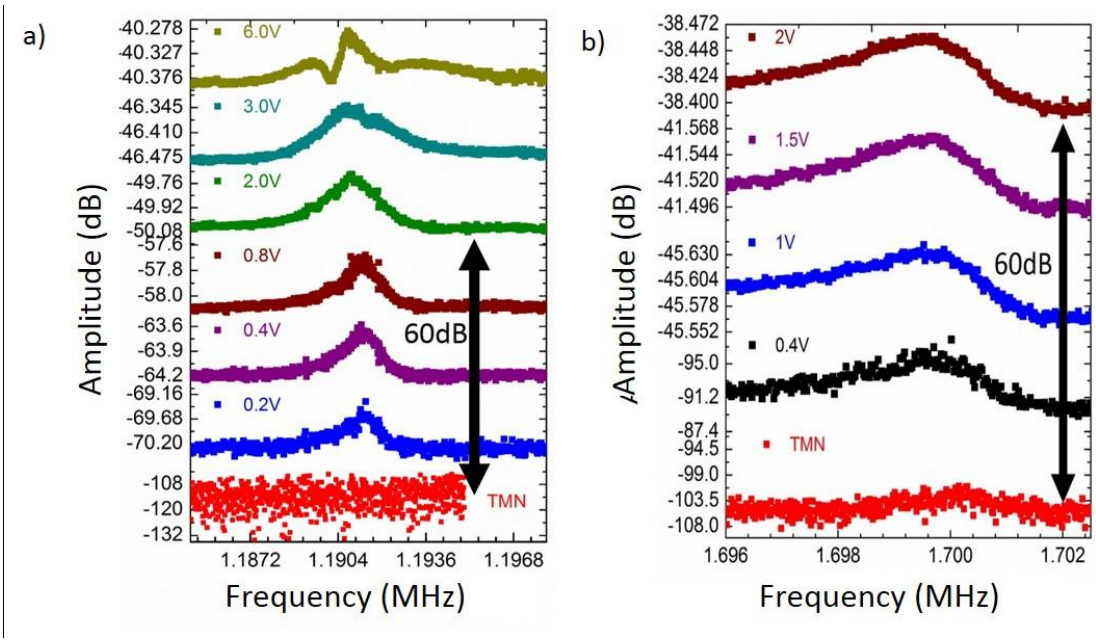

Figure 3. 14 Estimation the dynamic range of device 1 (a) and device 3 (b). Both the devices shows linear dynamic range of more than 60 dB from thermomechanical noise to onset of nonlinearity – I used 60 dB to estimate the mass sensitivity.

Figure 3. 14a shows the resonance frequency of a device with varying actuation. Although I was not able to resolve the thermomechanical frequency peak, the thermal noise floor is shown as red curve. The other curves in different colours are the piezomechanically driven responses. At V_{Ext} = 2V broadening of the resonance peak and a slight shift in lower value could be observed (Duffing behaviour, discussed in chapter 4). Above V_{Ext} = 2V a further broadening and tilting towards the lower value frequency could be observed. At V_{Ext} = 6V nonlinearity in the frequency curve could be clearly observed. Hence I assumed that the highest drive (2V), at which non-linearity was not observed, is the dynamic range of the device [25-26], which is a conservative assumption. Figure 3. 14b shows the resonance frequency of another device with varying actuation. The red curve shows the thermomechanical noise spectrum at resonance frequency, while the other curves in different colours are the piezomechanically driven responses. The data shows that the linear dynamic range (DR) [25-26] of this resonator is more than 60dB as measured from thermomechanical noise floor to the onset of nonlinearity.

3.6.2 Calculation of mass and force sensitivity

For more realistic situations, considering the mass of the resonator to be higher than that of monolayer graphene due to residues (contamination) remaining after fabrication [61]. I have assumed $\rho_{eff} = 2.5x\rho_{graphene}$, where $\rho_{graphene} = 7.4 \times 10^{-16}$ g/ μm^2 [61] to calculate effective mass of the resonator (M_{eff}). Thus considering dimensions of the devices, and $\rho_{eff} = 2.5x\rho_{graphene}$, $M_{eff} = 1.665 \times 10^{-15}$ gm is calculated.

Minimum resolvable mass **(**δm**)** is given by:

$$\delta m = 2M_{eff} \left(\frac{\Delta f}{Q\omega^0}\right)^{1/2} 10^{-DR/20} \quad (3.9)$$

$$\delta m \sim (M_{eff}/Q) \times 10^{-DR/20} \quad (3.10)$$

For driven response:

Device 1, δm ~ (1.41 ± 0.02) x 10^{-21} g for Q ~ = (1180 ± 20).

Thermal motion of a resonator is given by $x_{th} = \sqrt{\frac{K_b\ T}{k}}$ (3.11)

Hence for a graphene monolayer resonator (0.34nm thick), with $f_0 = 1.7$ MHz (device 3), and very low k_{eff} 0.2 x 10^{-3} N/m has a room temperature thermal motion of $x_{th} = 4.55$ nm. The thermomechanical noise arises from a noise force exerted on the device by the surrounding temperature, and its force spectral density is given by [31]

$$(S_{th}^F)_{Min} = \frac{4kTK_b}{\omega_0 Q} \quad (3.12)$$

Where *k* is the spring constant (which increases with increasing mass, as k= M_{eff} ω^2) *T* the temperature (300 K in this case)and k_b is the Boltzmann constant.

For Device 1, Q = (1180 ± 20), minimum force resolution is given by:

$$F_{min} = \sqrt{S_{th}^F} = (13.7 \pm 0.1)\ aN/\sqrt{Hz}$$

3.7 Conclusions:

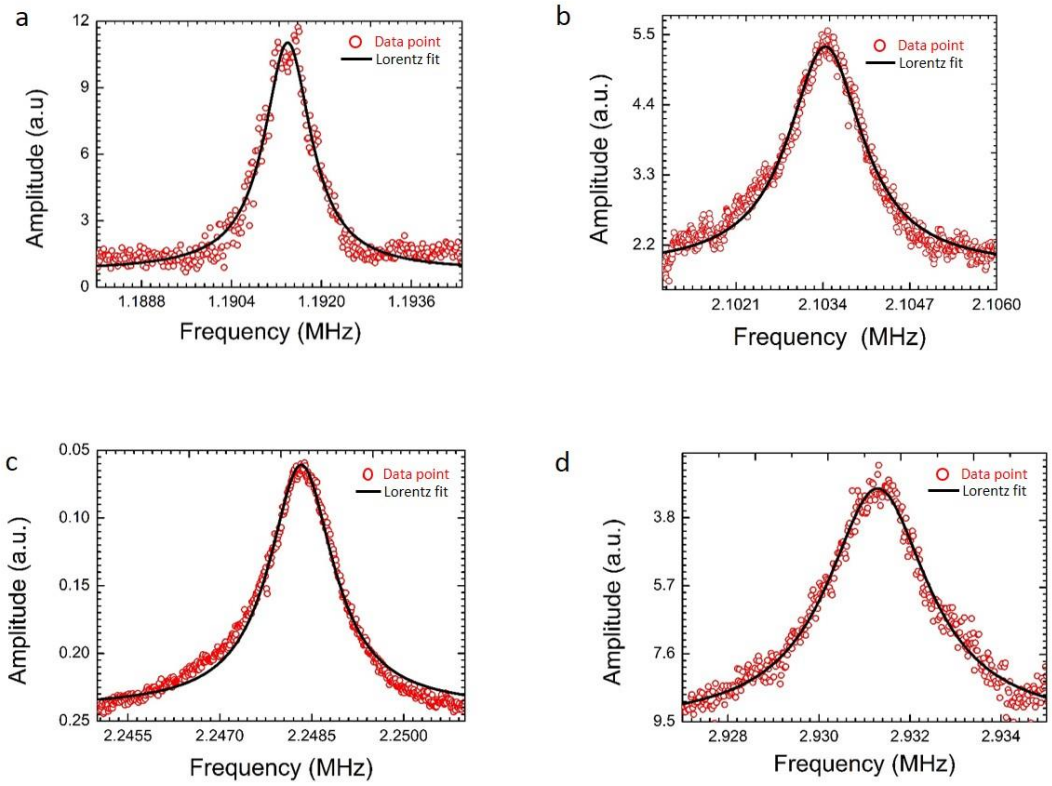

Figure 3. 15 a-d) The resonance frequency response of different devices. Circular red rings are data points and the black line is the Lorentz fit of the data points.

In conclusion, I demonstrate that the intrinsic piezoresistivity of graphene is an effective technique to transduce the motion of monolayer graphene nanomechanical resonators. I find that such graphene resonators show high Q-factors of >103 [4], the highest reported value for beam resonators at room temperature [4]. I have shown thermomechanical motion in ambient temperatures and pressures of ~ 4 × 10-6 T. Figure 3. 15 shows frequency response of a few devices. I have measured f_0 mostly between 1-3 MHz with Q of the order of 10^3 (1-2). In Figure 3. 16, I list the measured resonance 3 MHz

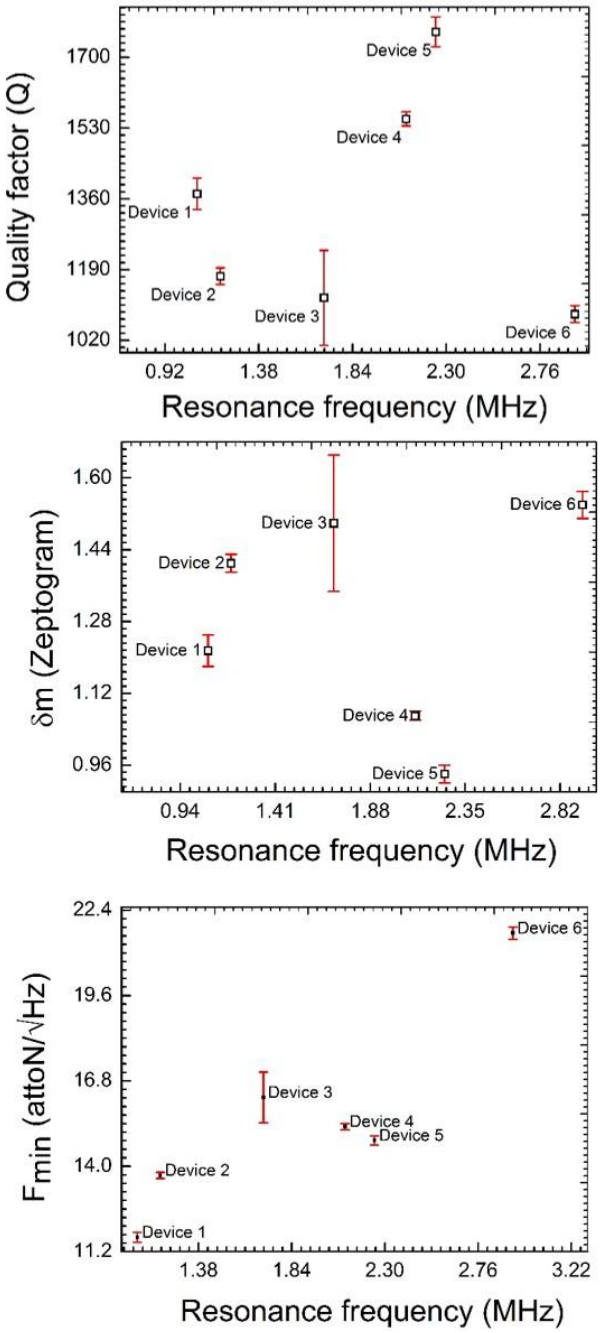

Figure 3. 4 Performance of different devices. Comparison of a) quality factor b) minimum resolvable mass and c) minimum force detection of six different devices.

with Q of the order of 10^3 (1-2). In Figure 3. 15, we list the measured f 3 frequencies and

the calculated quality factor, force and mass sensitivities for six devices, showing that the process is highly repeatable. The minimum detectable mass and force resolution of such resonators is calculated to be an astounding 0.95 – 1.54 zeptograms (10^{-21} g) and 11.7 – 21.6 aN/$Hz^{1/2}$ at *room temperature* as shown in Figure 3.16. In chapter 4 I will discuss about qualitative and quantitative analysis of various nonlinearity present in graphene-NEMS.

Chapter 4

Nonlinearity in Graphene-NEMS

In NEMS, a linear excitation can result in a non-linear response from the device. We have observed that this is particularly prominent for two-dimensional materials such as graphene. Graphene with its outstanding properties, such as high stiffness and low mass density, is an exceptional candidate for nanoelectromechanical systems (NEMS). However, due to its small dimensions, its frequency response is quite nonlinear [21,101]. Studying this will allow us to address the basic understanding of this phenomena and its origin. Understanding the onset of nonlinearity in such devices is particularly important. This nonlinearity provides a new opportunity for applications such as mass sensing in NEMS devices, while also serving as a cautionary design constraint.

4.1 Harmonic Oscillator [102]

A very common example of a simple harmonic oscillator (SHO) is a mass *M*, attached to a spring with spring constant *k*, fixed at one of the ends. With a small displacement *x* from equilibrium position, the restoring force *F* (which acts in opposite direction of the displacement) can be expressed as:

$$F = -kx \tag{4.1}$$

But $F = Ma$, where a is acceleration, hence

$$M\left(\frac{d^2x}{dt^2}\right) = -kx \tag{4.2}$$

$$\left(\frac{d^2x}{dt^2}\right) = -\left(\frac{k}{M}\right)x \tag{4.3}$$

Comparing with the standard equation of a SHO: $\left(\frac{d^2x}{dt^2}\right) = -\omega_o^2 x$

Where ω_o is angular resonance frequency of SHO, we get: $\omega_o^2 = k/M$ (4.3a)

Using: ($\omega_o = 2\pi f_o$)

$$f_0 = \frac{1}{2\pi}\sqrt{\frac{k}{M}} \tag{4.4}$$

Where f_o is the mechanical resonance frequency of the oscillator. In reality there is no perfect harmonic oscillator and hence damping [102] has to be taken in account in the oscillator. Damping has a very important impact on the frequency response of the oscillator and hence influences the performance. Vibrational energy dissipates into the surroundings, which damps the amplitude. Let us consider a linear damping coefficient γ, and hence additional linear damping force $\gamma\ (dx/dt)$ will be added to equation 4.2 due to the linear damping [102] in the system. For a resonator it needs to be driven externally, thus a periodic driving force with amplitude F and frequency ω given by $Fsin(\omega t)$ is included. Hence eq. 4.2 is modified by two additional terms $\gamma(dx/dt)$ and $Fsin(\omega t)$.

$$M\left(\frac{d^2x}{dt^2}\right) + \gamma\left(\frac{dx}{dt}\right) + kx = Fsin(\omega t) \tag{4.5}$$

Let us consider the steady state solution of equation 4.5 to be of the form:

$$x = A \sin(\omega t - \varphi) \tag{4.6}$$

Therefore amplitude A, phase φ, and quality factor Q can be written as:

$$A = \frac{F}{k} \frac{Q}{\sqrt{Q^2\left(1-\frac{\omega^2}{\omega_0{}^2}\right)+\left(\frac{\omega^2}{\omega_0{}^2}\right)}} \tag{4.7}$$

$$\varphi = \tan^{-1} \frac{\omega\omega_0}{Q(\omega_0{}^2-\omega^2)} \tag{4.8}$$

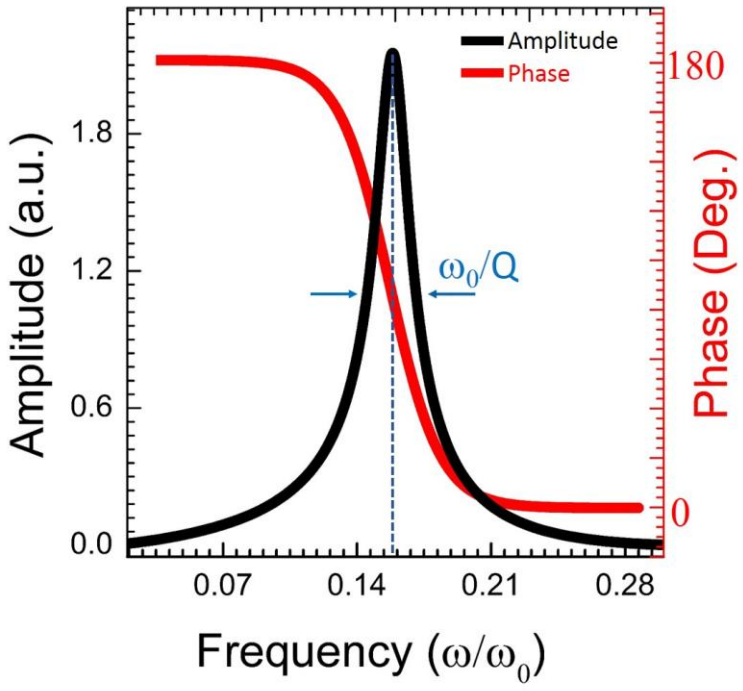

Figure 4. 1 The amplitude and phase of a driven damped harmonic oscillator.

$$Q = \frac{\omega_0}{\gamma} \tag{4.9}$$

At resonance $\omega = \omega_o$, and therefore, from equation 4.7 and 4.8:

$$A = \frac{QF}{k}\ ,\ \ \phi = \pi/2 \tag{4.10}$$

$$\text{and}\ \ Q = \frac{f_0}{\Delta f} \tag{4.11}$$

where Δf is full width at half maximum(FWHM) of the amplitude resonance peak shown as $2\pi f_o/Q$ in the Figure 4. 1. Figure 4. 2 shows frequency response of a resonator with different γ. Resonace peak become broder and quality factor decrese as we increse the γ. In the

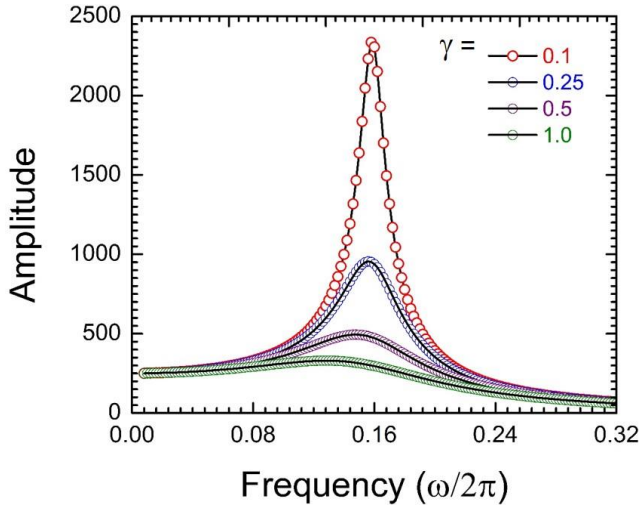

Figure 4. 2 The frequency response of a driven damped harmonic with variation γ

absences of γ, the amplitude of resonance peak would resemble a Dirac delta function with infinite amplitude, zero Δf (FWHM) and hence infinite *Q*. Therefore, it would keep oscillating forever even after removal of the applied force.

Figure 4. 3b shows the nonlinear frequency response as we anneal [41, 61, 62, 83] the sample (device 2) and remove the impurities and residues. We can clearly observe in Figure 4. 3a that before the impurities are removed, an increase in the external drive voltage (V_{Ext}),

the resonance frequency doesn't change significantly. As we start annealing the device, residual impurities are removed and hence the mass of the resonator decreases which results in the increase in resonance frequency as shown in Figure 4. 3b. Furthermore, unlike

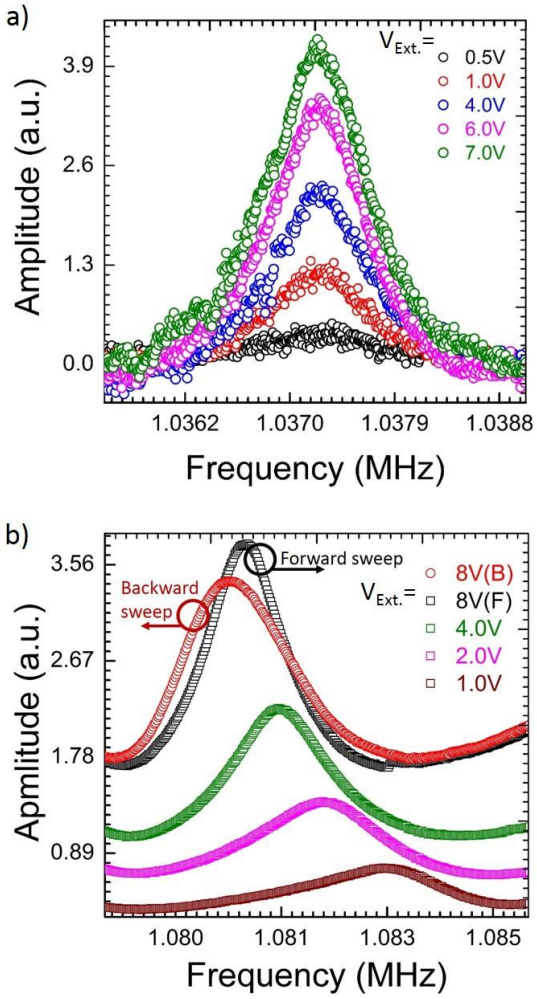

Figure 4. 3 a) The linear resonance frequency response with different V_{Ext} prior to annealing the device. b) The non-linear resonance frequency response after annealing the device. Hysteresis in the resonance frequency is also observed while sweeping frequency in a forward (black square data point) and backward direction (red circular data point)

pre-annealing there is a change in the resonance frequency as we increase the external drive voltage (V_{Ext}) post-annealing. Resonance frequency decreases (Capacitive softening) [26, 62, 65, 78-79] with an increase in V_{Ext} as shown in Figure 4. 3b. Hysteresis in the resonance frequency is also observed in these devices after removing impurities whilst sweeping frequency in a forward and backward direction as Figure 4. 3b. Subsequently as we decrease the mass of these nanomechanical resonators, non-linearity, decrease in material damping, and hysteresis in the resonance frequency are observed in most of the devices whilst driving at a higher amplitude. It has been shown earlier that in nanomechanical resonators, hysteresis can be used an ultra-sensitive charge detection application [101].

4.2 Nonlinear frequency response of nanomechanical resonators [21,101-2]

The model represented by equation 4.5 considering linear damping γ in the oscillator, accurately describes its damped oscillation for resonators with dimensions from meter scale to a few tens of micrometers. However, for atomic scale resonators such as monolayer graphene where transverse dimension is sub nanometer, this simple linear damping model fails and the damping behavior cannot be described by the above model. For example, changes in resonance frequency due to the driving force, hysteresis in the resonance peak while sweeping, and asymmetry in the resonance peak has been observed in these resonators nanoscale resonators which cannot be explained by the above model.

4.2.1 Duffing resonator [101-2]

The Duffing equation was introduced in 1918 to describe the motion of a nonlinear resonator with a cubic stiffness term along with the linear stiffness as shown in Figure 4. 4. It can be either positive for hardening spring effect or negative for softening spring effect which is observed in many mechanical systems such as resonators. In the previous section we have discussed ideal linear systems where the spring constant behaves linearly as the resonator moves. But in a real systems many nonlinearities exist. Figure 4. 4 shows a mass *M* with displacement degree of freedom *x*. In addition to a linear spring of stiffness k, the mass is also connected to a nonlinear spring with spring stiffness α and a damper with damping coefficient *c*. $F_{Ext.}$ is the external driving force applied to the system. A quadratic nonlinear spring stiffness αx^2 is produced due to nonlinear spring and hence the total restoring force of the spring due to linear and nonlinear spring is given by:

$$f_{res} = (k + \alpha x^2)x = kx + \alpha x^3 \tag{4.12}$$

As we increase the driving force of resonator, the amplitude of motion becomes quite large relative to the thickness of the resonator. At large amplitudes, the potential of the resonator becomes non-harmonic (non-parabolic), as shown in Figure 4. 5b, due to a contribution of higher order terms of displacement. Hence a non-restoring force comes into play at large amplitude. Due to the non-linear restoring force, the motion of resonator becomes non-linear like a Duffing resonator [101-2]. A Duffing resonator is an example of a periodically forced resonator with a nonlinear elasticity (α). The motion of a resonator wi-

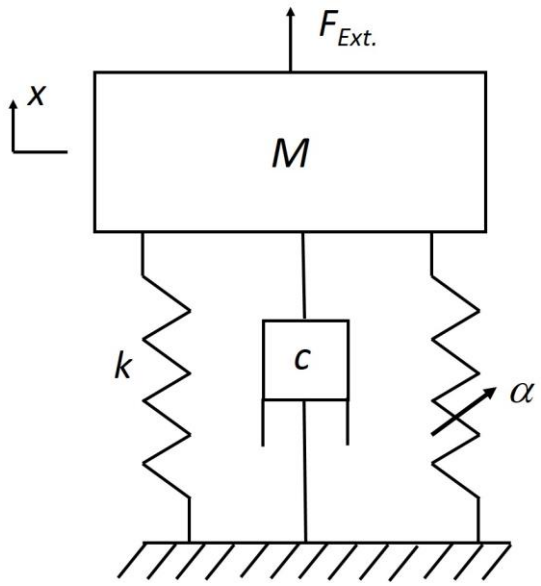

Figure 4. 4 A resonator with linear as well as nonlinear spring constants.

th nonlinear spring constant has a more complicated potential than simple harmonic motion such as a spring pendulum, as its spring stiffness does not follow Hooke's law (equation 4.1). This is a type of perturbed simple harmonic resonator and its motion can be explained by modifying the previous model and adding a Duffing term αx^3 in the equation of motion (equation 4.5), where α is the Duffing damping coefficient which gives an estimate of this kind of nonlinear stiffness. This Duffing term (αx^3, cubic nonlinearity) arises from anharmonicity in the external potential as explained earlier. Hence the motion of a classical particle in anharmonic potential such as a double well potential (Figure 4. 5b) is described by the Duffing equation Let us consider a simple model for such a potential as:

$$V(x) = \alpha \frac{x^4}{4} + k \frac{x^2}{2} \tag{4.13}$$

The Force acting on the beam is given by the gradient of V(x) plus external drive,

$$M\left(\frac{d^2x}{dt^2}\right) = \text{- grad V(x)} + Fsin(\omega t) \quad (4.14)$$

$$M\left(\frac{d^2x}{dt^2}\right) = \text{- kx - } \alpha x^3 + Fsin(\omega t) \quad (4.15)$$

Dissipation of motion due to damping caused by friction, viscosity due to surrounding air or any other fluid, and other forces can be modelled using a linear velocity dependent term given as $F_{Damp} = k\,(dx/dt)$, considering only linear damping γ. Hence the equation of motion is given by:

$$M\left(\frac{d^2x}{dt^2}\right) + \gamma\left(\frac{dx}{dt}\right) + kx + \alpha x^3 = Fsin(\omega t) \quad (4.16)$$

Depending on the nature of α, the Duffing nonlinearity can be positive ($\alpha > 0$), thus favoring the restoring force, making the resonator stiffer, and thus increasing the resonance frequency until it reaches a saddle-node bifurcation point as shown in Figure 4. 6a . It can also be negative ($\alpha < 0$), thus acting against the restoring force making the resonator less stiff and decreasing its resonance frequency. Unlike a linear oscillator where the resonance frequency is independent of amplitude given as $x(t) = Asin\,(\omega t-\varphi)$, in the case of a Duffing resonator the amplitude of the resonance frequency is a function of frequency. Thus the solution of steady state has to be modified and can be written as $x(t) = A(\omega)sin\,(\omega t-\varphi)$. The Duffing resonator model explains remarkably hysteresis and frequency dependent amplitude shift [101-102].

a)

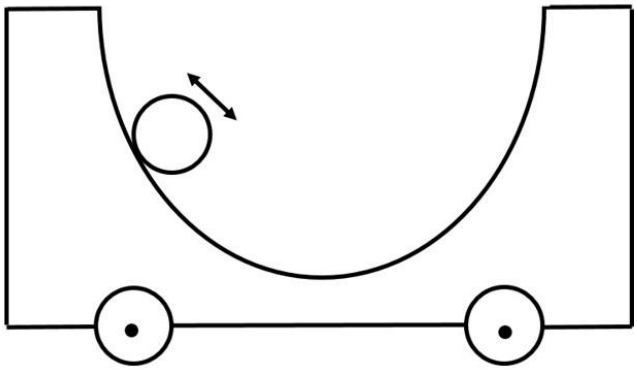

b)

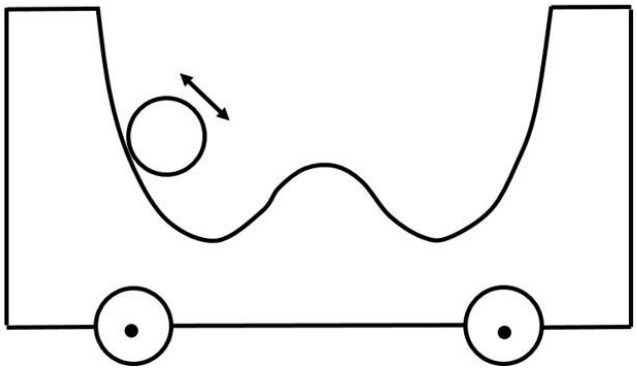

Figure 4. 5 A vehicle with a ball rolling inside on a cross section with one minima (a) or with two minima (b).

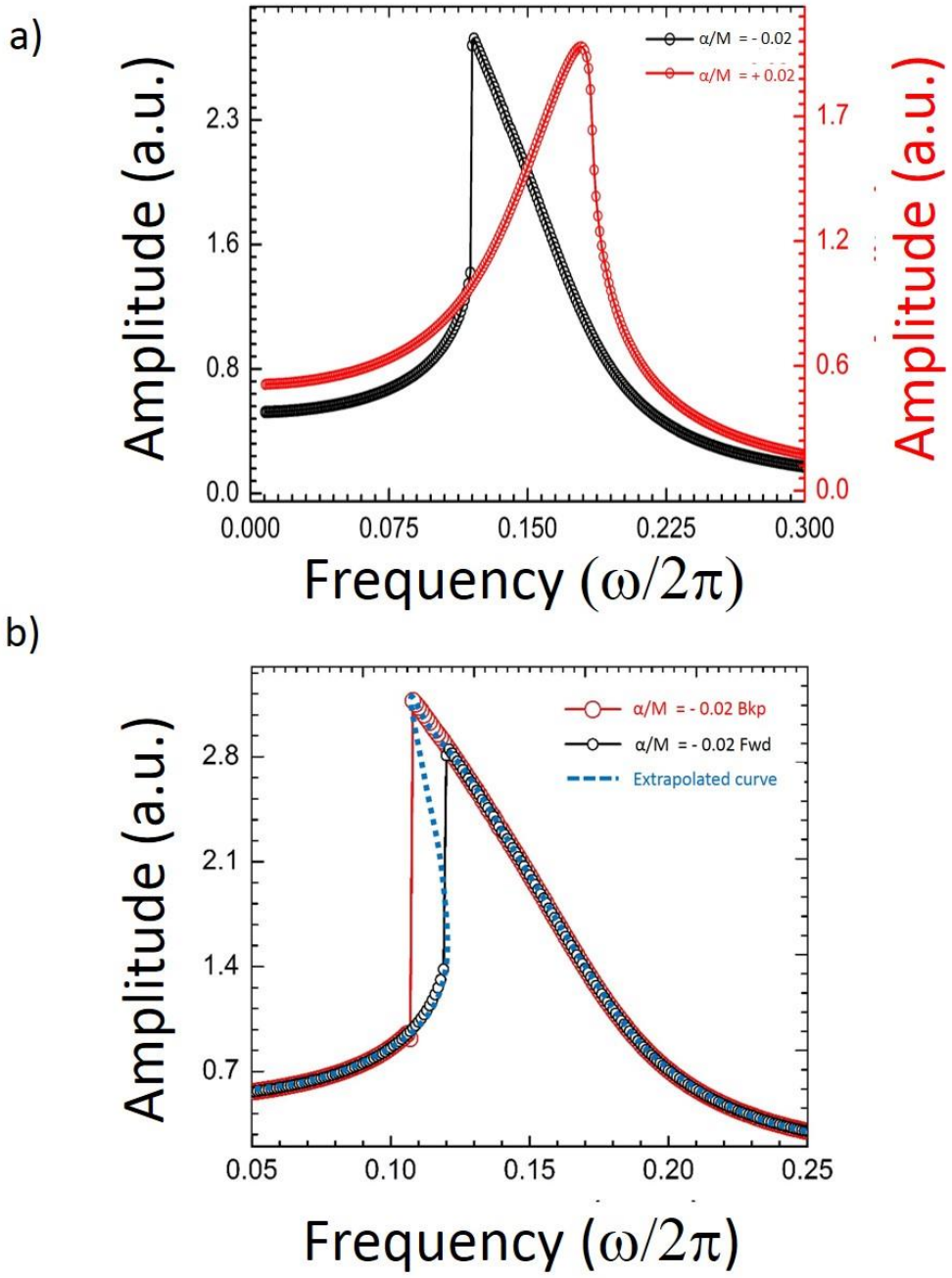

Figure 4. 6 Simulation data of the resonance frequency response of a Duffing resonator with α = - 0.02 (black curve) and α = + 0.02 (red curve). b) Hysteresis in the resonance frequency response of a duffing resonator at α = - 0.02 whilst sweeping frequency in a forward and backward direction. Extrapolated curve shows unstable branch (blue curve).

I have solved Equation 4.16 using MATLAB® for different values of the parameters γ, *k*, α, *F* to understand the frequency response of a Duffing resonator. Figure 4. 6a shows simulation data for both a positive and negative nonlinear spring constant (α), showing the frequency response of a softening as well as hardening spring effect in a Duffing resonator. As we sweep the frequency in a forward direction going from a lower to a higher value, the amplitude rises at higher frequencies. While sweeping frequency in a backward direction driving resonator from a higher value of frequency to a lower value, the amplitude rises at lower frequencies showing hysteresis in the amplitude as a function of sweep frequency. The amount of non-linearity in the system decides the amount of hysteresis. Hence the higher the non-linearity in the system, the larger the hysteresis in amplitude would be. Figure 4. 6b shows simulation data of the frequency response of a Duffing system for α = -0.02 and γ = +0.1. Hysteresis is observed whilst going from a lower to a higher value of frequency and vice versa. The extrapolated curve shows an unstable region at the saddle-node bifurcation point. The equation of motion of the Duffing resonator (Equation 4.16) is solved for different values of α at constant values of other parameters to understand the effect of both negative and positive α on the frequency response of the resonator. Figure 4.7a shows the simulation data of the frequency response of a softening spring effect Duffing resonator using Equation 4.16 with γ = +0.1 $\alpha = -0.02$ and for different value of *F*. As we increase *F*, not only the amplitude of the motion increases but also Duffing nonlinearity due

to α also increases. Decrease in the resonance frequency of the resonator indicates that the resonator becomes less stiff due to negative value of α. Figure 4. 7b shows simulation

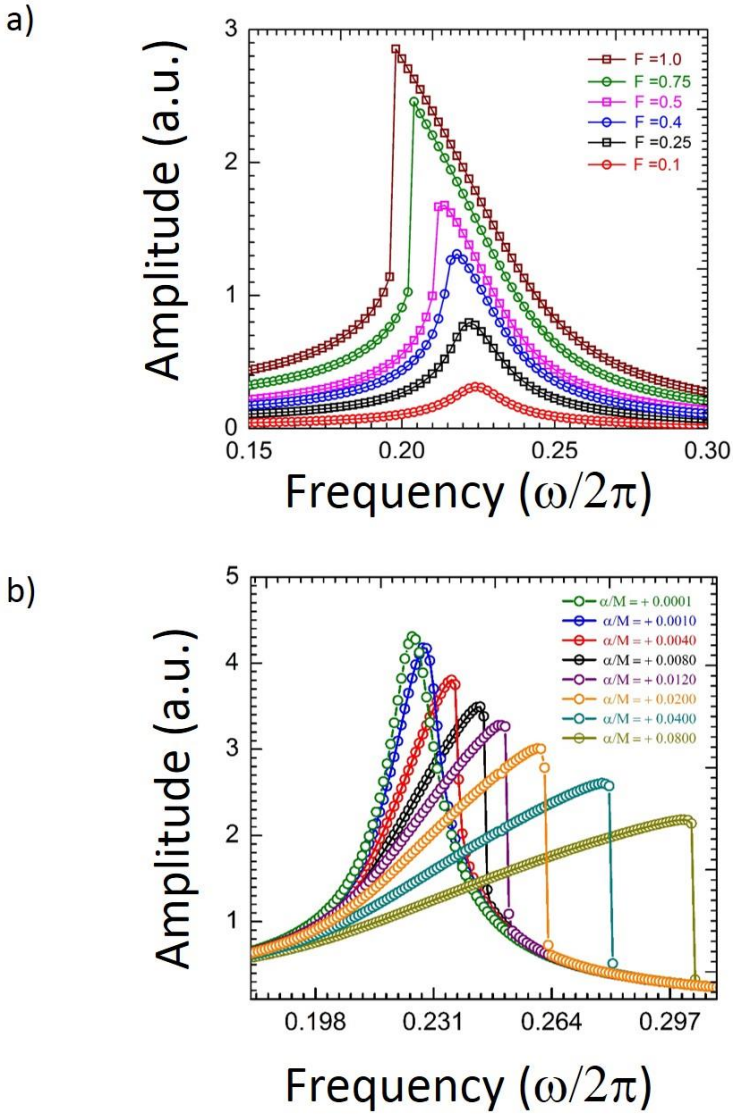

Figure 4. 7 a) Simulation data of the resonance frequency response of a Duffing resonator with softening spring effect (α = - 0.02) for different value of *F*. b) Simulation data of the resonance frequency response of a duffing resonator with hardening spring effect for constant value of *F* = 1 with different value of α.

data of the frequency response of a hardening spring effect of a Duffing resonator using equation 4.16 with γ = +0.0725 and *F* = 1, for different values of α. Similar to a softening spring effect, the amplitude of the oscillation also decreases with an increase in α but the resonance frequency increases which is due to a positive value of α making the resonator stiffer.

Figure 4. 8a shows the frequency response of one of the resonators (device 4). The resonance frequency of the device is shown at $V_{Ext.}$ = 6V and $V_{Inp.}$ = 40mV. At around 1.168MHz, the amplitude undergoes a sudden jump (Saddle-node bifurcation point) as we increase the frequency, indicating that the system is quite unstable at this frequency. $\alpha = -0.02$ and $\gamma = +0.1$ are extracted from the fit to data using equation 4.16 showing this negative nonlinear spring effect. Figure 4. 8b shows hysteresis in the resonance frequency of the Duffing resonator whilst sweeping the frequency in a forward and backward direction. The amount of non-linearity in the system determines the amount of hysteresis. Hence the higher the non-linearity in the system the larger the hysteresis in amplitude would be. We observe hysteresis in a nanomechanical resonator quite often whilst driving the resonator at higher amplitudes. H. Krommer *et al.* [103] have shown that hysteresis can be used to detect a single charge.

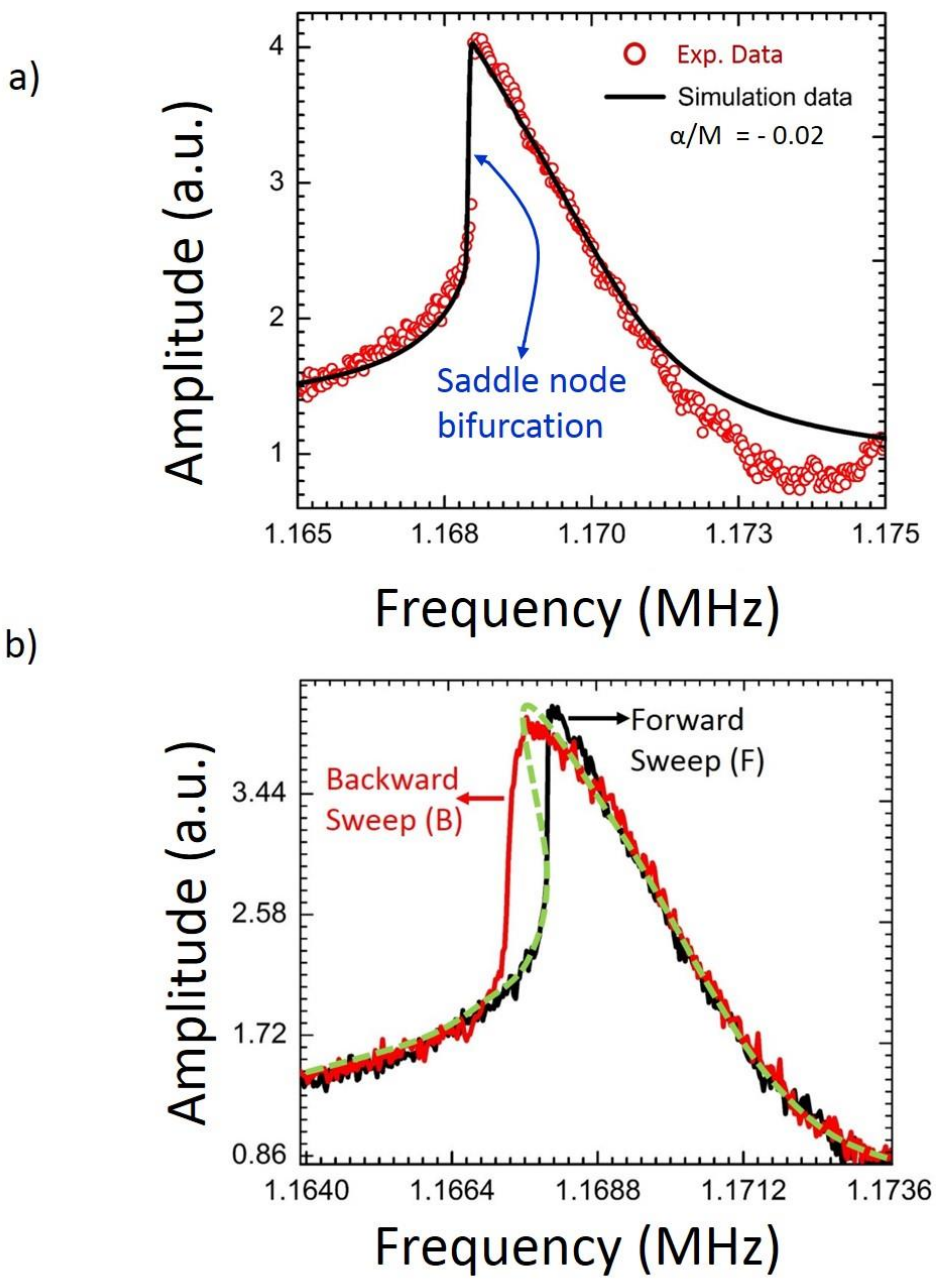

Figure 4. 8 a) The resonance frequency response of device 4 showing Duffing behavior at V_{Ext} = 6V and V_{Inp} = 40mV (red circular data point). Solid black line shows the simulation data using equation 4.16 with α = - 0.02. b) Forward frequency sweep (black and solid line) and backward frequency sweep (red solid line) of resonance frequency response of device 4 (Duffing behavior) at V_{Ext} = 6V and V_{Inp} = 40mV. Extrapolated curve shows unstable branch (green curve).

Figure 4. 9 shows the frequency response of device 4 as we change the amplitude of motion by varying V_{Ext} from 0.1 to 6V, keeping $V_{Inp.}$ = 40mV constant. The behavior is similar to the simulation data of a softening nonlinear spring effect as shown in Figure 4. 7a. The resonance frequency and saddle-node bifurcation point decreases with an increase in $V_{Ext.}$ There is also an increase in the amplitude with V_{Ext}. Thus we can tune α with $V_{Ext.}$ We also observe hysteresis in the fundamental resonance mode whilst sweeping the frequency in a forward and backward direction. Recently [4] it has been reported that for such systems, mode splitting occurs at higher modes. In Figure 4. 10 the first and second mode of device 2 is shown. An amplitude jump in both the modes with increasing frequencies indicates Duffing behavior of the system. Duffing behavior in the second mode further confirms mode splitting in these devices. Figure 4. 10a shows the first and second mode of the Duffing resonator (device 4). Figure 4. 10b shows the variation of amplitude of the second resonance mode at different external drive amplitudes (V_{Ext}) whilst maintaining a constant bias voltage (V_{Inp}). As the resonator is driven with increasing amplitude, Duffing non-linearity (α) starts appearing. Mode 2 also shows negative nonlinearity making the resonator less stiff, and thus decreasing the resonance frequency as the external drive is increased from $V_{Ext.}$ = 0.4 to 6 V. As expected, an increase in non-linearity with the increase in amplitude of vibration ($V_{Ext.}$) is observed. At the higher V_{Ext} hysteresis in the second mode, whilst sweeping the frequency in a forward (black line) and backward direction, is observed like the first mode.

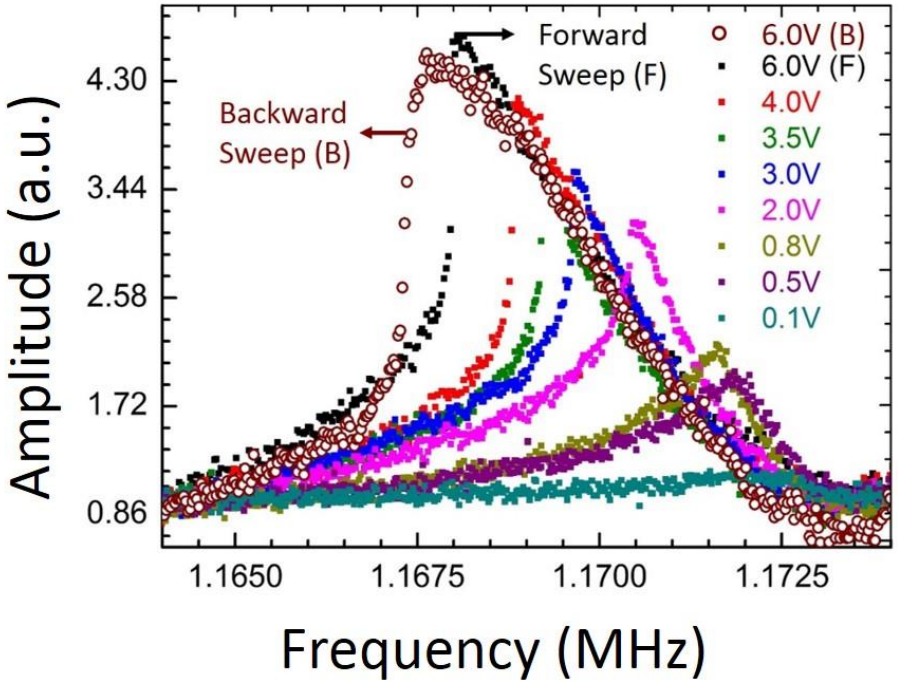

Figure 4. 9 The resonance frequency response of device 4 with different V_{Ext} and constant V_{Inp} = 40mV. Duffing nonlinear behavior due to large vibrational amplitude and hysteresis is observed.

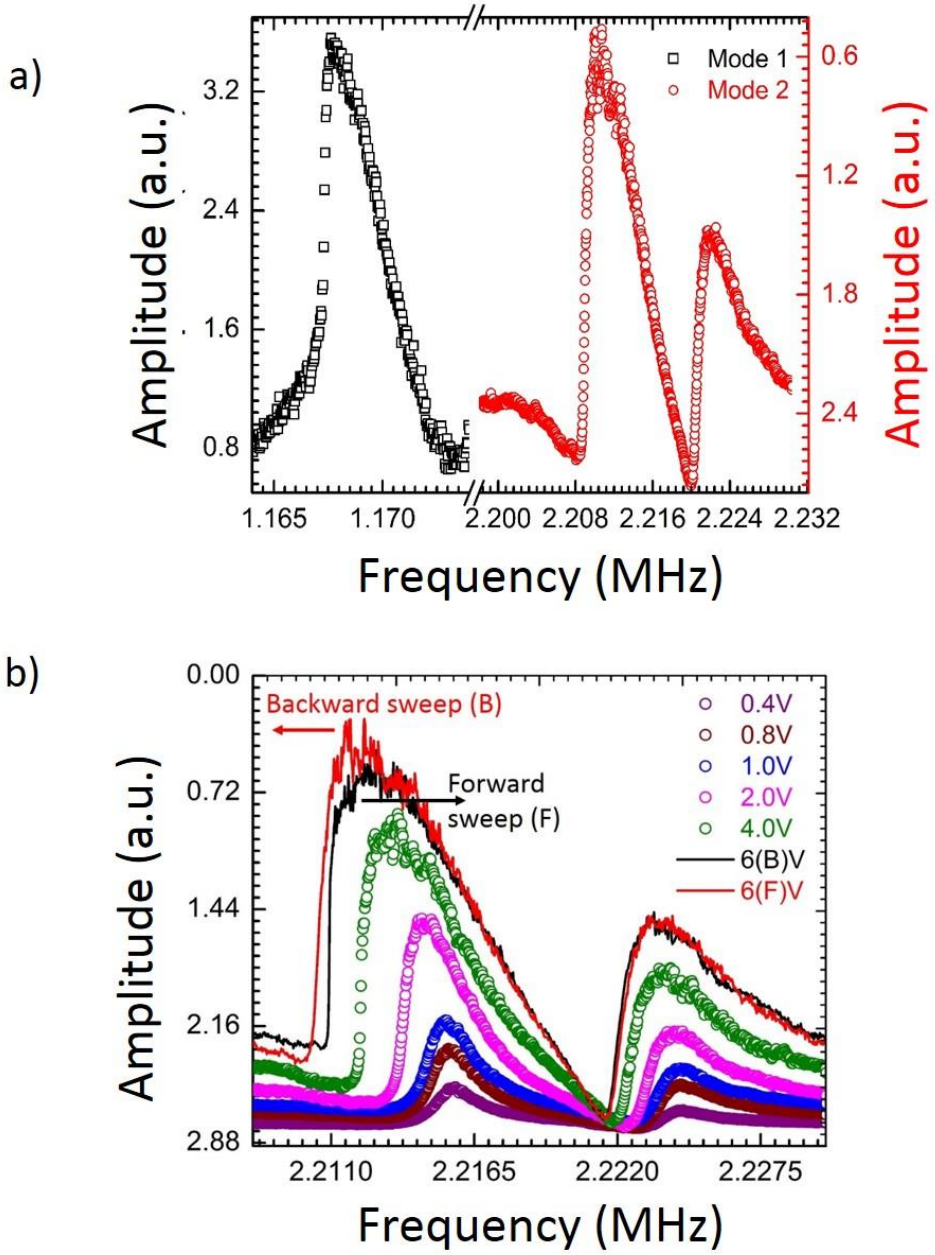

Figure 4. 10 a) First and second mode of the Duffing resonator (device 4). b) The second mode frequency response of device 4 with different V_{Ext} and constant V_{Inp} = 100mV.

For non-linear systems such as Duffing resonators, the frequency response due to harmonic force excitation at ω may have extra harmonics ($\omega = n\omega_0$) [102,104] where $n \neq 1$. Figure 4. 11 shows small peaks in addition to the resonance frequency of a Duffing resonator for different devices. The amplitude of this peak to that of the main resonance frequency varies for different devices as shown in Figure 4. 11a-c. For device 4, the amplitude of this extra peak just before the resonance peak (as shown in Figure 4. 11a) is quite large compared with other devices. Additionally in other devices also we mostly observe these extra peaks just before the resonance peak as shown in Figure 4. 11b-c, but with different relative amplitudes to main the resonance peak. These peaks start appearing as we increase the non-linearity in the system as shown in Figure 4. 11c. At V_{Ext} = 0.4 V the extra peak starts appearing and the amplitude increases further as we increase the V_{Ext}. Change in amplitude, frequency and nonlinearity introduced in these additional peak as we increase the amplitude of excitation, confirms that it represents mechanical resonance but not any electrical resonance. I couldn't determine the exact reason for these extra peaks but from the similar trend in many devices we can confirm that the effect starts appearing as soon as the non-linearity in the system increases as shown in Figure 4. 11. This can be some extra harmonics (sub-harmonics) present in the system due to the Duffing behavior. A potential explanation for this observation of that the additional peak in the Figure 4. 11 could be internal resonance peak [102].

In a nonlinear system, when the system is excited by a harmonic force, the response

can have higher and (or) lower harmonics other than that particular external excitation harmonic. These extra harmonics are very small signals and are usually buried under other parasitic and noise signals. However, at the resonance frequency when the system is very sensitive to excitation, it is possible to observe these extra harmonics in a nonlinear system

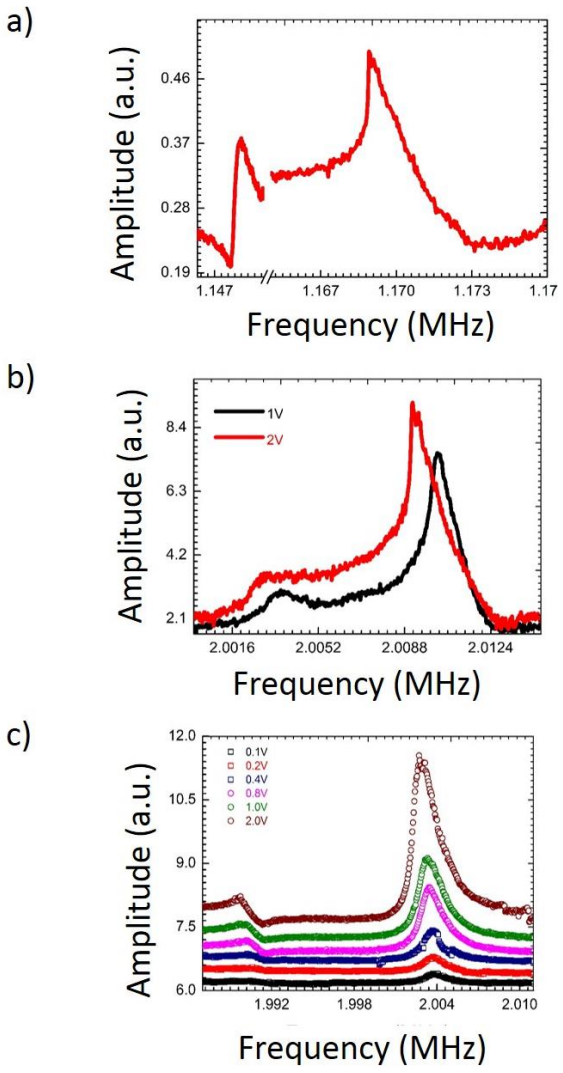

Figure 4. 11 a-b) The extra harmonics in the frequency response, other than the fundamental harmonic just before the f_o for device 4 (a) and device 5 (b). c) The resonance frequency response of device 6 with different V_{Ext} and constant V_{Inp}.

if we have an ultrasensitive read out method to transduce the signal effectively. Hence if we excite a cubic nonlinear system by a fundamental harmonic (ω) of the system, we can observe signals at subharmonic ($\omega/3$) and super-harmonic (3ω). Hence for a subharmonic system when the system is excited with a signal $x_1(t) = A \sin(\omega t)$ the response signal $x_2(t) = B \sin(\omega t) + C \sin(\omega t/3)$ will have a signal at ω as well as at $\omega/3$. Similarly for super-harmonic systems when it is excited with a signal $x_1(t) = A \sin(\omega t)$, the response signal $x_2(t) = B \sin(\omega t) + C \sin(3\omega t)$ will have a vibration signal at ω as well as at 3ω. To demonstrate this effect experimentally, after finding the resonance frequency, the resonator is driven at the resonance frequency and the real time data is taken using an oscilloscope. Figure 4. 12a shows a non-sinusoidal behavior of time domain signal of the device indicating nonlinearity and the presence of more than one harmonic. Whilst exciting the device 4 at resonance frequency ω, we have measured the amplitude of the vibration simultaneously at ω and $3\omega_0$ as shown in Figure 4. 12b. Figure 4. 12b is the FFT of time domain signal from device shown in Figure 4. 12a. The presence of a super-harmonic further confirms that the system is a nonlinear Duffing resonator.

4.2.2 Higher order nonlinear damping: van der Pol system [21,101-2]

For nanomechanical resonators (NMR) with dimensions less than 10 nm, , damping is found to strongly depend on the amplitude of motion and cannot be described by a linear damping model $\gamma(dx/dt)$, as with NMR based on nanotubes and graphene where the transverse dimension is sub-nanometer. Earlier we had modelled dissipation of motion due to linear damping force $F_{damp} = \gamma(dx/dt)$, caused by resistance to motion due to friction, viscosity due to surrounding air or any other fluids, and other forces acting on the system.

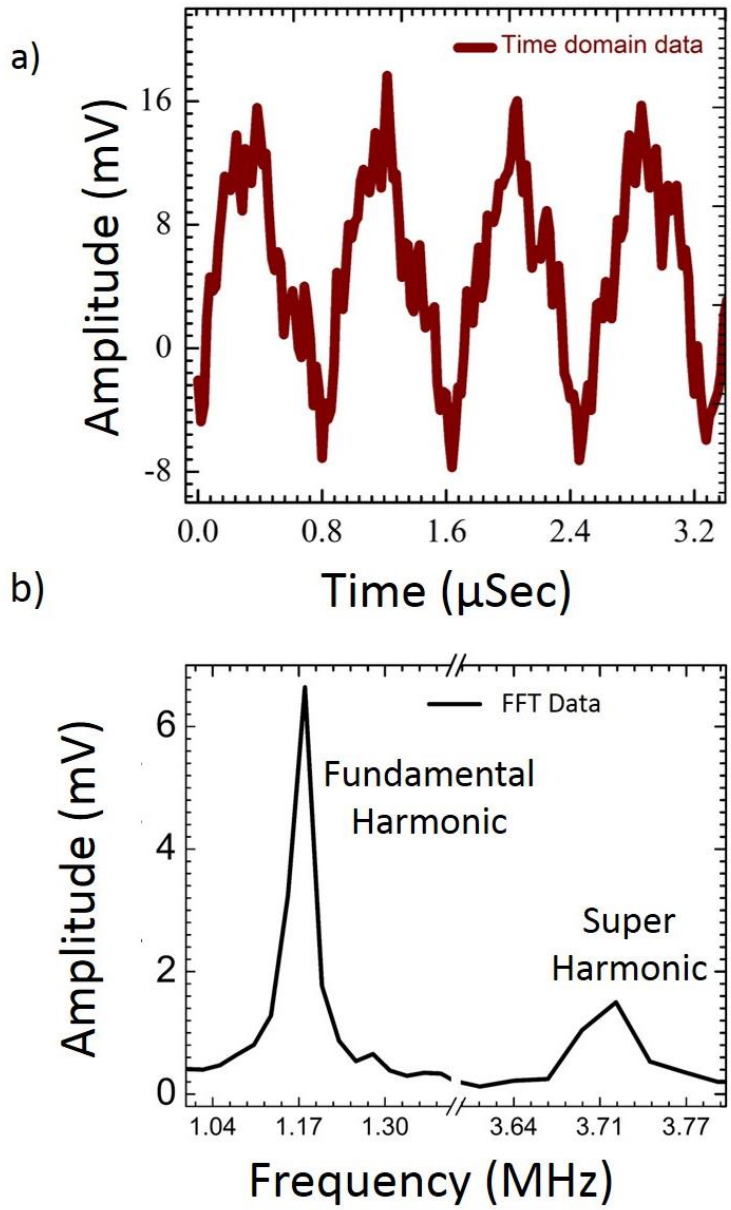

Figure 4. 12 a) The non-sinusoidal time domain signal of a nonlinear system (Device 4). b) FFT of the time domain signal of the above figure, showing fundamental and 3rd harmonic (super harmonics) of a nonlinear system (Device 4)

viscosity due to surrounding air or any other fluids, and other forces acting on the system. Now let's consider damping caused by linear as well as nonlinear damping as shown in Figure 4. 4, therefore the total damping force becomes $F_{Damp} = c\,(dx/dt) = (\gamma + \eta x^2)(dx/dt)$, where η is the coefficient of nonlinear damping. Hence the equation of motion for a nonlinear system has to be modified by including the higher order nonlinear damping term $\eta x^2(dx/dt)$ in equation 4.16 [21,101-2]. Thus for small resonators (sub nanometre) at the resonance frequency, the motion of the resonator is very sensitive to the driving force. Consequently, due to large motional amplitude $\eta x^2(dx/dt)$ is dominant over $\gamma(dx/dt)$.

$$M\left(\frac{d^2x}{dt^2}\right) + \ (\gamma + \eta x^2)\left(\frac{dx}{dt}\right) + \ kx \ = \ Fsin(\omega t) \qquad (4.17)$$

Van der Pol's equation 4.17 [102,105], describes the motion of a resonator with nonlinear damping. However the equation 4.17 has to be modified for nonlinear resonators including the Duffing force and can be written as: [101-2]

$$M\left(\frac{d^2x}{dt^2}\right) + \ (\gamma + \eta x^2)\left(\frac{dx}{dt}\right) + \ kx + \ \alpha x^3 \ = \ Fsin(\omega t) \qquad (4.18)$$

Equation 4.18 describes a van der pol-Duffing system. Including a Duffing term in a van der pol equation represents one of the most common examples of nonlinear oscillations for various mechanical and electrical systems.

I have solved equation 4.18 using MATLAB® for different values of the parameters γ, η , k, α, and F to understand the frequency response of a Pol-Duffing resonator. Figure 4. 13a shows the simulation data of the effect of different values of η varying from 0 to 1 for

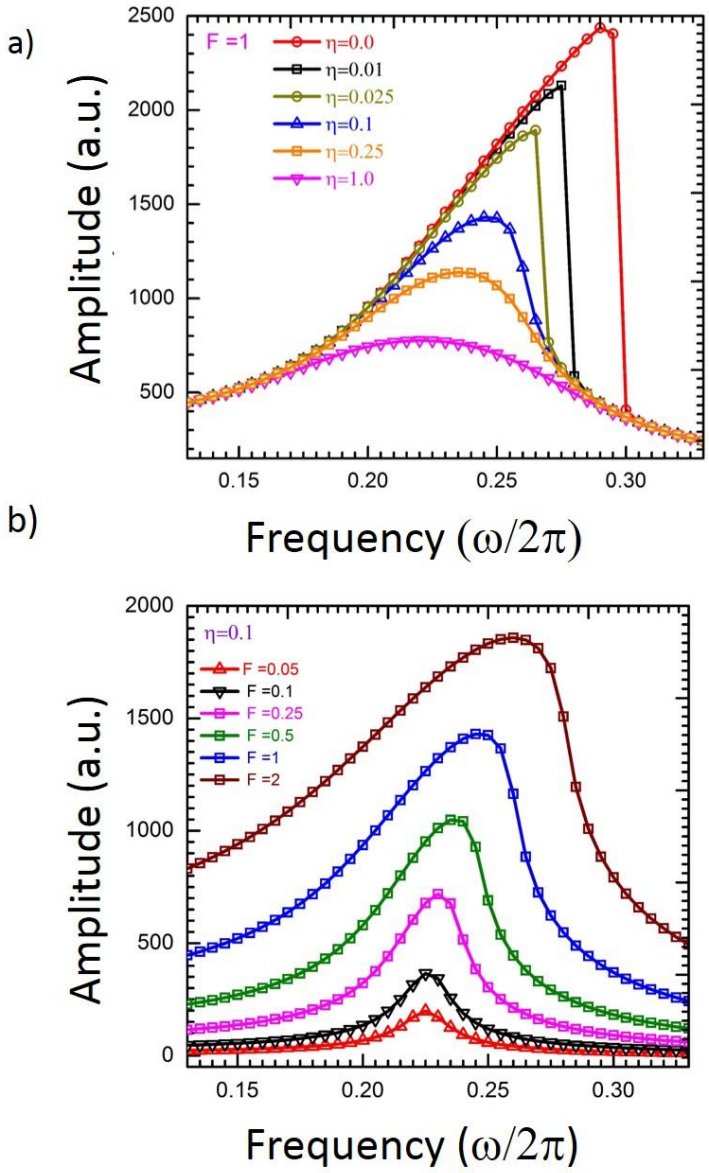

Figure 4. 13 Simulation data of the resonance frequency response of a Pol-Duffing system with η (a) and F (b) at constant $\alpha = +0.1$

a positive nonlinear spring constant ($\alpha = 0.1$) of a Duffing resonator. For smaller values of η (< 0.1) the frequency response is similar to a typical Duffing resonator with a clear and large jump in the amplitude at the saddle-node bifurcation point. As we start increasing the nonlinear damping coefficient, the frequency responses departs from a typical Duffing resonator. As we increase η not only the amplitude of the vibration decreases but also the resonance frequency starts decreasing (for a positive nonlinear spring constant) as shown in Figure 4. 13a. The decrease in amplitude is due to the increase in damping in the system. The decrease in resonance frequency indicates that the nonlinear damping force due to η, acts against the nonlinear restoring force due to α. Hence in this case of positive nonlinear spring effect, α tries to make the resonator more stiff whilst η makes the resonator less stiff and hence α and η act against each other. However keeping α and η constant and equal to 0.1, as we increase F, not only amplitude but also effects due to α (Duffing behavior) and η (broadening of peak due to damping) also increases as shown in Figure 4. 13b.

Previously an electrostatic actuation [21] technique has been employed to study the nonlinear damping of mechanical resonators based on nanotubes and graphene (with sub-nanometer dimensions), where an oscillation voltage V^{ac} at frequency f (resonance frequency) is applied between the resonator and gate electrode as shown in the Figure 3.1a. Capacitive detection techniques are employed to detect the motion of the resonator, and mixing current (I_{mix}) is measured with different V^{ac}. Unlike the linear damping model, in these resonators as we increase the driving force, asymmetry (bistability) in the

resonance peak is observed and Q is strongly dependent on the driving force. Hence Q = $f_o/\Delta f$ does not hold for the nonlinear damping model, and a new expression for Q, (or Δf) for a nonlinear damped resonator is given by equation 4.19 [21] which fits up to a certain

$$\Delta f = 0.3\ 2m^{-1}\eta^{1/3}f_o^{-2/3}F^{2/3}_{drive} \quad (4.19)$$

extent *w*ith experimental data.

For a nonlinear system such as a Pol-Duffing resonator, as we increase the amplitude of the driving force we may observe effect of both nonlinear damping as well as Duffing nonlinearity. Figure 4. 14a shows the frequency response of one of the devices (device 7) for different values of V_{Ext} and constant V_{Inp} = 75mV. The resonator starts behaving more like a Duffing resonator (broadening of peak) from V_{Ext} = 0.8V till 4V. As we increase V_{Ext} further, at 6V the single resonance peak splits into three branches. The curve not only has a sharp resonance peak at f_o = 1.1908 MHz but also other broad peaks at f_L = 1.1895 MHz and f_H = 1.19309 MHz. Splitting of resonance peak indicates Pol-Duffing nonlinearity in the system [21]. One of the reasons for such nonlinearity could be the non-linearity in the piezoresistive coefficient [90] itself (including the higher terms) and hence the piezoresistivity (output signal).

$$\frac{d\rho}{\rho} = \pi_1 T + \pi_2 T^2 + \pi_3 T^3 + \pi_4 T^4 \ldots\ldots, \quad (4.20)$$

Where T is applied stress, π_i is the i^{th} order piezoresistance coefficient and ρ is the resistivity of the material. Figure 4. 14b shows the hysteresis in the resonance frequency of the

resonator while sweeping the frequency in a forward (black line) and backward direction (red line) for $V_{Ext.}$= 6V and $V_{Inp.}$= 40V.

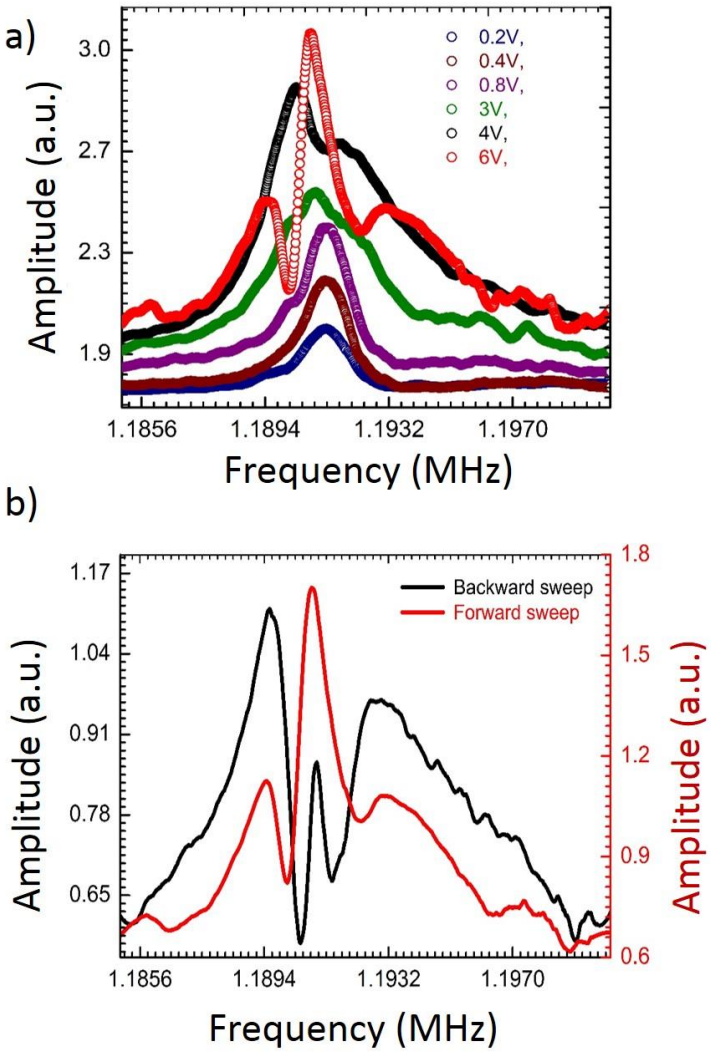

Figure 4. 14 a) The resonance frequency response of device 7 with different V_{Ext} and constant V_{Inp} = 75mV. b) Hysteresis in the resonance frequency of the resonator while sweeping frequency in forward (black line) and backward direction (red line).

Thus, this demonstrates nonlinearity in the spring constant as well as damping in Thus, this demonstrates nonlinearity in the spring constant as well as damping in the graphene resonator. This nonlinearity provides a new opportunity for application in NEMS devices, which has not been exploited before. For instance, we can use the non-linear response of our graphene-based NEMS to achieve new records in mass sensing.

4.3 To summarize characteristics of nonlinear vibration:

- The amplitude of the vibration affects the frequency of vibration, hence the frequency of the vibration is dependent on the amplitude.
- *Jump phenomenon*: As we increase the amplitude of vibration, we observe a sudden jump either up or down in the amplitude of vibration, indicating the instability of the system (saddle node bifurcation).
- *Sub or super harmonics*: When a system is excited at a particular harmonic force (ω), the output response will not only have the fundamental component but also may contain higher (super harmonics, 3ω) or lower harmonics (sub harmonics, $\omega/3$).
- *Pol-Duffing system:* For nanomechanical resonators (NMR) based on graphene where dimensions are less than 1 nm, damping is found to strongly depend on the amplitude of motion, and thus equation of motion is modelled using *Pol-Duffing system*.
- If we keep increasing the amplitude of vibration the system can become unstable and mode splitting can take place.

In conclusion, I have characterized and quantified the nonlinearity in graphene to enable design of high performing sensor. I have demonstrated the inherent variability in device parameters as well as the variability in the nonlinearity of these parameters. Thus we have shown a positive as well as negative Duffing-Pol system with different nonlinear coefficients.

Hence we have shown nonlinearity in the spring constant (both positive and negative) as well as in the damping of a graphene resonator. Thereby enabling the understanding of the onset of nonlinearity in such devices, which is particularly important for two-dimensional layers such as graphene. We have observed internal resonance in graphene resonator due to cubic nonlinearity in the coupled mode. This nonlinearity provides a new opportunity for application in NEMS devices, which has never been exploited before. For instance, we can use the non-linear response of our graphene-based NEMS to achieve new records in mass sensing.

Mostly we design linear system. But for graphene NEMS due to its atomically thick structure, the operation regime is bound by Duffing nonlinearity, mode splitting, internal resonance and nonlinear damping. Hence nano system and sensors design using graphene to operate in the linear regime have multiple constraint on excitation as well as measurements. This therefore calls for further enquiry utilizing nonlinearity rather than avoiding or ignoring it.

Chapter 5

Mode splitting in graphene resonator

In this chapter I shall talk about the higher modes along with the fundamental resonance modes of graphene resonator. Splitting of resonance peak in antisymmetric mode takes place not only due to the presence defects due to fabrication and irradiation, but also due to asymmetry in the legs of an H shape graphene resonator. I have also shown the frequency response of the resonator by systematically varying the length of the legs of the resonator. The experimental results verify the expected theory very well and the FEM model.

5.1 Splitting of resonance peak in higher Modes

Higher modes of the resonator have been transduced piezoresistively as shown in the previous chapters. One of the higher modes (antisymmetric) as modelled by FEM is shown in Figure 2.2c. In this mode, at resonance frequency, the two support legs move in opposite directions. Figure 5. 1 shows splitting of higher resonance modes in these resonators. Splitting of resonance modes [106-108] is commonly observed in micro (or nano) resonators. For example it has been observed in a nanowire that a small asymmetry in the cross-section can break the single vibrational resonance peak into two closely spaced

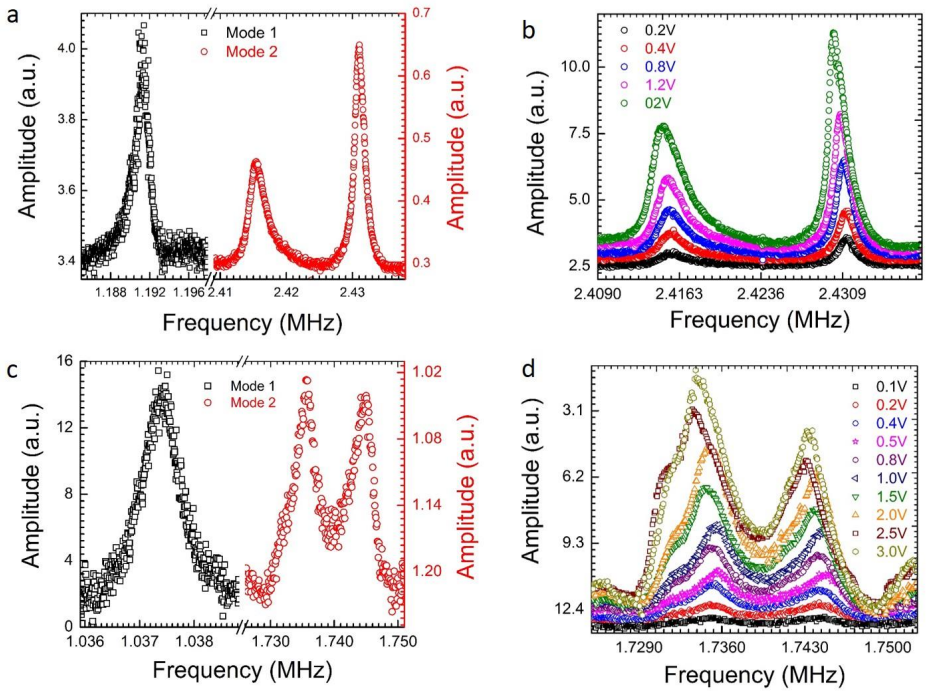

Figure 5. 1 a) Fundamental mode resonance f_o (black hollow squares) and the higher modes f_1 (red hollow circles) of device 1. b) The second mode frequency response of device 1 with different V_{Ext} and constant V_{Inp} = 40mV. c) f_o and f_1 for device 2. (d) The second mode frequency response of device 2 with different V_{Ext} and constant V_{Inp} = 100mV

peaks [106-108]. Presence of asymmetry in the legs of a H shape graphene resonator (which are more like nanoribbons) due to rippling, curving of the graphene membrane at the edges can break the mode in two single vibrational resonance peak (as shown in Figure 5. 1). Presence of defects due to fabrication and irradiation results in resonant mode splitting in carbon nanotube resonators [108]. It can be also one of the reasons of mode splitting in our system, as fabrication defects are unavoidable along with irradiation defects due to imaging during characterization of the devices (as shown by D peak in Raman spectra of the device, Figure 2.14). Rippling, slack or adsorbed mass can result in additional Eigen modes in a graphene resonator [59, 67].

5.1.1 Splitting of resonance peak due to asymmetry in shape [106]

It is observed in the nanowire that a small asymmetry in the cross-section can break the single vibrational resonance peak into two closely spaced peaks. Presence of asymmetry in the legs of H shape graphene resonator due to rippling, curving of the graphene membrane at the edges can break the antisymmetric mode in two single vibrational resonance peak. The splitting of peak is observed due to higher quality factor (Q ~ 10^3) of these resonator only, otherwise a low Q resonator would not have the bandwidth to observe this experimentally. Splitting in the peak has been observed in the commercial two beam (V and Π shaped) resonator as shown in Figure 5. 3a-d. But it is not observed in the single beam cantilever resonator as shown in Figure 5. 3e-f. It is interesting to observe that this splitting is observed in the antisymmetric mode only neither in the former nor later symmetrical mode. Hence, it indicates that this splitting due to asymmetry in the cross-section of the beam is more pronounced due to large length to thickness ratio (> 10^2) similar to the H shape resonator in this thesis. In the case of nanowire, it is shown that asymmetry in the cross-section of even 0.1 nm with a diameter of 100 nm is sufficient to split resonance peaks in vacuum [106]. Considering all the present measurements are in vacuum, it is expected that even a small asymmetry in the legs (width ~ 100nm) of the resonator will result in splitting of peaks.

Figure 5. 2 Distribution of the stress (left) and displacement (right) across the beam at the antisymmetric mode of the resonator. Due to asymmetry in the legs of the beam, stress is not distributed uniformly across the two free edges of the resonator and hence amplitude of vibration will be different.

5.1.2 Additional Eigen modes due to rippling, slack or adsorbed mass [59, 67]

Rippling, slack or adsorbed mass can result into some additional modified Eigen modes in graphene resonator [59, 67]. Rippling and curving at the edges are mostly observed in the graphene nano ribbon resonators. SEM images (Figure 2.10) of the resonator shows curving of the graphene membrane at the edges which can change the measured Eigen modes. Splitting of the higher resonance modes can also be the result of these additional Eigen modes, confirming that piezoresistive transduction is an effective and sensitive method to observe motion on graphene NEMS resonators. These unpredicted modes (generally unanticipated by standard elastic beam theory), is impractical to measure using optical and capacitive detection technique which depends on the average position of the resonator. Amplitude of vibration is largest along one of the free edges rather than at the centre of the beam in this case. Hence, in H shape beam at the antisymmetric mode, where the resonator vibrates as two coupled beam vibrating in two opposite directions, the

symmetry of vibration can break easily with one leg vibrating with much higher amplitude than the other. This is also observed in the Modal analysis (Figure 5. 2) when the symmetry of the two legs are broken. In H shaped graphene, as the clamping edges are completely separated it is possible to have an additional Eigen mode at or nearby the antisymmetric mode.

5.2 Higher mode of H shape graphene resonator

Frequency responses for two devices at higher modes is shown in Figure 5. 1. Figure 5. 1a shows the fundamental resonance frequency (f_o) at 1.19MHz and higher frequency mode (f_1) at around 2.2 MHz for device 1. Figure 5. 1c shows the fundamental resonance frequency (f_o) at 1.10375MHz and higher modes (f_1) at 1.74 MHz for the device 2. Figure 5. 1b shows driven response at f_1 with different V_{Ext} at constant V_{Inp} = 40mV for device 1; the decrease in f_1 with increase in V_{Ext} is similar to that of f_o shown in Figure 3.3a. For device 2, Figure 5. 1d shows the response of f_1 with different V_{Ext} at constant V_{Inp} = 100mV. We observe that there is less variation in the frequency i.e. the degenerated peaks are closer to each other compared to device 1. The resonance response upon increasing drive amplitude for this device (Figure 5. 1d) is similar to the f_o shown in Figure 3.3b. The measured value of f_1 is 2.2 MHz for device 1 and 1.7 MHz for device 2, the same order as calculated using FEM model (Figure 2.2c). For device 1, the splitting is prominent as we can see two distinct peaks very close to each other (Figure 5. 1a-b), while for device 2 the splitting is relatively small compared to device 1 (as shown in Figure 5. 1c-d but still clearly

discernible. This is most probably because the amount of asymmetry due to defects and structure in the two devices are different. It has been shown earlier that magnitude of splitting increases with degree of asymmetry in the resonators [106]. This ability to transduce motion in the higher modes is further proof of piezoresistive transduction and also underlines the sensitivity of this detection scheme.

5.3 Mode splitting in higher modes of commercial cantilevers.

Such dual modes at higher Eigen modes are observable in other mechanical systems made by microfabrication methods, such as triangular cantilevers in atomic force microscopy (AFM) as shown in Figure 5. 3. As shown in Figure 5. 1, double resonance peak at the higher resonance modes has been observed in the H shape graphene resonator. In order to verify that this is not simply an artefact of the measurement, the resonance frequency of some commercially available, V (Thindiamond: ND-CTIT2S) and □ (Nanosensors: A-PROBE-SPL) shaped double beam cantilever has been measured in an AFM using optical read-out as shown in Figure 5. 3. Figure 5. 3b shows the fundamental resonance frequency (f0) ~ 40 kHz and higher modes ~ 250 KHz of the V shape cantilever (SEM image of V shape cantilever is shown in Figure 5. 3a). Similarly, Figure 5. 3d shows the fundamental resonance frequency (f0) ~ 69 kHz and higher modes ~ 350 KHz of the □ shape cantilever (SEM image of □□shape cantilever is shown in Figure 5. 3c). It is observed that the higher modes has split into two peaks, for the two cantilever as shown in Figure 5. 3b and d, as is the case in the H shape graphene resonator. The origin of this behavior is the

motion of these two arms at slightly different frequencies due to asymmetry (or defects) [106-107] in the two arms. This independently indicates that Figure 5. 1 shows higher modes of our H shaped graphene resonators. Simple cantilevers (Budget sensors: ElectriMulti75-G: Figure 5. 3e shows SEM

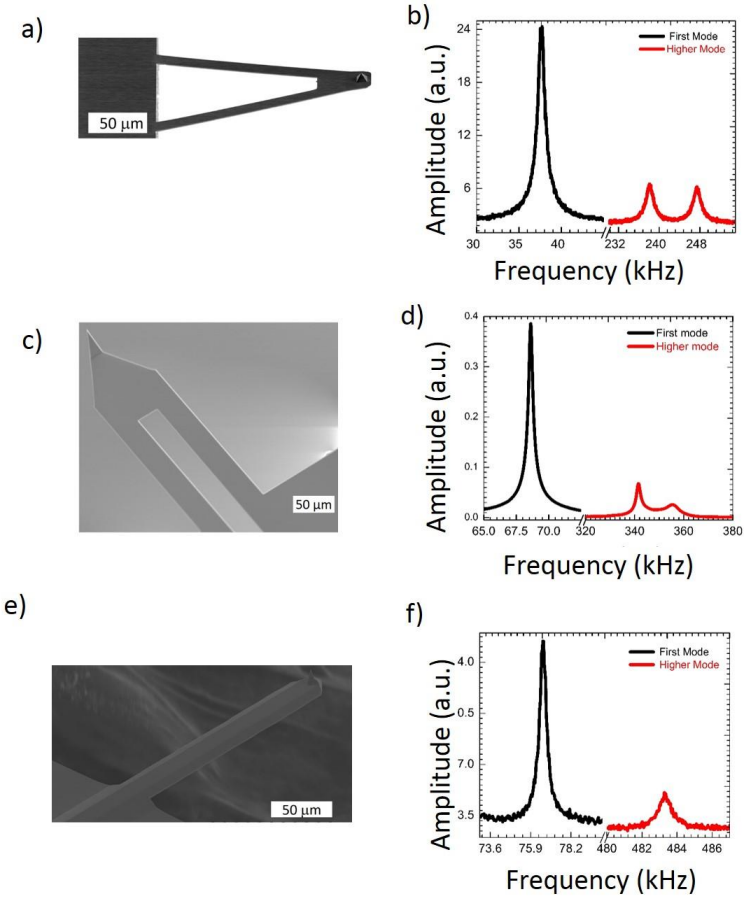

Figure 5. 3 SEM image of commercially available Cantilever and their frequency response: a) V-shaped cantilever (Thindiamond: ND-CTIT2S); b) First and higher resonance modes of the cantilevers shown in Figure a. c) Another two beam cantilever (Nanosensors: A-PROBE-SPL) d) First and higher resonance modes of the cantilevers shown in Figure c. e) Simple cantilever (Budget sensors: ElectriMulti75-G); f) First and higher resonance modes for cantilevers shown in Figure e.

image of such cantilever) as shown in Figure 5. 3f do not display this behavior, which rule out any measurement artefacts as the cause of this.

5.4 Fundamental and higher mode of Π shaped graphene resonator

Figure 5. 4 shows SEM images of Π shape graphene resonators. Frequency response of the Π shape graphene resonator is shown in Figure 5. 5. Higher mode f_1 of the Π shape resonator is shown in Figure 5. 5a at V_{Ext} = 2V with different V_{Int}. It is observed that as the V_{Int} is increased while keeping V_{Ext} constant, the shape of the frequency response become asymmetrical. At V_{Int} = 40mV the amplitude of resonance (peak) and anti-resonance (dip) is same. At V_{Int} = 100mV the amplitude of the resonance peak increase while amplitude of the anti-resonance dip decreases. It can be observed that the thermal fluctuations ($V_{Int.}$) induces strong coupling between the resonance and anti-resonance modes, this is an excellent verification of the predicted theory [109]. Figure 5. 5b shows hysteresis in f_1 of another such device while sweeping frequency forward and backward at V_{Ext} = 5V and V_{Int} = 80mV. Figure 5. 5c shows f_1 of same device at V_{Ext} = 1V with different V_{Int}. As we increase V_{Int} and hence, power applied to the resonator, resonance frequency remains nearly constant while the amplitude of both the resonance peak and anti- resonance dip increases. I have verified the predicted theory [109] excellently by showing broadening of the resonance peaks and hence quality factor with the thermal motion ($V_{Int.}$) due to the internally induced damping. Figure 5. 5d shows f_1 of same device at V_{Int} = 120 V with different V_{Ext}. As we increase the amplitude of vibration unlike Figure 5. 5c f_1 changes and goes towards lower value indicating capacitive softening [26,62,65,94-96] is observed as shown earlier in H shape graphene resonator (Figure 3.3a and 3.12). It is worth noting that

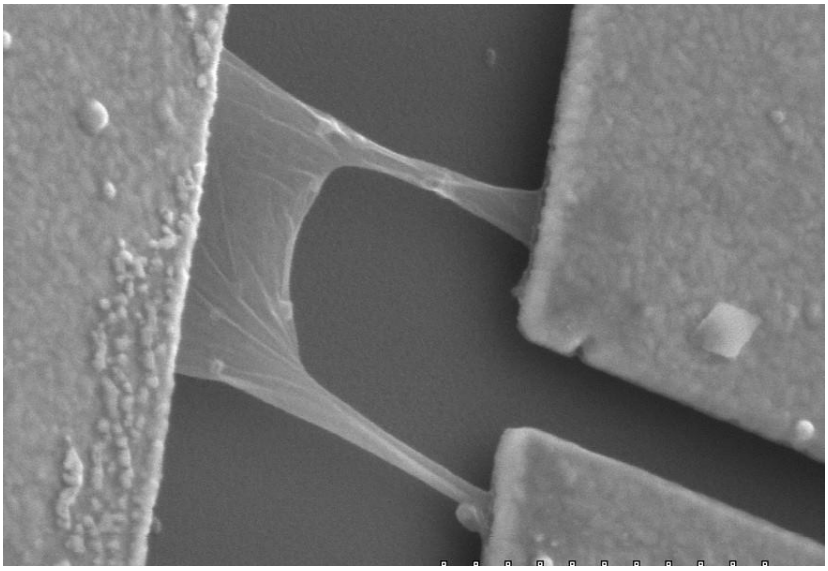

Figure 5. 4 SEM image of Π shape graphene resonator.

that for this device as we increase V_{Ext} amplitude of resonance peak increases relatively more than the amplitude of the anti-resonance dip.

Figure 5. 6a and b shows deformed shape of a three sided clamped Π shaped graphene resonator at fundamental frequency f_0 = 1.064 MHz and second mode shape f_1 = 1.088MHz respectively. The two modes are close to each other as expected. Due to residual mass of impurities on the graphene resonator due to fabrcation [61], I have consider mass density of the beam $(\rho) = 5 \times \rho_{graphene.}$ Dimension of the these resonator are considered according to the fabricated real devices (shown in Figure 5. 4) with 2 µm long, 1.2 µm wide, each leg being ~ 100 nm wide. Resonance frequencies have been measured between 1-2 MHz for most of these resonators as shown in Figure 5. 5. It has been found that these frequencies are of the same order as calculated using FEM (Figure 5. 6) taking into account of higher mass density. The reason for the two modes to be close to each other is that

the system behaves as an array of two-coupled resonator. In this system, each nano-graphene beam with 2 µm long and 100 nm wide acts as a resonator, which has been coupled through a central part with ~ 180 - 220nm long and 800-900 nm wide, at one end of the beam. Modal analysis confirms the two modes observed close to each other experimentally in Figure 5. 5

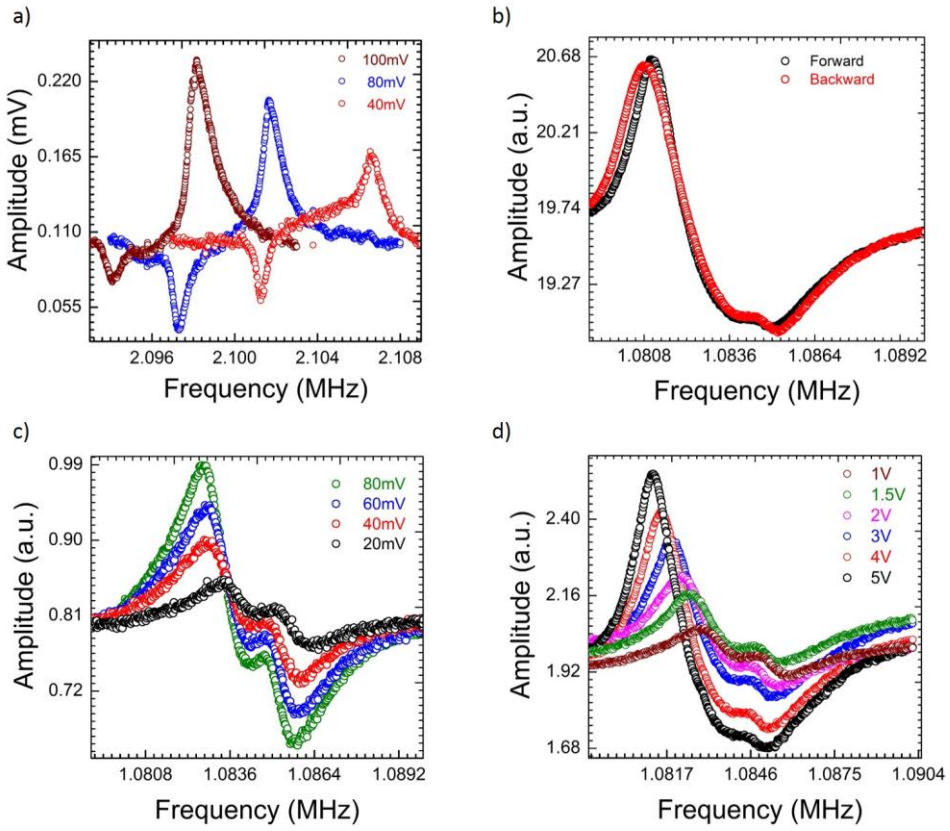

Figure 5. 5 The resonance frequency response of the Π shape resonator. a) f_0 and f_1 of Π shape resonator shown in figure 5.4 with different V_{Int} and constant V_{Ext} = 2V. b) Hysteresis in resonance frequency response of device 9 (another Π shape resonator) at V_{Ext} = 5V and V_{Int} = 80mV. The resonance frequency response of same device with different V_{Int} and at V_{Ext} = 1V (c) and with different V_{Ext} and at V_{Int} = 120 V (d).

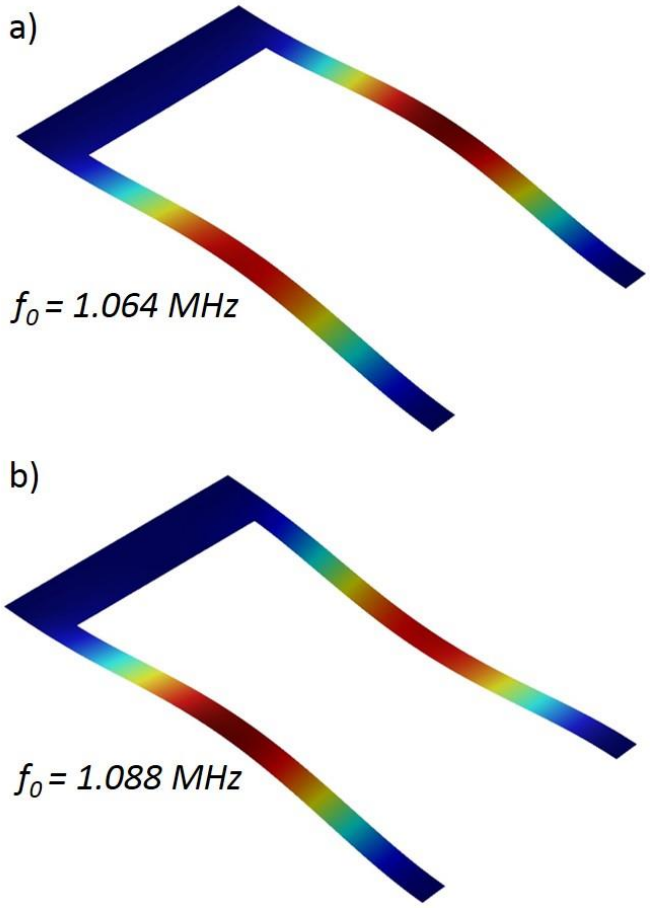

Figure 5. 6 Modal analysis using FEM I The deformed shape of a three sided clamped Π shaped graphene resonator at resonance at c) fundamental frequency (f_0) and at b) second mode shape (f_1).The colour code shows amount of amplitude of vibration, red colour indicates maximum displacement whereas blue colour shows minimum displacement.

5.5 Conclusions

In conclusion we have shown higher modes along with the fundamental resonance mode of two different kind of designs of graphene resonator; H shaped, and Π shaped. The results are verified with the measurements on commercial available beams. I have observed that by systematically changing the aspect ratio of the arms and resonator, we

could potentially control the resonance frequency and hence the quality factor. Strong coupling has been observed between different modes of the Π shaped graphene resonator due to thermal fluctuation. Both the two arms can be routinely functionalized to beam. Two different sensors both of which can be monitored using just the single response. This means that this design actually become two in one sensors. This also suggest that one can design a large array of similar resonator thereby producing a coupled array of large number of sensors. I have identified and characterized particular modes in graphene resonator using different NEMS design. The results are excellent verification of the theory, and give a useful result for graphene NEMS design.

Chapter 6

Concluding remarks

6.1 Conclusions

In conclusion, piezoresistive sensing of graphene based nanoelectromechanical system has been demonstrated. In this piezoresistive transduction method, the intrinsic piezoresistivity of graphene has been utilized as a self-sensing component to transduce the motion of graphene resonator. It has been demonstrated that piezoresistive sensing is not only a simple but very effective electrical readout method for graphene based nanoelectromechanical systems. To maximize the piezoresistive effect of graphene, a four-sided clamped H shaped graphene beam has been employed. Fundamental resonance frequency (f_o) of the devices has been measured at around 1-3MHz. These graphene resonators show very high quality factors as high as 1000-2000 in ambient temperatures and pressures of ~ 4×10^{-6} Torr which is one order higher than the previous reported values for double side clamped beams. The minimum detectable mass of such resonators is calculated to be an astounding 0.95 – 1.54 zeptograms (10^{-21} g) at room temperature. By transducing thermomechanical motion of these resonators minimum force resolution is estimated to be 11.7 – 21.6 aN/Hz$^{1/2}$ at room temperature. The sensitivity of the detection

technique is further demonstrated by detecting peak splitting in the second order resonance mode of the resonator, underlining the resolution of this technique.

In order to use NEMS for sensing applications, onset of non-linearity in the devices has been characterized. This addresses the basic understanding of nonlinearities in these devices and its origin. Duffing nonlinear behavior has been shown in the devices at higher external drive. Hysteresis is observed in f_o while sweeping frequency forward and backward. Due to the small dimensions of the resonators (width of the leg ~ 100 nm), nonlinear damping has been also shown at higher vibrational amplitude. The frequency response of some devices shows Pol-Duffing behavior. Hence nonlinearity in spring constant as well as higher order nonlinear damping, both have been shown in the devices. Further, the frequency response of the device with asymmetric shape has been measured. Higher modes along with the fundamental resonance mode have been measured for two different designs of graphene resonators; H shaped and Π shaped. The results are verified with measurements on commercial resonators. I have observed that by systematically changing the aspect ratio of the arms and the resonator, we can potentially control the resonance frequency and hence the quality factor. Strong coupling has been observed between different modes of the Π shaped graphene resonator due to thermal fluctuation. Key contributions of this thesis are:

- H shaped graphene resonator, has been successfully fabricated using standard lithography process. The very first demonstration of piezoresistive sensing of graphene based nanoelectromechanical systems has been carried out.
- It has been demonstrated that piezoresistive sensing is not only simple and sensitive but very effective for graphene based NEMS. One order higher Q-factors than the previous reported values for double side clamped beams in ambient temperatures has been measured. An astounding 0.95 – 1.54 zeptograms (10^{-21} g) of minimum detectable mass is estimated for such resonators at room temperature. Thermomechanical motion detection of these resonators allows us to estimate minimum force resolution of 11.7 – 21.6 aN/$Hz^{1/2}$ also at room temperature. The sensitivity of the detection technique is further demonstrated by detecting peak splitting in the second order resonance mode of the resonator.
- Onset of non-linearity in the devices has been characterized. Thus dynamic range as high as 60dB has been measured, which is highest reported value at room temperature. The basic understanding of nonlinearities in these devices and its origin such as Duffing behavior, hysteresis, nonlinear damping, and subharmonics have been carefully studied both experimentally as well as theoretically.
- Higher order modes along with the fundamental resonance mode have been measured for three different designs of graphene resonator; symmetrical H shaped, asymmetrical H shaped, and Π shaped.

- **6.2 Future applications**

The present work has been demonstrated on a scalable platform using a simple tabletop apparatus, which could hence be commercialized on hermetically sealed packages. Such high sensitivity at room temperature using CVD grown graphene could herald tabletop applications of hitherto low-temperature techniques such as MRFM and single molecule spectroscopy. Further investigation of techniques to use these for mass spectroscopy in vacuum could result in inexpensive and highly sensitive NEMS devices for applications in mass spectrometry.

6.2.1 Graphene-GST-Graphene: Tunable resonator

Graphene is a strong candidate as electrode and interconnect for wearable and flexible electronics due to its high conductance, current capacity, transparency and flexibility. Successful demonstration of graphene as a transparent electrode for display system has been shown [110]. GST ($Ge_2Sb_2Te_5$) [111] is an excellent memory device material that can switch both electrically and optically between amorphous and crystalline states. Its switching property can be used as a tunable resonator. But not being a very stiff material, a thin GST layer would need a support for being suspended. Graphene can be used as a bottom support for resonators based on GST. It will provide support as well as act as the bottom electrode to probe GST locally both electrically and optically. Figure 6. 1 shows a diagram of the proposed device [111]. A drum resonator comprising a graphene - $Ge_2Sb_2Te_5$ - graphene structure is placed on top of a hollow SiO_2 supporting substrate. As

already mentioned the two graphene electrodes would serve as active electrodes as well as the support and capping layers. Modeling based design of a tunable nanoelectro-mechanical system (NEMS) is capable of operating in the 800MHz to 1.9 GHz frequency band without the need of a constant electrostatic tuning stimuli [111]. Permanent, yet reversible, tuning of such a resonator in this region is possible, but only when the structural support platform is made of ultra-light and thin two-dimensional elements. Using graphene as the top and bottom electrodes with a layer of the well-known Phase Change Material (PCM) $Ge_2Sb_2Te_5$, a pathway can be provided for a highly functional NEMS that employ 2D electrodes and PCM in a tunable resonant circuits.

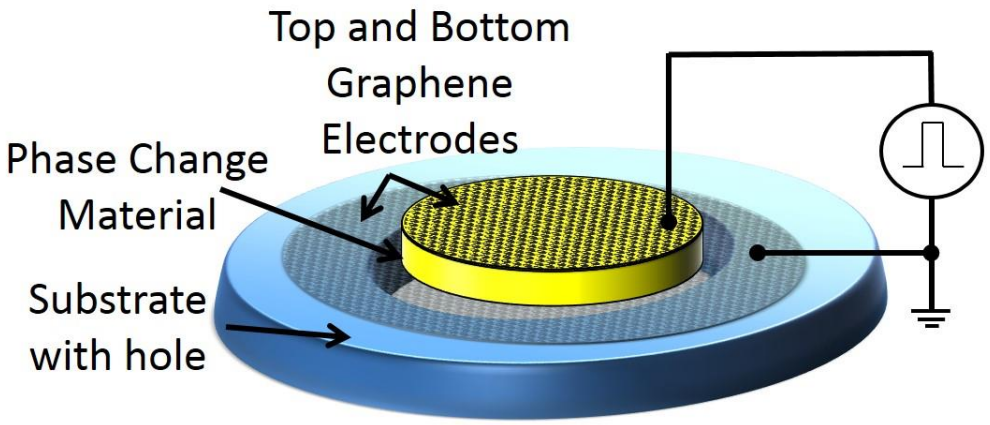

Figure 6. 1 shows a diagram of the proposed device [111]

Reference

1. Roukes, M. Plenty of Room Indeed *Scientific American*, **17**, 4-11 (2007).
2. Martínez, A. A. Replication of Coulomb's torsion balance experiment. *Arch. Hist. Exact Sci.* **60** 517–563 (2006).
3. Ekinci, K. L., Roukes, M. L., Nanoelectromechanical systems. *Rev. Sci. Instrum.* **76**, 061101 (2005).
4. Kumar, M., Bhaskaran, H. Ultrasensitive room temperature piezoresistive transduction in graphene-based nanoelectromechanical systems. *Nano Lett.* **15** (4), pp 2562–2567 (2015).
5. Kaajakari, V. *Practical MEMS.* Small Gear Pub. *(Las Vegas, Nev.)* (2009).
6. Feynman, R. P., Christopher, S. *No Ordinary Genius: The Illustrated Richard Feynman.* W. W. Norton & company (1995).
7. Feynman, R. P. There's Plenty of Room at the Bottom. *Engineering and Science*, California Institute of Technology, 1960.http://www.zyvex.com/nanotech/feynman.html
8. 'Plenty of room' revisited, editorial, *Nat. Nanotechnol.* **4** (2009).
9. Ball, P. Material witness: Miniature motors, *Nat. Mat.* **3**, 428 (2004).
10. Feynman, R. P. *Perfectly Reasonable Deviations from the Beaten Track 24-Copy Display* Basic Books (2005).
11. Rugar, D., Budakian, R., Mamin, H. J., Chui, B. W. Single spin detection by magnetic resonance force microscopy. *Nature* **430**, 329-332 (2004).

12. Kenny, T. Nanometer-scale force sensing with MEMS devices. *IEEE Sens. J.* **1**, 148 (2001).

13. Moser, J. *et al*. Ultrasensitive force detection with a nanotube mechanical resonator. *Nat. Nanotechnol.* **8**, 493–496 (2013).

14. Ekinci, K. L., Yang, Y. T., Roukes, M. L. Ultimate limits to inertial mass sensing based upon nanoelectromechanical systems. *J. Appl. Phys.* **95**, 2682 (2004).

15. Chaste, J. *et al.* Nanomechanical mass sensor with yoctogram resolution. *Nat. Nanotechnol.* **7**, 301–304 (2012).

16. Lassagne, B. *et al.* Ultrasensitive Mass Sensing with a with a nanotube electromechanical resonator. *Nano Lett.* **8** (11), 3735-3738 (2008).

17. Naik, A. K. *et at.* Towards single-molecule nanomechanical mass spectrometry. *Nat. Nanotechnol.* **4**, 445–450 (2009).

18. Hanay, M. S *et al.* Roukes, Single-protein nanomechanical mass spectrometry in real time. *Nat. Nanotechnol*. **7**, 602–608 (2012).

19. O'Connell, A. D. *et al.* Quantum ground state and single-phonon control of a mechanical resonator. *Nature* **464**, 697–703 (2010).

20. Rocheleau, T. *et al.* Preparation and detection of a mechanical resonator near the ground state of motion. *Nature* **463**, 72–75 (2010).

21. Eichler, A. *et al.* Nonlinear damping in mechanical resonators made from carbon nanotubes and graphene. *Nat. Nanotechnol*. **6**, 339–342 (2011).

22. Peng, H. B., Chang, C.W., Aloni, S., Yuzvinsky, T. D., Zettl, A. Ultrahigh Frequency Nanotube Resonators. *Phy. Rev. Lett.* **97,** 087203 (2006).
23. King Y. Fong, Wolfram H. P. Pernice, Hong X. Tang. Frequency and phase noise of ultrahigh Q silicon nitride nanomechanical resonators. *Phy. Rev. B.* **85**, 161410(R) (2012).
24. Moser, J., Eichler, A., Güttinger, J., Dykman, M. I., Bachtold, A. Nanotube mechanical resonators with quality factors of up to 5 million. *Nat. Nanotechnol*. **9** (12):1007-11 (2014).
25. Postma, H. W. C. *et at.* Dynamic range of nanotube- and nanowire-based electro-mechanical systems. *Appl. Phys. Lett.* **86**, 223105 (2005).
26. Kozinsky, I. *et al.* Tuning nonlinearity, dynamic range, and frequency of nanomech-anical resonators, *Appl. Phys. Lett.* **88**, 253101 (2006).
27. Zolfagharkhani, G. *et al.* Nanomechanical detection of itinerant electron spin flip. *Nat. Nanotechnol*. **3**, 720–723 (2008).
28. Teufel, J. D., Donner, T., Castellanos-Beltran, M. A., Harlow, J. W. & Lehnert, K. W. Nanomechanical motion measured with an imprecision below that at the standard quantum limit. *Nat. Nanotechnol*. **4**, 820–823 (2009).
29. Knobel, R. G. & Cleland, A. N. Nanometre-scale displacement sensing using a single electron transistor. *Nature* **424**, 291–293 (2003).

30. Poggio, M. *et al*. An off-board quantum point contact as a sensitive detector of cantilever motion. *Nature Phys.* **4**, 635–638 (2008).

31. LaHaye, M. D., Buu, O., Camarota, B. & Schwab, K. C. Approaching the quantum limit of a nanomechanical resonator. *Science* **304**, 74–77 (2004).

32. Anetsberger, G. *et al.* Near-field cavity optomechanics with nanomechanical oscillators. *Nature Phys*. **5**, 909 - 914 (2009).

33. Etaki, S. *et al.* Motion detection of a micromechanical resonator embedded in a d.c. SQUID. *Nature Phys.* **4**, 785–788 (2008).

34. Munday, J. N., Capasso, F. & Parsegian, V. A. Measured long-range repulsive Casimir-Lifshitz forces. *Nature* **457**, 170–173 (2009).

35. Geim, A. K., & Novoselov, K. S. The rise of graphene, *Nat. Mater.* **6**, 183-191 (2007).

36. Wallace, P. R. The band theory of graphite. *Phys. Rev.* **71**, 622–634 (1947).

37. Boehm, H., Clauss, A., Hofmann, U & Fischer, G. Dunnste Kohlenstof-Folien. *Z. Fur Naturforschung* **B 17**, 150 (1962).

38. Boehm, H., Setton, R. & Stumpp, E. Nomenclature and terminology of graphite intercalation compounds. *Carbon* **24**, 241-245 (1986).

39. Lee, C., W, X., Kysar, J.W., & Hone, J. Measurement of the elastic properties and intrinsic strength of monolayer graphene. *Science* **321** (5887), (2008).

40. Scientific American: Elephant Illustrates Important Point (2011).
http://www.scientificamerican.com/article/balancing-act/

41. Castro, E. V., Ochoa, H., Katsnelson, M. I., Gorbachev, R. V., Elias, D. C., Novoselov, K. S., Geim, A. K., & Guinea, F. Limits on charge carrier mobility in suspended graphene due to flexural phonons. *Phys. Rev. Lett.* **105**, 26660 (2010).

42. Morozov, S. V., Novoselov, K. S., Katsnelson, M. I., Schedin, F., Elias, D. C., Jaszczak, J. A., & Geim, A. K. Giant intrinsic carrier mobilities in graphene and its bilayer. *Phys. Rev. Lett* **100**, 1 (2008).

43. Bolotin, K. I. *et al.* Ultrahigh electron mobility in suspended graphene, *Solid State Commun.* **146**, 351–355 (2008).

44. Hosseini, E. S., Yegnanarayanan, S., Atabaki, A. H., Soltani, M. Adibi, A. High quality planar silicon nitride microdisk resonators for integrated photonics in the visible wavelength range. *Optics express* **17**(17), 14543–14551 (2009).

45. Sazonova, V. et al. A tunable carbon nanotube electromechanical oscillator. *Nature* **431**(7006), 284-287 (2004).

46. Huttel, A. K. *et al.* Carbon nanotubes as ultrahigh quality factor mechanical resonators. *Nano. Lett.* **9**(7), 25470-2552 (2009).

47. Steele, G. A. *et al.* Strong coupling between single-electron tunneling and nanomechanical motion. Science **325** (5944), 1103-1107 (2009).

48. Lassagne, B., Tarakanov, Y., Kinaret, J., Garcia-Sanchez, D. & Bachtold, A. Coupling mechanics to charge transport in carbon nanotube mechanical resonators. *Science* **325**(5944), 1107-1110 (2009).

49. Jensen, K., Kim, K. & Zettl, A. An atomic-resolution nanomechanical mass sensor. *Nat Nanotechnol*. **3**(9), 533-537 (2008).

50. Chiu, H.-Y., Hung, P., Postma, H. W. C. & Bockrath, M. Atomic-scale mass sensing using carbon nanotube resonators. *Nano Lett.* **8**(12), 4342-4346 (2008).

51. Feng, X. L., He, R., Yang, P. & Roukes, M. L. Very high frequency silicon nanowire electromechanical resonators. *Nano Lett.* **7**(7), 1953-1959 (2007).

52. Solanki, H. S. et al. Tuning mechanical modes and influence of charge screening in nanowire resonators. *Phy. Rev. B.* **81**(11) (2010).

53. Carr, D. W., Evoy, S., Sekaric, L., Craighead, H. G. & Parpia, J. M. Measurement of mechanical resonance and losses in nanometer scale silicon wires. *Apl. Phy. Lett.* **75**(7), 920-922 (1999).

54. Unterreithmeier, Q. P., Weig, E. M. & Kotthaus, J. P. Universal transduction scheme for nanomechanical systems based on dielectric forces. *Nature* **458**(7241), 1001-1004 (2009).

55. Li, X., Cai, W., An, J., Kim, S., Nah, J., Yang, D., Piner, R., Velamakanni, A., Jung, I., Tutuc, E., Banerjee, S. K., Colombo, L., & R. S. Ruoff. Large-area synthesis of high-quality and uniform graphene films on copper foils. *Science* **324** (5932), 1312–1314 (2009).

56. Kim, K. S., Zhao, Y., Jang, H., Lee, S. Y., Kim, J. M., Kim, K. S., Ahn, J. H. Kim, P., Choi, J. Y., & Hong. B. H., Large-scale pattern growth of graphene films for stretchable transparent electrodes. *Nature* **457** (7230), 706–710 (2009).

57. Chen, C., Hone, J. Graphene nanoelectromechanical systems. *Proc. IEEE* **101**, 1766–1779 (2013).

58. Bunch, J. S., Van der Zande, A. M., Verbridge, S. S., Frank, I. W., Tanenbaum, D. M., Parpia J. M., Craighead H. G., McEuen P. L. Electromechanical Resonators from Graphene Sheets. *Science* **315** (5811), 490-493(2007).

59. Garcia-Sanchez, D., Van der Zande, A. M., Paulo, A. S., Lassagne, B., McEuen, P. L., Bachtold, A. Imaging mechanical vibrations in suspended graphene sheets. *Nano Lett*. **8**(5), 1399–1403 (2008).

60. Bunch, J. S., Verbridge, S. S., Alden, J. S., van der Zande, A. M., Parpia, J. M., Craighead, H. G., McEuen P. L. Impermeable atomic membranes from graphene sheets. *Nano Lett.* **8**(8), 2458–2462 (2008).

61. Chen, C., Rosenblatt, S., Bolotin, K. I., Kalb, W., Kim, P., Kymissis, I., Stormer, H. L., Heinz, T. F., Hone, J. Performance of monolayer graphene nanomechanical resonators with electrical readout. *Nat. Nanotechnol*. **4**, 861-7 (2009).

62. Singh, V., Sengupta, S., Solanki, H. S., Dhall. R., Allain. A., Dhara., S., Pant, P., Deshmukh M. M. Probing thermal expansion of graphene and modal dispersion at

low-temperature using graphene nanoelectromechanical systems resonators., *Nanotechnology* **21**, 165204 (2010).

63. Van der Zande A. M., Barton, R. A., Alden, J. S., Ruiz-Vargas, C. S., Whitney, W. S., Pham, P. H. Q, Park. J., Parpia. J. M., Craighead, H. G., McEuen, P. L. Large-Scale Arrays of Single-Layer Graphene Resonators. *Nano Lett.* **10** (12), 4869–4873 (2010).
64. Stolyarova, E., Stolyarov, D., Bolotin, K., Ryu, S., Liu, L., Rim, K. T., Klima, M., Hybertsen, M., Pogorelsky, I., Pavlishin, I., Kusche, K., Hone, J., Kim, P., Stormer, H. L., Yakimenko, V., Flynn, G. Observation of graphene bubbles and effective mass transport under graphene films. *Nano Lett.* **9**(1), 332-7 (2009).
65. Song, X., Oksanen, M., Sillanpää, M. A., Craighead, H. G., Parpia, J. M., Hakonen, P. J. Stamp transferred suspended graphene mechanical resonators for radio frequency electrical readout. *Nano Lett.* **12**, 198–202 (2011).
66. Robinson, J. T, Zalalutdinov, M., Baldwin, J. W., Snow, E. S., Wei, Z., Sheehan, P., Houston, B. H. Wafer-scale Reduced Graphene Oxide Films for Nanomechanical Devices. *Nano Lett.* ***8*** (10), 3441-3445 (2008).
67. Shivaraman, S., Barton, R. A., Yu, X., Alden, J., Herman, L., Chandrashekhar, M., Park, J., McEuen, P. L., Parpia, J. M., Craighead, H. G., Spencer M. G. Free-Standing Epitaxial Graphene. *Nano Lett.* ***9*** (9), 3100-3105 (2009).

68. Barton, R. A., Ilic, B., Van der Zande A. M., Whitney, W. S., McEuen, P. L., Parpia, J. M., Craighead, H. G. High, Size-Dependent Quality Factor in an Array of Graphene Mechanical Resonators. *Nano Lett.* ***11*** (3), 1232-1236 (2011).

69. Lee, Y., Bae, S., Jang, H., Jang, S., Zhu, S. E., Sim, S. H., Song, Y. I., Hong, B. H., Ahn, J. H. Wafer-scale synthesis and transfer of graphene films. *Nano Lett.* **10**, 10(2) 490-3, (2010).

70. Huang, M., Pascal, T. A., Kim, H., Goddard, W. A., Greer, J. R. Electronic-mechanical coupling in graphene from in situ nanoindentation experiments and multiscale atomistic simulations. *Nano Lett.* Mar **9**,11(3), 1241-6 (2011).

71. Chen, X., Zheng, X., Kim, J., Li, X., & Lee, D. Investigation of graphene piezoresistors for use as strain gauge sensors*. J. Vac. Sci. Technol. B* **29**, 06FE01 (2011).

72. Hosseinzadegan, H., Todd, C., Lal, A., Pandey, M., Levendorf, M., Park, J. Graphene has ultra-high piezoresistive gauge factor. *MEMS, IEEE 25th International Conference,* 611–614 (2012).

73. Zhao, J, He, C, Yang, R, Shi, Z, Cheng, M, Yang, W, Xie, G, Wang, D, Shi, D, Zhang, G. Ultra-sensitive strain sensors based on piezoresistive nanographene films, *Appl. Phys. Lett.* 101, 063112 (2012).

74. Smith, A. D., Niklaus, F., Paussa, A., Vaziri, S., Fischer, A. C., Sterner, M., Forsberg, F., Delin, A., Esseni, D., Palestri, P., Östling, M., Lemme, M. C. Electromechanical piezoresistive sensing in suspended graphene membranes. *Nano Lett.* **13**, 3237−3242

(2013).

75. Zhao, J., Wang, G., Yang, R., Lu, X., Cheng, M., He, C., Xie, G., Meng, J., Shi, D., Zhang, G. Tunable piezoresistivity of nanographene films for strain sensing. *ACS Nano*. **24**, 9(2), 1622-9 (2015).

76. COMSOL multiphysics modeling guide. http://math.nju.edu.cn/help/mathhpc/doc/comsol/modeling.pdf

77. Zener, C., Internal Friction in Solids, *Phys. Rev.* **52**, 230-235 (1937)

78. Duwel, A., Candler, R., Kenny T., Varghese, M., *Journal of Microelectromechanical Systems,* vol. **15**, no. 6, pp. 1437–1445 (2006).

79. Gupta, S., Estimation of Thermo-Elastic Dissipation in MEMS, MSc. Thesis, Dept. Mechanical Engineering, *Indian Institute of Science*, *Bangalore,* (2004).

80. Roszhart, T.V. The Effect of Thermoelastic Internal Friction on the Q of Micromachined silicon resonators, *Tech. Dig. Solid-State Sens.* Actuator Workshop, Hilton Head, SC, pp. 13-16 (1990).

81. Lifshitz, R., & Roukes, K.L., Thermoelastic Damping in Micro- and Nanomechanical Systems, *Phy. Rev. B*. vol. **61**(8), 15(2000).

82. Ferrari, A. C. Raman spectroscopy of graphene and graphite: Disorder, electron–phonon coupling, doping and nonadiabatic effects. *Solid State Commun.* **143,** 47–57 (2007).

83. Malard, L. M., Pimenta, M. a., Dresselhaus, G. & Dresselhaus, M. S. Raman spectros-

copy in graphene. *Phys. Rep.* **473,** 51–87 (2009).

84. Kanda, Y. A Graphical Representation of the piezoresistance coefficients in Silicon. *IEEE Trans. Electron Devices* **29**, 64 (1982).

85. Kuczynski, G. C. Effect of Elastic Strain on the Electrical Resistance of Metals. *Phys. Rev.* **94**, 61 (1954).

86. webelement.com

87. Jen, S.U., Yu, C.C., Liu, C.H., Lee, G.Y. Piezoresistance and electrical resistivity of Pd, Au, and Cu films. *Thin Solid Films* **434**, 316–322 (2003).

88. Parker, R. L., & Krinsky, A. Electrical Resistance-Strain Characteristics of Thin Evaporated Metal Films. *J. Appl. Phys.* **34**, 2700 (1963).

89. Smith, C. S. Piezoresistance Effect in Germanium and Silicon. *Phys. Rev.* **94,** 42 (1954).

90. Kanda, Y. Piezoresistance effect of silicon. *Sen. & Act. A: Phy.* **28**(2), 83–91 (1991).

91. Li, C., Hesketh, P. J., & Maclay, G. J. Thin gold film strain gauges. *J. Vac. Sci. Technol. A* **12**, 813 (1994)

92. Bargatin, I., Myers, E. B., Arlett, J., Gudlewski, B., & Roukes M. L. Sensitive detection of nanomechanical motion using Piezoresistive signal downmixing. *Appl. Phys. Lett.* **86**, 133109 (2005).

93. Li, M., Tang, H. X., Roukes, M. L. Ultra-sensitive NEMS-based cantilevers for sensing, scanned probe and very high-frequency applications., *Nat. Nanotechnol.* **2**, 114–120 (2007).

94. Wu, C. C., Zhong, Z. Capacitive spring softening in single-walled carbon nanotube nanoelectromechanical resonators. *Nano Lett.* **13**, 11(4) 1448-51 (2011).

95. Xu, Y. *et al.* Radio frequency electrical transduction of graphene mechanical resonators. *Apl. Phy. Lett.* **97**, 243111 (2010).

96. Garcia-Sanchez, D., San Paulo, A., Esplandiu, M. J., Perez-Murano, F., Forró, L., Aguasca, A., Bachtold, A. Mechanical detection of carbon nanotube resonator vibrations. *Phys. Rev. Lett.* **99**, 085501 (2007).

97. Chen, C., Lee, S., Deshpande, V. V., Lee, G. H., Lekas, M., Shepard, K., Hone, J. Graphene mechanical oscillators with tunable frequency. *Nat. Nanotechnol.* **8,** 923–7 (2013).

98. Chen, C. "Graphene NanoElectroMechanical Resonators and Oscillators", PhD Thesis, University of Columbia, (2013).

99. Ishigami, M., Chen, J. H., Cullen, W. G., Fuhrer, M. S., Williams, E. D. Atomic structure of graphene on SiO_2. *Nano Lett.* ***7***(6) 1643-1648 (2007).

100. Moser, J., Barreiro, A. & Bachtold, A. Current-induced cleaning of graphene. *App. Phy. Lett.* **91**(16), 163513 (2007).

101. Lifshitz, R. & Cross, M. C. Reviews of Nonlinear Dynamics and Complexity Vol. 1 (*Wiley*, 2008).

102. Nayfeh, A. H. and Mook, T. R. Nonlinear Oscillations. *Wiley Inter science* (1979).

103. Krommer, H., Erbe, A., Tilke, A., Manus, S., and Blick, H. Nanomechanical resonators

operating as charge detectors in the nonlinear regime. *Euro phys. Lett*, **50** (1), 101-106 (2000).

104. Levenson, M. E. Harmonic and Subharmonic Response for the Duffing Equation αx+βx3 = Fcosωt (α>0). *J. Appl. Phys.* **20**, 1045-51 (1949).

105. Guckenheimer, J., Holmes, P. Nonlinear oscillations, dynamical systems, and bifurcations of vector fields. New York, London: Springer-Verlag, (1983).

106. Gil-Santos, E., Ramos, D., Martínez, J., Fernández-Regúlez, M., García, R., San Paulo, Calleja. M, Tamayo J. Nanomechanical mass sensing and stiffness spectrometry based on two-dimensional vibrations of resonant nanowires. *Nat Nanotechnol.* **5**(9): 641-5 (2010).

107. Nelis, M. R., Yu, L., Zhang, W., Zhao, Y., Yang, C., Raman, A., Mohammadi, S., Rhoads, J. F. 2011, Sources and implications of resonant mode splitting in silicon nanowire devices. *Nanotechnology* **22** (45): 455502 (2011).

108. Vallabhaneni, A. K., Rhoads, J. F., Murthy, J. Y., Ruan, X. Defect-Induced Mechanical Mode Splitting in Carbon Nanotube Resonators *J. Vib. Acoust.* **135**(2), 024504 (2013).

109. Barnard, A. W., Sazonova, V., van der Zande, A. M., McEuen, P. L., Fluctuation broadening in carbon nanotube resonators. *PNAS* **20**,109(47):19093-6 (2012).

110. Bae, S. *et al.* Roll-to-roll production of 30-inch graphene films for transparent electrodes. *Nat Nanotechnol.* **5** (8): 574-8 (2010).

111. Hosseini, P., Kumar, M., Bhaskaran, H. Two-dimensional materials as a functional platform for phase change tunable NEMS. *Access, IEEE* **3**,737-742 (2015).

Appendix

Ultrasensitive room temperature piezoresistive transduction in graphene-based nanoelectromechanical systems

Madhav Kumar and Harish Bhaskaran[§]

Department of Materials, University of Oxford, Parks Road, Oxford OX1 3PH, United Kingdom
[§] harish.bhaskaran@materials.ox.ac.uk

Abstract: The low mass and high quality factors that nanomechanical resonators exhibit lead to exceptional sensitivity in the frequency domain. This is especially appealing for the design of ultrasensitive force and mass sensors. The sensitivity of a nanomechanical mass and force sensor depends on its mass and quality factor; a low resonator mass and a higher quality factor reduce both the minimum resolvable mass and force. Graphene, a single atomic layer thick membrane is an ideal candidate for nanoelectromechanical resonators due to its extremely low mass and high stiffness. Here, we show that by employing the intrinsic piezoresistivity of graphene to transduce its motion in nanoelectromechanical systems (NEMS), we approach a force resolution 16.3 ± 0.8 aN/Hz$^{1/2}$ and a minimum detectable mass of 1.41 ± 0.02 zeptograms (10^{-21} g) at *ambient temperature*. Quality factors of the driven response of the order of 10^3 at pressures ~10^{-6} Torr on several devices are also observed. Moreover, we demonstrate this at ambient temperature on chemical-vapour-deposition-grown graphene to allow for scale-up, thus demonstrating its potential for

applications requiring exquisite force and mass resolution such as mass spectroscopy and magnetic resonance force microscopy.

Key words: Graphene NEMS, piezoresistive sensing, zeptogram mass sensitivity, attonewton force sensitivity, room temperature NEMS.

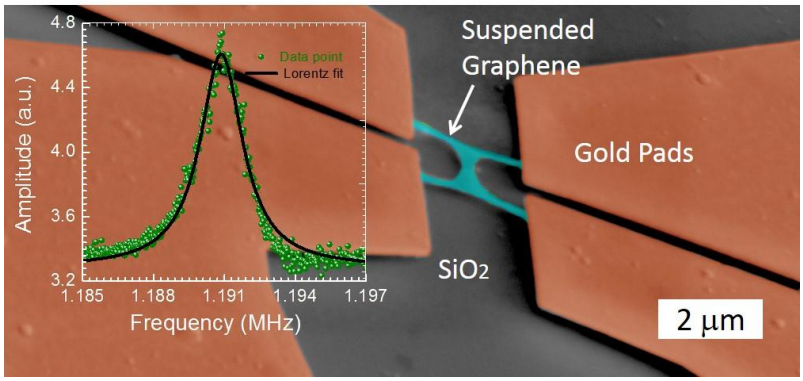

Nanoelectromechanical systems (NEMS)[1-2] can measure very small forces[3-5] and mass[6-7] as has been showcased in the last decade by the demonstration of measurements ranging from single spin detection[3] and mass spectroscopy[8-9] to the read-out of the quantum ground state of a mesoscopic resonator[10-11]. Mass spectroscopy with NEMS is particularly appealing because the vibrational frequency of NEMS is a sensitive function of its total mass; thus minute changes in mass due to added or removed adsorbate will change the resonance frequency of a nanomechanical resonator. Indeed, single molecule detection has recently been demonstrated using NEMS as a sensitive mass detector[6-7]. The minimum detectable mass is given by $\delta m = 2m_{eff}\,(\Delta f/Q \times \omega)^{1/2}10^{-(DR/20)}$ (*Refs* [1]), where m_{eff} is the

resonator mass, Q the quality factor and ω the resonance frequency, Δf the measurable bandwidth and DR the Dynamic Range[12-13]. Hence a resonator with low m_{eff} and high Q would be ideal for mass sensor. The minimum detectable force of a nanomechanical resonator is given by the force spectral density as $F_{min} = (S_{th})^{1/2} = (4k_bTk/\omega Q)^{1/2}$ (*Refs* [4]), where ω is the resonance frequency, k is the spring constant (which increases with increasing mass, as $k = m_{eff}\,\omega^2$), T the temperature and k_b is the Boltzmann constant. Thus, to maximize mass as well as force sensitivity, resonators with low mass, low resonance frequency, and high quality factors are required. Whilst resonators based on Silicon Nitride can exceed quality factors of 10^6 [(14)], its mass is not as low as that of monolayer graphene[15]. The high Young's modulus[58] and surface area contribute to graphene-based resonators being ideal for mass and force sensors. Extensive studies have been carried out on graphene NEMS by employing both optical[58-20] and electrostatic[21-26] actuation techniques. The maximum room temperature quality factors (Q) achieved[58-25] by these techniques are of the order of 10^2 for a double sided clamped graphene resonator and 10^3 for graphene based drum resonators.[20,25] The use of metal piezoresistivity for sensing in NEMS was described by Li *et al.*[27] and was shown to be a very effective readout method over a wide frequency range. In this work, we utilize the intrinsic piezoresistivity of graphene[28-30] as a self-sensing component. By employing this piezoresitivity in a monolayer graphene resonator, we have estimated sensitivity down to attonewton forces and to zeptogram mass and have recorded room temperature Q of the order of 10^3 (1-2). Importantly, by fabricating such resonators

on chemical-vapour-deposition (CVD) grown graphene we demonstrate proof-principle scalable manufacturing of graphene resonators. Our electrical read-out is effective, yet simple; a compact vacuum chamber is sufficient to carry out these measurements in ambient temperatures.

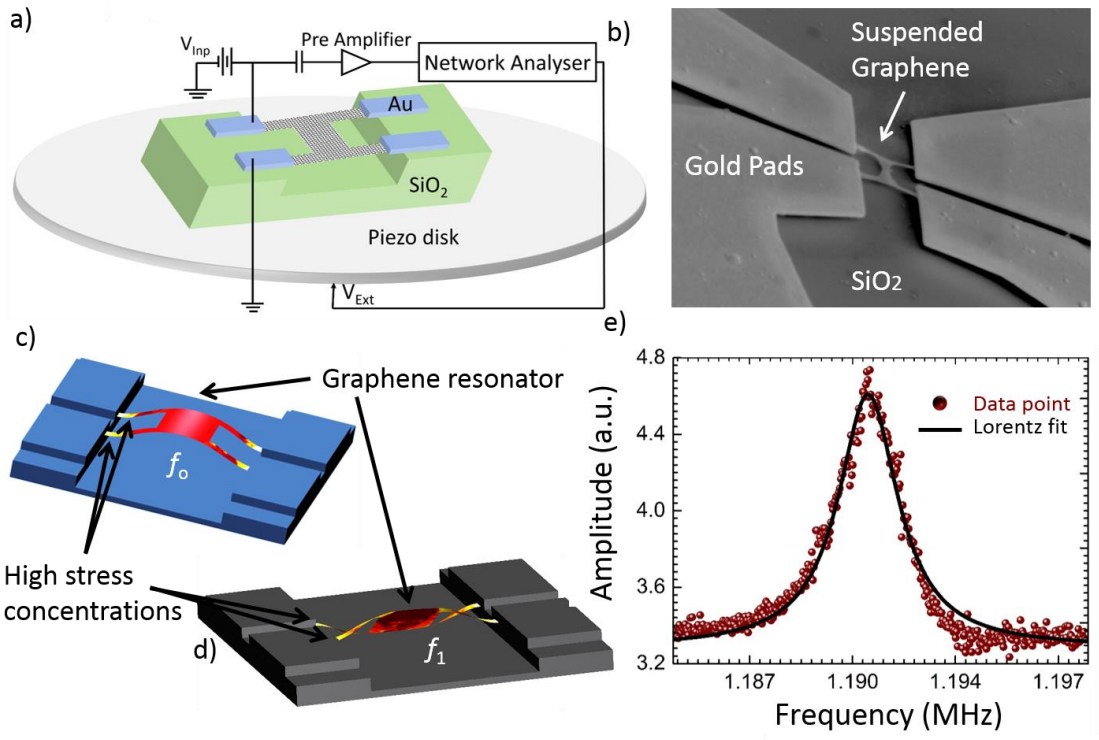

Figure 1. Piezoresistive transduction of graphene-NEMS. (a) Schematic of the device with circuit diagram of the measurement setup. (b) SEM image of a fabricated suspended H shape graphene resonator clamped at the base by four gold electrodes and silicon dioxide. (c-d) Finite element model (FEM) of the device, indicating the leg area has the highest strain energy density at the mechanical resonance frequency (yellow), (c) first mode (f_o) and (d) second mode (f_1). (e) Amplitude with frequency at V_{Inp}= 75mV and V_{Ext} = 2V of a mechanical resonator with f_0= 1.191MHz (The lines are Lorentzian fit to the data).

To increase the sensitivity due to the instrinsic piezoresistive effect, we make use of higher stress concentrations near the base of a mechanical resonator, where the resistance

change is most pronounced. We have thus employed a four-sided clamped H shaped graphene beam, which allows us to measure across the regions of maximum stress near the supports of the mechanical beam to maximize the piezoresistivity. Our measurement is done across any one set of two such constrictions (legs) near the supports. Figure 1a shows a schematic of our device and in Figure 1b, a scanning electron micrograph of a fabricated H shaped graphene resonator clamped at the base by four gold electrodes and silicon dioxide is shown. We measure the resistivity across any two adjacent pairs of legs, and this resistance varies as a result of the piezoresistivity. Our mechanical resonators have a total length of 1.8 μm, and total width of 1.2 μm; the dimension of each leg ~ 120-150 nm wide and 0.5-0.7 μm long.

As this resonator vibrates, most of the mechanical stress at maximum deflection of the first and second vibrational mode is concentrated near the legs for effective piezoresistive transduction. The device is designed such that the resistance across the legs in the conducting path accounts for 65-80% of the total resistance of the conducting path of the suspended portion of the resonator. Finite Element Modeling (Figure 1Figure 1c-d) confirms that this base region has the highest stress (see Supporting Information 1 for details). We then fabricate these devices using Chemical Vapour Deposition (CVD) grown monolayer graphene (see Supporting Information 2 for details of fabrication). We verify that the devices are suspended using SEM imaging (*See Supporting Information 2*). We employ Raman spectroscopy[31-32] to confirm that the graphene is monolayer prior to

fabrication (*Data in Supporting Information 3*). Our device resistance drops from 6-8 kΩ to 0.8 kΩ during current annealing of the device, which is performed before electrical measurements in line with other measurements on graphene[23,26,33] (*more information in Supporting Information 4*). All measurements are performed at room temperature and at pressures of ~ 4 x 10^{-6} Torr.

Initial verification of piezoresitive sensing is done by actively driving the nanomechanical resonator using a voltage controlled piezomechanical disc (V_{Ext}). A DC bias voltage (V_{Inp}) is applied across the two legs of the same side of the H shaped graphene beam to convert the resistance variation to a voltage signal. The schematic of our measurement is shown in Figure 1a and exemplifies the simplicity of the simultaneously measures the output electrical signal from the device. Figure 1e shows the fundamental resonance frequency (f_o) of this device (arbitrarily described as Device 1 henceforth) at 1.191MHz at V_{Inp} = 75mV and V_{Ext} = 2V. For most of the resonators of same size, on the same chip (with same fabrication process) we have measured f_o between 1-3 MHz. The resonance frequency as estimated by the finite element simulation is around 1 MHz, approximately of the same order of magnitude as measured for most of the devices. In Figure 1 we show the driven response of two different resonators (device 1 and 2); in both cases, the resonance is driven piezomechanically. The lock-in amplifier is used, whose output drives the piezomechanical disc and sweep the drive frequency while monitoring the output at the amplifier. As the drive amplitude is increased (V_{Ext}), indicating that these resonators have a slight slack[34]. Our

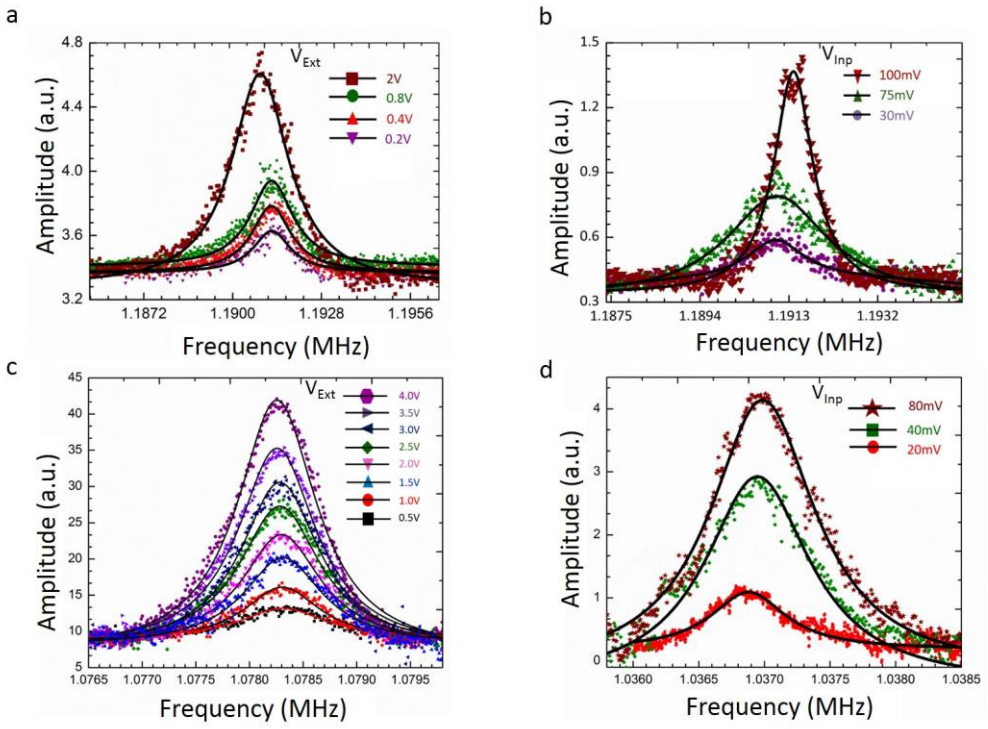

Figure 2. Externally driven frequency response. (a) Variation of amplitude at f_o with different external drive amplitudes (V_{Ext}) at constant bias voltage V_{Inp} = 75mV to the device (Device 1). (b) Variation of amplitude at f_o at different V_{Inp} and constant V_{Ext} = 2V (Device 1). At V_{Ext} = 2V, for V_{Inp}= 100mV Device 1 shows quality factor of the order of 10^3. (c) Variation in amplitude at different V_{Ext}, and constant V_{Inp}= 120mV (Device 2). (d) Variation of amplitude at f_o at different V_{Inp} and constant V_{Ext} = 6V (Device 2). Device 2 also shows quality factor of the order of 10^3.

FEM simulations indicate that the expected frequency range is within the same order of magnitude as measured, in contrast to previously reported on mechanically exfoliated graphene,[58,21,23] where the frequency was significantly higher than expected due to intrinsic tension. This is not unexpected – the graphene we use is grown using CVD and transferred to a silicon dioxide substrate in liquid, which would significantly change intrinsic stress effects as compared to mechanically exfoliated graphene.

Figure 1a and c shows broadening of the resonance peaks and a slight deviation towards the lower frequency with increasing drive amplitude (V_{Ext}) which indicates negative nonlinearity in the spring constant[35]. There are differences between devices, for example, device 1 (Figure 1a) is more non-linear when compared to device 2 (Figure 1c) where there is less change in f_0 with $V_{Ext.}$ Non-linearity in NEMS and its onset is of concern particularly for mass sensing, where the Dynamic Range of a device sets the minimum resolvable mass, and we discuss this later. Our measurements indicate that our devices may have some slack[34] probably due to use of CVD graphene. Depending on the

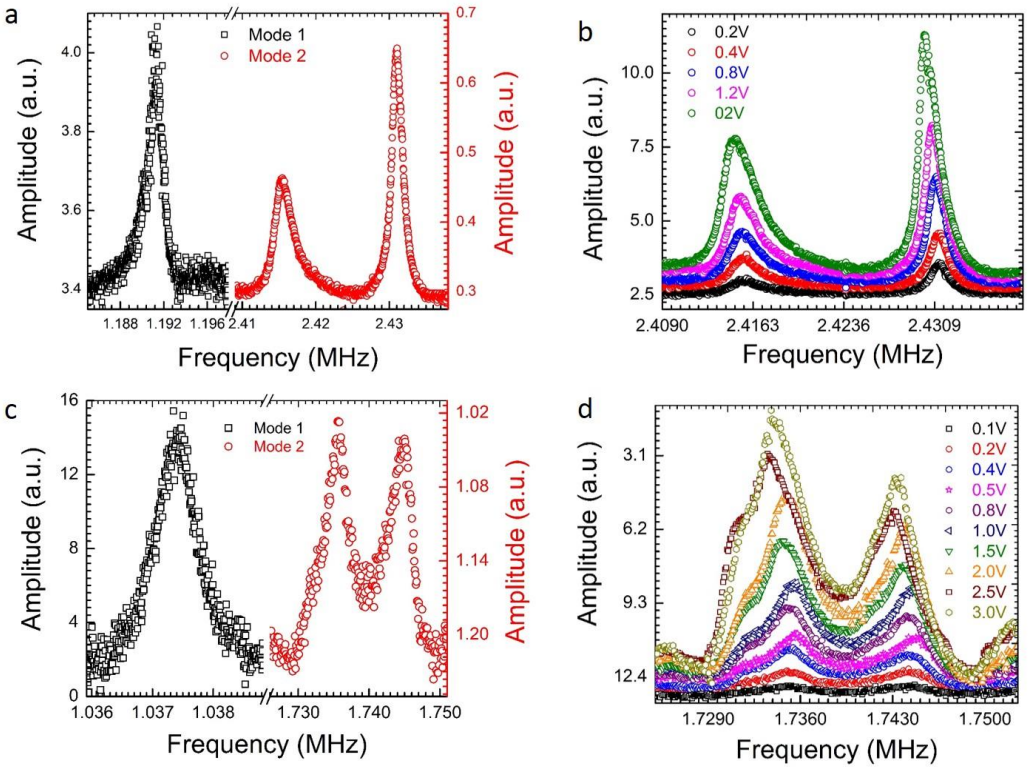

Figure 3 Externally driven frequency response of the second mode (f_1) . (a) Fundamental mode resonance f_o (black hollow squares) and the second mode f_1 (red hollow circles) of device 1. (b), Variation of amplitude at f_1 with different V_{Ext} at V_{Inp} =40mV for device1. (c), f_o and f_1 for device 2. (d), Variation in amplitude at f_1 with different V_{Ext}, and constant V_{Inp}= 100mV (device 2).

amount of slack in each device, the effect may not discernible. Graphene displays a negative coefficient of thermal expansion.[23,26] Essentially, this would entail that as we increase V_{Inp}, more power is dropped across the graphene resonator, which would heat the resonator; hence, the resonance frequency would be expected to go up for a resonator under tensile stress. As shown in Figure 1b and 2d, we indeed observe this behaviour in both the device 1 and 2.

We then transduce the second mode of the resonator piezoresistively. The second mode as modelled by FEM is shown in Figure 1d (more data in Supporting Information 1). In this mode, at resonance, the two support legs move in opposite directions (Figue 1d). However, because of slight asymmetry in the shape and mass between the two legs, the degenerated resonance peak may split into two peaks. We are able to observe the second mode, confirming that piezoresistive transduction is an effective and sensitive method to observe motion on graphene NEMS resonators. Frequency response for both these devices in the second mode is shown in Figure 2. Figure 2a shows the fundamental resonance frequency (f_o) at 1.19MHz and second Eigen frequency (f_1) at around 2.2 MHz for device 1. Figure 2c shows the fundamental resonance frequency (f_o) at 1.10375MHz and second mode (f_1) at 1.74 MHz for the device 2. Figure 2b shows driven response at f_1 with different V_{Ext} at constant V_{Inp} = 40mV for device 1; the decrease in f_1 with increase in V_{Ext} is similar to that of f_o shown in Figure 1a.

For device 2, Figure 2d shows the response of f_1 with different V_{Ext} at constant V_{Inp} = 100mV. We observe that there is less variation in the frequency of the two legs, i.e. the degenerated peaks are closer to each other. This is most probably because the two legs for device 2 are geometrically more symmetrical. The resonance response upon increasing drive amplitude for this device (Figure 2d) is similar to the f_o shown in Figure 1c. The measured value of f_1 is 2.2 MHz for device 1 and 1.7 MHz for device 2, the same order as calculated using FEM model (Data in Supporting Information 1, figure S1b). For device 1 the splitting is prominent as we can see two distinct peaks very close to each other (Figure 2a-b), while for device 2 the splitting is relatively small compared to device 1 (as shown in Figure 2c-d) but still clearly discernible. This ability to transduce motion in the second mode is further proof of peizoresistive transduction and also underlines the sensitivity of this detection scheme. We note that such dual modes are observable in other mechanical systems made by microfabrication methods, for example, triangular cantilevers in atomic force microscopy (our data on such commercially available cantilevers are included in *Supporting Information 5*).

We then proceeded to resolve the thermomechanical motion[58,27] of the resonator. Thermomechanical noise of the resonator is the Johnson's noise equivalent for the mechanical resonator, thus being present at all temperatures above 0 K. We measure the thermomechanical noise spectrum by averaging the spectrum 64 times to obtain high-resolution data. Figure 3a shows the amplitude due to thermomechanical motion at V_{Inp} =

120 mV (the red solid line in the figure is the Lorentzian fit to the data). As external drive amplitude (V_{Ext}) is increased, we can then drive the resonator, similar to that seen in the other devices, confirming that this is indeed a highly sensitive transduction method capable of sensing the Brownian motion of the resonator. Figure 3b shows amplitude variation of f_o at constant V_{Inp} with different V_{Ext} including the thermomechanical noise data (V_{Ext} = 0V, black data points). We see a decrease in f_o (softening non-linearity) as we increase the external drive amplitude. It is worth noting that we observe this softening effect in all our devices.

We can then calculate the minimum resolvable mass $\delta m = 2m_{eff}\ (\Delta f/Q \times \omega)^{1/2} \bullet 10^{-(DR/20)}$, which is approximated to $(m_{eff}/Q) \bullet 10^{-DR/20}$ *(Refs*[1-2,27]*)*. The dynamic range (DR)[12-13] is a key aspect of mass sensitivity, and we estimate this to be at least 60dB for both devices 1 and

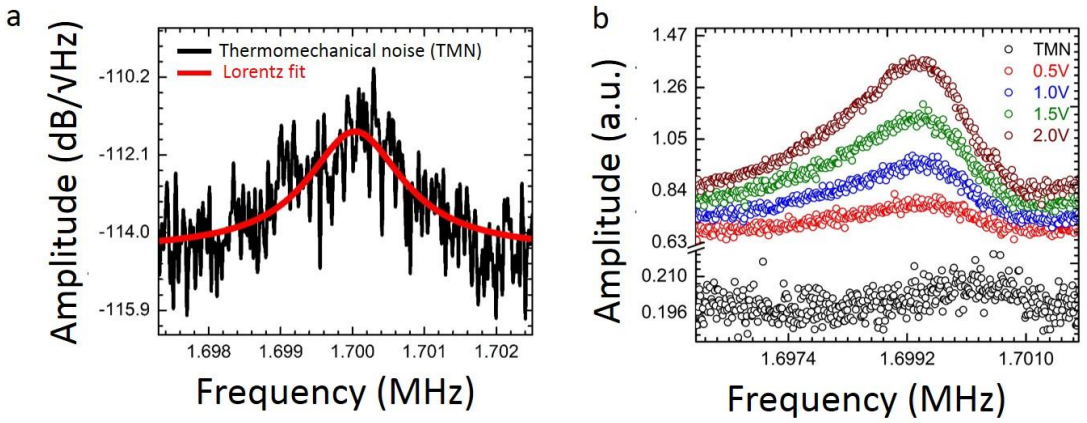

Figure 4 Thermomechanical motion detection. (a), Amplitude of thermomechanical motion at the resonance frequency (1.7MHz) of a resonator V_{Inp} = 120mV; Quality factor (Q) = 1043, and Bandwidth = 7Hz. (b), Variation of amplitude at constant V_{Inp}= 140mV for different V_{Ext} at f_o. f_o decreases (softening of resonator) as we drive the resonator.

3 (as shown in Supporting Information 7). For Device 1, with Q = 1180 (± 20) we calculate the mass sensitivity to be 1.41 (± 0.02) zeptograms (10^{-21} g) at room temperature (see Supporting Information 10 for details). The spring constant for these resonators are also extremely low (of the order of 10^{-4} N/m). The force sensitivity is calculated using force spectral density to be 16.3 ± 0.8 aN/$\sqrt{Hz}$ at 300 K for device 3. Thus, such a sensor is in principle capable of resolving forces of the order of attonewton at room temperatures.

We finally comment on the observed non-linearity in these resonators. Graphene-NEMS with small dimensions and mass often show nonlinear response[21,36-37]. Equation 1[21,36] describes the motion of nonlinear resonators with duffing nonlinearity (αx^3) as well as higher order nonlinear damping ($\eta.x^2.(dx/dt)$), where M is the effective mass of the resonator.

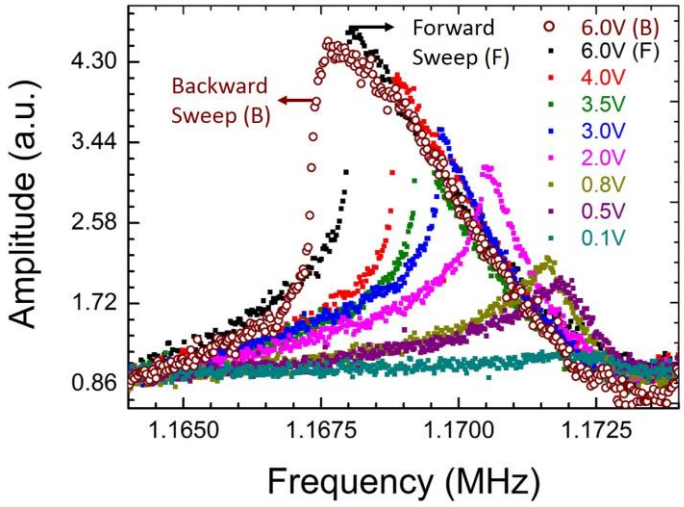

Figure 5 Nonlinearity in Graphene resonator. Variation of amplitude at f_o at different V_{Ext} and constant V_{Inp} = 40mV. Negative nonlinear spring constants and duffing nonlinear behaviour due to large vibrational amplitude is observed.

These nonlinearities are more prominent when either a large excitation force is applied or the device mass is very small. As we drive the resonator with increasing amplitude, we observe duffing non-linearity (α) as shown in Figure 4. We also observe hysteresis in the fundamental resonance mode while sweeping the frequency forward

$$M\left(\frac{d^2x}{dt^2}\right) + \gamma\left(\frac{dx}{dt}\right) + kx + \alpha x^3 + \eta x^2\left(\frac{dx}{dt}\right) = Fcos(\omega t) \qquad \ldots\ldots 1$$

(black data points) and backward (red data points, Figure 4). All of this is consistent with the inherent non-linearity in nanoelectromechanical systems, further confirming the validity and sensitivity of our piezoresistive sensing scheme. We note that much work on the use of non-linear systems to enhance sensitivity can be employed[38-40] and this could be the subject of further investigation using our measurement scheme.

In conclusion, we demonstrate that the intrinsic piezoresistivity of graphene is an effective technique to transduce the motion of monolayer graphene nanomechanical resonators. We find that such graphene resonators show high *Q*-factors of $>10^3$ for an externally driven response, the highest reported for beam resonators at room temperature[37]. Using this technique, we demonstrate sensing of the second mode of the resonator. We have shown thermomechanical motion in ambient temperatures and pressures of ~ 4×10^{-6} T. The minimum detectable mass and force resolution of such resonators is calculated to be an astounding 0.95 – 1.54 zeptograms (10^{-21} g) and 11.7 – 21.6 aN/Hz$^{1/2}$ at *room temperature*. The sensitivity of the detection technique is further demonstrated by detecting the second order resonance mode of the resonator, underlining

the resolution of this technique. Furthermore, we demonstrate these on a scalable platform using a simple tabletop apparatus, which could hence be commercialized on hermetically sealed packages. Such high sensitivity at room temperature using CVD grown graphene could herald tabletop applications of hitherto low-temperature techniques such as MRFM and single molecule spectroscopy. We also observe nonlinearity in these devices as is common in graphene NEMS. Understanding the onset of nonlinearity in such devices is particularly important for two-dimensional layers such as graphene, and this platform will allow one to address the basic understanding of such Physics in terms of higher order modes. Further investigation of techniques to use these for mass spectroscopy in vacuum could result in inexpensive and highly sensitive NEMS devices for applications in mass spectrometry.

Methods

Device Fabrication.

Samples were fabricated by patterning commercially available CVD grown graphene on 285nm Silicon dioxide substrate (Graphene Supermarket) using electron beam lithography and argon plasma reactive ion etching (RIE). Metal electrodes were patterned and fabricated by evaporating 5nm Chromium (Cr) as a adhesion layer and 90nm Gold (Au) as metal electrodes. Graphene was suspended by under-etching SiO_2 using buffered hydrofluoric acid[21,23,26,33]. To prevent the suspended graphene membrane from collapsing

during the drying process due to surface tension effects, we employ critical point drying[23,26,33]. *(More information in Supporting Information 2.)*

Electrical Measurement.

Our electrical readout method utilizes piezoresistivity[27] of graphene as a self-sensing component for NEMS. A DC bias (V_{Inp}) is applied to two adjacent legs of the resonator to convert the resistance variation to a voltage signal, which is amplified with a preamplifier (MITEQ AU1442), and the frequency response of the beam is measured with a Lock-in ampliifier (Zurich Instruments HF2 with UHS option). All measurements are carried out at high vacuum (> 10^{-6} T) to increase quality factor. *(More information in Supporting Information 4.)*

ASSOCIATED CONTENT

Supporting Information

Modal analysis, device fabrication, characterization, electrical measurement, resonance frequency of commercial cantilever, time domain signal, calculation of dynamic range, thermoselastic damping, calculations of mass and force sensitivity, Figure S1-9 and Table 1.

AUTHOR INFORMATION

Corresponding Author

[§]E-mail: harish.bhaskaran@materials.ox.ac.uk

Author Contributions

MK performed the fabrication, experimentation, data acquisition and analysis. HB conceived of the concept, led the study and the experimentation. Both authors co-wrote the manuscript.

Acknowledgments

We acknowledge useful discussions with Bhaskar Choubey on non-linearity and damping. MK and HB acknowledge access to sample fabrication facilities at the University of Exeter's Centre for Graphene Science and CD Wright for supporting this. We are grateful for scientific and technical discussions with D. Anderson, BF. Porter, G. Rodriguez-Hernandez. P. Hosseini and A. Neg. HB acknowledges support from the OUP John Fell Fund and EPSRC via grants EP/J00541X/1/2 and EP/J018694/1.

References

1. Ekinci, K. L.; Yang, Y. T.; Roukes M. L. *J. Appl. Phys.* **2004,** 95**,** 2682-9.

2. Ekinci, K. L.; Roukes, M. L. *Rev. Sci. Instrum.* **2005,** 76, 061101-12.

3. Rugar, D.; Budakian, R.; Mamin, H. J.; Chui, B. W. *Nature* **2004,** 430, 329-332.

4. Kenny, T. *IEEE Sens. J.* **2001,** 1**,** 148.

5. Moser, J.; Güttinger, J.; Eichler, A.; Esplandiu, M. J.; Liu, D. E.; Dykman, M. I.; Bachtold, A. *Nature Nanotech* **2013***,* 8, 493-6.

6. Chaste, J.; Eichler, A.; Moser, J.; Ceballos, G.; Rurali, R.; Bachtold, A. *Nature Nanotech.* **2012,** 7**,** 301–4.

7. Lassagne, B.; Garcia-Sanchez, D.; Aguasca, A.; Bachtold, A. *Nano Lett.* **2008,** 8 (11), 3735-3738.

8. Naik, A. K.; Hanay, M. S.; Hiebert, W. K.; Feng, X. L.; Roukes, M. L. *Nature Nanotech.* **2009,** 4, 445–450.

9. Hanay, M. S.; Kelber, S.; Naik, A. K.; Chi, D.; Hentz, S.; Bullard, E. C.; Colinet, E.; Duraffourg, L.; Roukes, M. L. *Nature Nanotech.* **2012,** 7**,** 602–8.

10. O'Connell, A. D.; Hofheinz, M.; Ansmann, M.; Bialczak, R. C.; Lenander, M.; Lucero, E.; Neeley, M.; Sank, D.; Wang, H.; Weides, M.; Wenner, J.; Martinis, J. M.; Cleland, A. N. *Nature* **2010**, 464, 697–703.

11. Rocheleau, T.; Ndukum, T.; Macklin, C.; Hertzberg, J. B.; Clerk A. A.; Schwab. K. C. *Nature* **2010,** 463, 72–5.

12. Postma, H. W. C.; Kozinsky, I.; Husain, A.; Roukes, M. L. *Appl. Phys. Lett.* **2005,** 86, 223105-3.

13. Kozinsky, I.; Postma, H. W. C.; Bargatin, I.; Roukes, M. L. *Appl. Phys. Lett.* **2006,** 88**,** 253101-3.

14. Hosseini, E. S.; Yegnanarayanan, S.; Atabaki, A. H.; Soltani, M.; Adibi, A. *Opt. Express* **2009,** 17 (17)**,** 14543–51.

15. Geim, A. K.; Novoselov, K. S. The rise of graphene. *Nature Mater.* **2007,** 6, 183–91.

16. Bunch, J. S.; Van der Zande, A. M.; Verbridge, S. S.; Frank, I. W.; Tanenbaum, D. M.; Parpia J. M.; Craighead H. G.; McEuen P. L. *Science* **2007,** 315 (5811), 490-493.

17. Bunch, J. S.; Verbridge, S. S.; Alden, J. S.; Van der Zande, A. M.; Parpia, J. M.; Craighead, H. G.; McEuen, P. L. *Nano Lett.* **2008,** 8 (8), 2458–62.

18. Robinson, J. T; Zalalutdinov, M.; Baldwin, J. W.; Snow, E. S.; Wei, Z.; Sheehan, P.; Houston, B. H. *Nano Lett.* **2008,** 8 (10), 3441–5.

19. Shivaraman, S.; Barton, R. A.; Yu, X.; Alden, J.; Herman, L.; Chandrashekhar, M.; Park, J.; McEuen, P. L.; Parpia, J. M.; Craighead, H. G.; Spencer M. G. *Nano Lett.* **2009,** 9 (9), 3100–5.

20. Barton, R. A.; Ilic, B.; Van der Zande A. M.; Whitney, W. S.; McEuen, P. L.; Parpia, J. M.; Craighead, H. G. *Nano Lett.* **2011,** 11 (3)**,** 1232–6.

21. Eichler, A.; Moser, J.; Chaste, J.; Zdrojek, M.; Wilson-Rae I.; Bachtold A. *Nature Nanotech.* **2011,** 6, 339–42.

22. Garcia-Sanchez, D.; Van der Zande, A. M.; Paulo, A. S.; Lassagne, B.; McEuen, P. L.; Bachtold, A. *Nano Lett.* **2008,** 8 (5)**,** 1399–403.

23. Chen, C.; Rosenblatt, S.; Bolotin, K. I.; Kalb, W.; Kim, P.; Kymissis, I.; Stormer, H. L.; Heinz, T. F.; Hone, J. *Nature Nanotech.* **2009,** 4, 861–7.

24. Van der Zande A. M.; Barton, R. A.; Alden, J. S.; Ruiz-Vargas, C. S.;, Whitney, W. S.; Pham, P. H. Q; Park. J.; Parpia. J. M.; Craighead, H. G.; McEuen, P. L. *Nano Lett*. **2010,** 10 (12), 4869–4873.

25. Chen, C.; Lee, S.; Deshpande, V. V.; Lee, G. H.; Lekas, M.; Shepard, K.; Hone, J. *Nature Nanotech.* **2013,** 8, 923–7.

26. Singh, V.; Sengupta, S.; Solanki, H. S.; Dhall. R.; Allain. A.; Dhara.; S.; Pant, P.; Deshmukh M. M. *Nanotechnology* **2010,** 21, 165204.

27. Li, M.; Tang, H. X.; Roukes, M. L. *Nature Nanotech.* **2007,** 2, 114–20.

28. Hosseinzadegan, H.; Todd, C.; Lal, A.; Pandey, M.; Levendorf, M.; Park, J. *MEMS, IEEE 25th International Conference,* **2012,** 611–614.

29. Zhao, J; He, C; Yang, R; Shi, Z; Cheng, M; Yang, W; Xie, G; Wang, D; Shi, D; Zhang, G. *Appl. Phys. Lett.* **2012,** 101**,** 063112-5.

30. Smith, A. D.; Niklaus, F.; Paussa, A.; Vaziri, S.; Fischer, A. C.; Sterner, M.; Forsberg, F.; Delin, A.; Esseni, D.; Palestri, P.; Östling, M.; Lemme, M. C. *Nano Lett.* **2013,** 13 (7), 3237−42.

31. Ferrari, A. C. *Solid State Commun.* **2007,** 143, 47–57.

32. Malard, L. M.; Pimenta, M. A.; Dresselhaus, G.; Dresselhaus, M. S.; *Phys. Rep.* **2009,** 473, 51–87.

33. Bolotin, K. I.; Sikes, K.J.; Jiang, Z.; Klima, M.; Fudenberg, G.; Hone, J.; Kim, P.; Stormer, H.L. *Solid State Commun.* **2008,** 146**,** 351–355.

34. Garcia-Sanchez, D.; San Paulo, A.; Esplandiu, M. J.; Perez-Murano, F.; Forró, L.; Aguasca, A.; Bachtold, A. *Phys. Rev. Lett.* **2007,** 99, 085501-4.

35. Song, X.; Oksanen, M.; Sillanpää, M. A.; Craighead, H. G.; Parpia, J. M.; Hakonen, P. J. *Nano Lett.* **2011,** 12, 198–202.

36. Lifshitz, R.; Cross, M. C. *Reviews of Nonlinear Dynamics and Complexity*; Wiley: New York, 2008; pp 1-48.

37. Chen, C.; Hone, J. *Proc. IEEE* **2013,** 101, 1766–79.

38. Buks, E.; Yurke, B. *Physical review E* **2006***,* 74, 046619 .

39. Datskos, P. G.; Lavrik, N. V. *US 8505382 B2* **2013**.

40. Kumar, V., Boley, J. W.; Yang, Y.; Ekowaluyo, H.; Miller, J. K.; Chiu, G. T. C.; Rhoads, J. F. *Appl. Phys. Lett.* **2011,** 98, 153510.